

**AD-A257 069****TATION PAGE**Form Approved  
OMB No. 0704-0188**1**

d to average 1 hour per response, including the time for reviewing instructions, searching existing data sources, reviewing the collection of information. Send comments regarding this burden estimate or any other aspect of this burden to Washington Headquarters Services, Directorate for Information Operations and Reports, 1215 Jefferson Avenue, Washington, DC 20540, and to the Office of Management and Budget, Paperwork Reduction Project (0704-0188), Washington, DC 20503.

<b>1. DATE</b> 10-5-92		<b>3. REPORT TYPE AND DATES COVERED</b> Final 5/1/87 - 7/31/92	
<b>4. TITLE AND SUBTITLE</b> Radar Scene Generation for Tactical Decision Aids		<b>5. FUNDING NUMBERS</b> DACA39-87-K-0022  7041/0024	
<b>6. AUTHOR(S)</b> Prof. J.A. Kong		<b>8. PERFORMING ORGANIZATION REPORT NUMBER</b>	
<b>7. PERFORMING ORGANIZATION NAME(S) AND ADDRESS(ES)</b> Research Laboratory of Electronics Massachusetts Institute of Technology 77 Massachusetts Avenue Cambridge, MA 02139		<b>10. SPONSORING / MONITORING AGENCY REPORT NUMBER</b>	
<b>9. SPONSORING / MONITORING AGENCY NAME(S) AND ADDRESS(ES)</b> Army Corps of Engineers Waterways Experiment Station P.O. Box 631 Vicksburg, MS 39180		<b>11. SUPPLEMENTARY NOTES</b> The view, opinions and/or findings contained in this report are those of the author(s) and should not be construed as an official Department of the Army position, policy, or decision, unless so designated by other documentation.	
<b>12a. DISTRIBUTION / AVAILABILITY STATEMENT</b>  Approved for public release; distribution unlimited.		<b>12b. DISTRIBUTION CODE</b>	
<b>13. ABSTRACT (Maximum 200 words)</b>  Work by Prof. Kong and his collaborators is summarized here  <div style="text-align: center;"><b>DTIC</b> <b>ELECTE</b> <b>OCT 13 1992</b> <b>S B D</b></div> <div style="text-align: right;">304050</div> <div style="text-align: right;"><b>92-26912</b> </div>			
<b>14. SUBJECT TERMS</b>		<b>15. NUMBER OF PAGES</b>	
		<b>16. PRICE CODE</b>	
<b>17. SECURITY CLASSIFICATION OF REPORT</b> UNCLASSIFIED	<b>18. SECURITY CLASSIFICATION OF THIS PAGE</b> UNCLASSIFIED	<b>19. SECURITY CLASSIFICATION OF ABSTRACT</b> UNCLASSIFIED	<b>20. LIMITATION OF ABSTRACT</b> UL

## **FINAL REPORT**

**Title: RADAR SCENE GENERATION FOR TACTICAL DECISION AIDS**

**Sponsor by: Army Corps of Engineers  
Waterways Experimental Station**

**Contract number: DACA39-87-K-0022**

**Research Organization: Center for Electromagnetic Theory and Applications  
Research Laboratory of Electronics  
Massachusetts Institute of Technology**

**OSP number: 99139**

**Principal Investigator: J. A. Kong**

**Author of Report: Y. Eric Yang**

**Period covered: May 1, 1987 — July 31, 1992**

## RADAR SCENE GENERATION FOR TACTICAL DECISION AIDS

This work was supported by the U.S. Army Engineer Waterways Experiment Station, Vicksburg, Miss. as part of the Air Land Battle Field Environment (ALBE) thrust program with point of contact Dr. Richard Weiss. We have published 67 refereed journal and conference papers for the research on the Radar Scene Generation For Tactical Decision Aids.

EMSARS (Electromagnetic Model of Scattering Applied to Remote Sensing) is an electromagnetic background scattering model developed at the Massachusetts Institute of Technology. The physical characterization of the terrain background is in terms of layered continuous random medium and discrete scatterer models. Various theories and mathematical techniques such as the analytical Wave Theory with the Born Approximation and the Radiative Transfer Theory are used to solve the integral equations characterizing the electromagnetic scattering effects. We recently presented applications of the EMSARS model to millimeter wave scattering by vegetation. Tree is modeled as discrete scatterers with multiple size for the trunk, the branches and leaves, respectively. The leaves of coniferous trees, the branches, and the trunks are modeled as circular cylinders. For deciduous trees, the leaves are modeled as thin circular disks. The physical optics approximation is used to calculate the millimeter wave returns from circular disks while finite cylinder approximation is used for circular cylinders. Then, the branching structure and their orientation distributions are applied to obtain the radar returns from vegetation. The trunk is model as a circular cylinde with random surface roughness where geometrical optics approximation is used to calculate the radar return from the surface of trunk. Except for

the case in which the ground is illuminated, we only consider single scattering returns. Transmission loss factors, due to absorption and scattering, are included when computing the contribution from interior branches and leaves. Theoretical predictions are compared with the measurement data collected in Bend, Oregon by NVEOD using a 94GHz radar.

Polarimetric radar calibration algorithms using a combination of point targets and reciprocal distributed targets are developed. From distributed target, a matrix equation is derived which can be converted into an equivalent point target response. The equivalent point target corresponds physically to a 90-degree polarization rotator which is non-reciprocal and rotation-invariant. Due to this equivalent-point-target interpretation, the cases of polarimetric calibration using two point targets and one distributed target then reduce to those using three point targets, which have been solved in previous research. Regarding the calibration using one point target and one reciprocal distributed target, two cases are analyzed with the point target being a sphere (trihedral reflector) or a polarimetric active radar calibrator (PARC). For both cases, the general solutions of system distortion matrices are written as a product of a particular solution and a matrix with one free parameter, and then an additional assumption about the distributed target is made to determine the free parameter. For the trihedral-reflector case, when the particular solution is applied for calibration, the measured polarimetric data can be calibrated to the level that only rotation errors remain, and once azimuthal symmetry is assumed for the distributed target, an iterative scheme is devised to solve the rotation parameter. For the PARC case, the residual error is like the channel imbalance after the data are calibrated by the particular solution, and the free parameter can be determined by knowing one ratio of two covariance matrix elements of the distributed target. Numerical results were simulated to demonstrate the validity of the algorithms developed.

DTIC QUALITY INSPECTED 1

By _____	
Distribution/	
Availability Codes	
Dist	Avail and/or Special
A-1	

To develop an algorithm for retrieving forest biomass using SAR data, a study is performed, which includes: 1) observations on the relation between backscatter and forest biomass, 2) interpretation of the observations by modelling and 3) simulation of radar response for a wide range of forest and ground conditions. We have obtained preliminary results of P-band backscatter simulations as functions of radar incidence angle, ground slope, undergrowth vegetation state, vegetation moisture content, and crown structure.

A branching model is proposed for the remote sensing of vegetation. The frequency and angular responses of a two-scale cylinder cluster are calculated to demonstrate the significance of vegetation architecture. The results indicate that it is necessary for theoretical models to take into account the architecture of vegetation which plays an important role in determining the observed coherent effects. A two-scale branching model is implemented for soybean with its internal structure and the resulting clustering effects considered. Furthermore, at the scale of soybean fields, the relative location of soybean plants is described by a pair of distribution function. The polarimetric backscattering coefficients are obtained in terms of the scattering properties of soybean plants and the pair distribution function. Theoretical backscattering coefficients evaluated using the hole-correction pair distribution are in good agreement with extensive data collected from soybean fields. Compared with the independent-scatterer pair distribution, it is found that the hole-correction approximation, which prevents two soybean plants from overlapping each other, is more realistic and improves the agreement between the model calculation and experimental data near normal incidence. Extension to a multiscale branching model can be achieved by recursion.

Historically, the volume scattering effects stimulated the development of the continuous random medium model and the random discrete scattering model for the description of the media. Theoretical treatments were developed along two different paths. Invoking the principle of reciprocity, the wave theory based on Maxwell's equations has been used to calculate the emissivity. The other approach was to start with the radiative transfer equations and solved for the brightness temperatures directly. Attempts have been made to derive the radiative transfer theory from the wave theory. At the same time, both theoretical approaches have been used to calculate the radiometric emissions and to interpret experimentally measured data. The successful interpretation of the Cosmos 243 data was perhaps the first most important step towards a serious development of the continuous random medium model to account for the volume scattering effects of snow ice fields. Subsequent interpretation of measurement results from snow field with both passive radiometers and active radar systems established a unique position for its description of earth terrain media. Recent efforts in classifying sea ice with correlation function characterization are demonstration of acceptance of this model. Future inverse scattering developments will perhaps rely heavily on this model. The emissivity calculations for periodical rough surfaces are also performed and checked against measured data. Recent development in polarimetric active remote sensing with synthetic aperture radar has created significant theoretical results and practical applications. In passive remote sensing, the third and the fourth Stokes parameters for earth remote sensing have not received much attention in the past partly due to the expected small values any measurement can yield. We have made initial calculations and experimental measurements to show that at least the third Stokes parameter can give appreciable number in both theoretical prediction and actual experimentation in a plowed field. Such results may have practical implications in measuring wind directions in ocean waves, for instance. We believe polarimetric passive remote sensing is a viable field which should be explored in light of its potential applications that

may be derived from the full Stokes vector instead of its first two parameters, i.e.,  $T_H$  and  $T_V$ , the horizontally and vertically polarized brightness temperature components.

A multivariate K-distribution, well supported by experimental data, is proposed to model the statistics of fully polarimetric radar clutter of earth terrain. In this approach, correlated polarizations of backscattered radar returns are characterized by a covariance matrix and homogeneity of terrain scatterers is characterized by a parameter  $\alpha$ . As compared with C-, L-, and P- band polarimetric SAR image simultaneously measured by Jet Propulsion Laboratory (JPL) on Mt. Shasta, it is found that  $\alpha$  appears to decrease from C- to P-band for both the forest and burned areas.

The concept of polarimetry in active remote sensing is extended to passive remote sensing. The potential use of the third and fourth Stokes parameters  $U$  and  $V$ , which play an important role in polarimetric active remote sensing, is demonstrated for passive remote sensing. It is shown that, by the use of the reciprocity principle, the polarimetric parameters of passive remote sensing can be obtained through the solution of the associated direct scattering problem. These ideas are applied to study polarimetric passive remote sensing of periodic surfaces. The solution of the direct scattering problem is obtained by an integral equation formulation which involves evaluation of periodic Green's functions and normal derivative of those on the surface. Rapid evaluation of the slowly convergent series associated with these functions is observed to be critical for the feasibility of the method. New formulas, which are rapidly convergent, are derived for the calculation of these series. The study has shown that the brightness temperature of the Stokes parameter  $U$  can be significant in passive remote sensing. Values as high as 50 K are observed for certain configurations.

Classification of sea ice types using polarimetric radar is an area of considerable current interest and research. In this paper, a new classification technique is applied to determine sea ice types in polarimetric and multi-frequency SAR images, utilizing an unsupervised neural network to provide automatic classification, and employing an iterative algorithm to improve the performance. Learning Vector Quantization (LVQ) is first applied for the unsupervised classification of SAR images, and the results are compared with those of the Migrating Means method. Results show that LVQ outperforms the Migrating Means method, which classified most of the pixels into two classes. To further improve the performance, an iterative algorithm is applied where the SAR image is reclassified using the Maximum Likelihood (ML) classifier. It is shown that this algorithm converges, and significantly improves the performance of the unsupervised LVQ method while preserving the advantages of automatic operation inherent in unsupervised techniques.

Monte Carlo simulation of random rough surface is carried out using the Finite-Difference Time-Domain (FDTD) method. The solution domain is truncated using a periodic and an absorbing boundary condition. The advantages of using FDTD include (1) matrix inversion is eliminated. (2) time-domain response is readily available, and (3) scattering intensities for a range of frequencies can be obtained simultaneously.

A random medium model has been applied to interpret the radar backscattering coefficients measured over a soybean canopy. The vegetation is modeled as a random medium containing non spherical scatterers which are soybean leaves. The theoretical results are in good agreement with experimental data. An interesting observation is the high correlation between the canopy fractional volume and the correlation length of the permittivity fluctuations in the horizontal plane. The model is then used to simulate backscattering coefficients of various observation conditions. The results define the different sensitivity domains of radar data to soil moisture and vegetation biomass for inversion consideration.



The multiple species in the random medium are considered as randomly oriented ellipsoids and described by multiple three-dimensional ellipsoidal correlation functions. The variances and correlation lengths of the correlation functions characterize the fluctuation strengths and the physical geometry of the scatterers, respectively. The strong permittivity fluctuation theory is extended to account for the multiple species of ellipsoidal shape. In the random medium, a coincidence of an observation point with a source point gives rise to the singularity of the dyadic Green's function which is properly taken into account with exclusion volumes of the scatterers. Polarimetric scattering properties of a remotely sensed medium are depicted with a covariance matrix whose elements are polarimetric scattering coefficients. The medium has a layer configuration: the top layer such as air is considered as homogeneous, the middle layer such as a vegetation canopy is random, and the underlying layer such as soil is a homogeneous half space. More random medium layers can also be introduced in the configuration to account for weather effect such as fog cover. The *distorted Born* approximation is then used with the effective permittivity to obtain the polarimetric covariance matrix. The result for the cross-polarized return  $\sigma_{hv}$  is non-zero even in the first order approximation. Due to the non-spherical shape and the random orientation of the scatterers, the correlation coefficient between the HH and VV returns has a magnitude different from unity and a small phase. The scattering coefficients are also used to calculate the Mueller matrix for synthesis of polarization signatures. The copolarized signature of the random medium has a rather straight distortion track and a recognizable pedestal.

In passive remote sensing of earth terrain, the Radiative Transfer (RT) theory is widely applied with various types of scattering models to interpret observation. Part of the advantages of the RT theory can be attributed to its simplicity in formulating the reflection and transmission in the presence of boundaries as well as in treating the scattering effect by the incoherent sum of the scattering from each individual scatterer. However, being restricted by this incoherent nature, the RT theory cannot properly take into account the coherent effect which becomes significant at lower frequency in the case of remote sensing of a structured vegetation canopy. Also, in the past, the volume scattering and the surface scattering have been treated separately. A rigorous composite model is thus required to correctly evaluate the volume-surface interactions when the rough surface is visible by the radiometer. We formulated the vector radiative transfer equation for passive microwave remote sensing of a vegetation canopy overlying a soil half-space, and calculated brightness temperatures resulting from microwave thermal emission based on the first order iterative solution. The rough surface boundary condition has been integrated into this model through the coupling matrix for the boundary between the vegetation layer and soil such that the interactions between volume scattering and surface scattering are rigorously included. A randomly distributed stem-leave model is employed to construct the phase matrix such that the effects of coherence and multi-scale can be properly accounted for.

We have applied the radiative transfer theory to vegetation with clustered structures. To take into account vegetation structure in the radiative transfer theory, the phase matrix of a vegetation cluster is calculated by incorporating the phase interference of scattered fields from every components. Subsequently, the resulting phase matrix is used in the radiative transfer equations to evaluate the polarimetric backscattering coefficients from a layer of medium embedded with vegetation clusters. Theoretical results are illustrated for various kinds of vegetation clusters. It is found that the simulated polarization, frequency, and angular responses carry significant information regarding the structure of vegetation

clusters. The theoretical results will also be compared with the signatures observed in multi-frequency polarimetric synthetic aperture radar images.

Classification of terrain cover using polarimetric radar is an area of considerable current interest and research. A number of methods have been developed to classify ground terrain types from fully polarimetric Synthetic Aperture Radar (SAR) images, and these techniques are often grouped into supervised and unsupervised approaches. Supervised methods, including both conventional Maximum Likelihood (ML) and more recent Multi-layer Perceptron classifiers, have yielded higher accuracy than unsupervised techniques, but suffer from the need for human interaction to predetermine classes and training regions. In contrast, unsupervised methods determine classes automatically, but generally show limited ability to accurately divide terrain into natural classes. In this paper, a new terrain classification technique is introduced, utilizing unsupervised neural networks to provide automatic classification, but employing an iterative algorithm which overcomes the poor accuracy of other unsupervised techniques.

In remote sensing, the encountered geophysical media such as agricultural canopy, forest, snow, or ice are inhomogeneous and contain scatterers in a random manner. Furthermore, weather conditions such as fog, mist, or snow cover can intervene the electromagnetic observation of the remotely sensed media. In the modelling of such media accounting for the weather effects, a multi-layer random medium model has been developed. The scattering effects of the random media are described by three-dimensional correlation functions with variances and correlation lengths corresponding to the fluctuation strengths and the physical geometry of the inhomogeneities, respectively. With proper consideration of the dyadic Green's function and its singularities, the strong fluctuation theory is used to calculate the effective permittivities which account for the modification of the wave speed and attenuation in the presence of the scatterers. The distorted Born approximation is then applied to obtain the correlations of the scattered fields. From the correlation of the

scattered field, calculated are the complete set of scattering coefficients for polarimetric radar observation or brightness temperature in passive radiometer applications.

Polarimetric calibration algorithms using combination of point targets and reciprocal distributed targets are developed. From distributed target reciprocity, derived is an equivalent point target response. Then the problem of polarimetric calibration using two point targets and one distributed target reduces to that using three point targets, which has been solved in previous research. Regarding the calibration using one point target and one reciprocal distributed target, analyzed are two cases with the point target being a trihedral reflector or a Polarimetric Active Radar Calibrator (PARC). For both cases, the general solutions of the system distortion matrices are written as a product of a particular solution and a matrix with one free parameter. For the trihedral-reflector case, this free parameter is determined by assuming azimuthal symmetry for the distributed target. For the PARC case, knowing one ratio of two covariance matrix elements of the distributed target is required to solve the free parameter.

Finite difference techniques have been applied to analyze various electromagnetic problems in both frequency and time domains. Examples of these applications include scattering and radiation, microwave and millimeter wave circuits, and hyperthermia. Besides the widespread applications, the latest research efforts have been directed at achieving more accurate discretization schemes, improving absorbing boundary conditions for open region problems, and efficient implementations on supercomputers.

We also developed a Finite-Difference Time-Domain (FD-TD) scheme on triangular grids. The discretization scheme is based on the combination of the finite difference and control region approximations. The flexibility of the triangular grid is utilized to provide more accurate target modeling capability than the traditional FD-TD technique of the rectangular grid.

Fully polarimetric scattering of electromagnetic waves from snow and sea ice is studied with a layered random medium model and applied to interpret experimental data obtained under laboratory controlled conditions. The snow layer is modeled as an isotropic random medium. The sea ice is described as an anisotropic random medium due to the elongated form of brine inclusions. The underlying sea water is considered as a homogeneous half-space. The scattering effects of both random media are described by three-dimensional correlation functions with variances and correlation lengths corresponding to the fluctuation strengths and the physical geometry of the inhomogeneities, respectively. The strong fluctuation theory is used to calculate the effective permittivities of the random media. The distorted Born approximation is then applied to obtain the covariance matrix which describes the fully polarimetric scattering properties of the remotely sensed media.

Polarimetric scattering measurements have been from the simulated bare sea ice in CRREL, and the two-layer configuration is used to model this experimental set-up. The distinction on the characteristics of the media are investigated with the conventional backscattering coefficients and the complex correlation coefficient  $\rho$  between  $\sigma_{hh}$  and  $\sigma_{vv}$ . For ice-type identification, the measured covariance matrices are studied with the model to infer the physical characteristics pertaining to the different ice types. The three-layer configuration is then used to investigate the effects on fully polarimetric radar returns from snow covered sea ice.

There is also considerable interest in identifying and classifying ice types by using polarimetric scattering data. Due to differences in structure and composition, ice of different types such as frazil, first-year, or multi-year can have different polarimetric scattering behaviors. To study the polarimetric response of sea ice, the layered random medium model is used. In this model, the sea-ice layer is described as an anisotropic random medium composed of a host medium with randomly embedded inhomogeneities, such as

elongated brine inclusions, which can have preferred orientation direction. The underlying sea-water layer is considered as a homogenous half space. The scattering effect of the inhomogeneities in the sea ice are characterized by three-dimensional correlation function with variance and correlation lengths respectively corresponding to the fluctuation strength and the physical geometry of the scatterers. The effective permittivity of the sea ice is calculated with the strong fluctuation theory and the polarimetric backscattering coefficients are obtained under the distorted Born approximation. The distinction on the characteristics of different ice types are investigated with the conventional backscattering coefficients and the complex correlation coefficient  $\rho$  between  $\sigma_{hh}$  and  $\sigma_{vv}$ . The correlation coefficient  $\rho$  contains additional information on the sea-ice structure and can be useful in the identification of the ice types. By relating to the covariance matrices, the model is used to explain the polarization signatures of different ice types. In the case of snow-covered sea ice, the snow layer is modeled as an isotropic random medium and the obtained solution accounts for the effect of snow cover on polarimetric scattering properties of sea ice.

The layered random medium model is used to investigate the fully polarimetric scattering of electromagnetic waves from vegetation. The vegetation canopy is modeled as an anisotropic random medium containing nonspherical scatterers with preferred alignment. The underlying medium is considered as a homogeneous half space. The scattering effect of the vegetation canopy are characterized by three-dimensional correlation functions with variances and correlation lengths respectively corresponding to the fluctuation strengths and the physical geometries of the scatterers. The strong fluctuation theory is used to calculate the anisotropic effective permittivity tensor of the random medium and the distorted Born approximation is then applied to obtain the covariance matrix which describes the fully polarimetric scattering properties of the vegetation field. This model accounts for all the interaction processes between the boundaries and the scatterers and includes all the coherent effects due to wave propagation in different directions such as the constructive and destructive interferences. For a vegetation canopy with low attenuation, the boundary

between the vegetation and the underlying medium can give rise to significant coherent effects.

The model is used to interpret the measured data for vegetation field such as rice, wheat, or soybean over water or soil. The temporal variation of  $\sigma_{hh}$  and  $\sigma_{vv}$  of the X-band SAR data of rice fields shows a wide range of responses at different growth stages. From the data of wheat, recognizable changes of the angular and polarization behaviour of the backscattering coefficients are observed at X-band before and after the heading of the wheat. For soybean, the data collected during the growing season shows similar results for both  $h$ - and  $v$ -polarizations. The observed effects on backscattering coefficients of the vegetation structural and moisture conditions at different growth stages can be explained by analyzing the different interaction processes pointed out by the model.

Accurate calibration of polarimetric radar systems is essential for the polarimetric remote sensing of earth terrain. A polarimetric calibration algorithm using three arbitrary in-scene reflectors is developed. The transmitting and receiving ports of the polarimetric radar are modeled by two unknown polarization transfer matrices. These unknown matrices are determined using the the measured scattering matrices from the calibration targets. A Polarization-Basis Transformation technique is introduced to convert the scattering matrices of the calibration targets into one of the six sets of targets with simpler scattering matrices. Then, the solution to the original problem can be expressed in terms of the solution obtained using the simpler scattering matrices. The uniqueness of polarimetric calibration using three targets is addressed for all possible combinations of calibration targets. The effect of misalignment of the calibration targets and the sensitivity of the polarimetric calibration algorithm to the noise are illustrated by investigating several sets of calibration targets in detail.

In the interpretation of active and passive microwave remote sensing data from earth terrain, the random medium model has been shown to be quite successful. In the random medium model, a correlation function is used to describe the random permittivity fluctuations with associated mean and variance. In the past, the correlation functions used were either assumed to be of certain form or calculated from cross sectional pictures of scattering media. We calculate the correlation function for a random collection of discrete scatterers imbedded in a background medium of constant permittivity. Correlation functions are first calculated for the simple cases of the uniform distribution of scatterers and the uniform distribution with the hole correction. Then, the correlation function for a more realistic case is obtained using the Percus-Yevik pair distribution function. Once the correlation function is obtained, the strong fluctuation theory is used to calculate the effective permittivities. Then, the distorted Born approximation is used to calculate the backscattering coefficients from a halfspace configuration. The theoretical results are illustrated by comparing the effective permittivities and the backscattering coefficients with the results obtained with the discrete scatterer theory.

Strong permittivity fluctuation theory has been used to solve the problem of scattering from a medium composed of completely randomly oriented scatterers under the low frequency limit. Based on Finkel'berg's approach, Gaussian statistics is not assumed for the renormalized scattering sources. The effective permittivity is obtained under the low frequency limit and the result is shown to be isotropic due to no preferred direction in the orientation of the scatterers. Numerical results of the effective permittivity are illustrated for oblate and prolate spheroidal scatterers and compared with the results for spherical scatterers. The results derived are shown to be consistent with the discrete scatterer theory. The effective permittivity of random medium embedded with nonspherical scatterers shows a higher imaginary part than that of spherical scatterer case with equal correlation volume. Under the distorted Born approximation, the polarimetric covariance matrix for the backscattered electric field is calculated for the half-space randomly oriented scatterers.



The nonspherical geometry of the scatterers shows significant effects on the cross-polarized backscattering returns  $\sigma_{hv}$  and the correlation coefficient  $\rho$  between HH and VV returns. The polarimetric backscattering scattering coefficients can provide useful information in distinguishing the geometry of scatterers. A polarimetric radar calibration algorithm using three in-scene reflectors is developed based on the exact solution for general target choices. The transmitting and receiving ports of the polarimetric radar are modeled by two unknown polarization transfer matrices. These transfer matrices are solved in terms of measurements from three independent calibration targets with known scattering matrices. The solutions for several sets of calibration targets with simple scattering matrices are presented first. Then, when at least two of the target scattering matrices can be simultaneously diagonalized, polarimetric calibration is derived using the method of simultaneous diagonalization of two matrices. A transformation matrix is found to convert the general scattering matrices into the simple cases, and the problem is solved in the transformed domain. The solution to the original problem then can be expressed in terms of the solutions obtained for the simple scattering matrices. All possible combinations of calibration targets are discussed and the solutions are presented for the cases that at least two of the scattering matrices can be simultaneously diagonalized.

Conventional classification techniques for identification of vehicle types from their range profiles, or pulse responses, have been shown to be limited in their practical ability to distinguish targets of interest. These limitations arise from the need for large signature libraries and time consuming processing for profile matching algorithms, and from the assumptions made toward the statistics of extracted features for parametric methods. To overcome the practical constraints of existing techniques, a new method of target recognition is examined which utilizes neural nets. The effectiveness of this neural net classifier is demonstrated with synthetically generated range profiles for two sets of geometries, as produced using RCS prediction techniques. The first set consists of three simple canonical geometries for which RCS predictions can be done directly. For these targets, two neural

net configurations are compared, and the effects of varied aspect sampling density for the training profiles and noise corruption in the test profiles are demonstrated. Comparisons are made between the neural net classifier and several conventional techniques to determine the relative performance and cost of each algorithm. A similar set of comparisons is performed for the second group of targets consisting of more realistic air vehicle models, each composed from a collection of canonical shapes. In both cases, the neural net classifier is shown to match or exceed the performance of conventional algorithms while offering a more computationally efficient implementation.

Earth terrains are modeled by a two-layer configuration to investigate the polarimetric scattering properties of the remotely sensed media. The scattering layer is a random medium characterized by a three-dimensional correlation function with correlation lengths and variances respectively related to the scatter sizes and the permittivity fluctuation strengths. Based on the wave theory with Born approximations carried to the second order, this model is applied to derive the Mueller and the covariance matrices which fully describe the polarimetric scattering characteristics of the media. Physically, the first- and second-order Born approximations account for the single and double scattering processes. For an isotropic scattering layer, the five depolarization elements of the covariance matrix are zero under the first-order Born approximation. For the uniaxial tilted permittivity case, the covariance matrix does not contain any zero elements. To account for the randomness in the azimuthal growth direction of leaves in vegetation, the backscattering coefficients are azimuthally averaged. In this case, the covariance matrix contains four zero elements although the tilt angle is not zero. Under the second-order Born approximation, the covariance matrix is derived for the isotropic and the uniaxial untilted random permittivity configurations. The results show that the covariance matrix has four zero elements and a depolarization factor is obtained even for the isotropic case. To describe the effect of the random medium on electromagnetic waves, the strong permittivity fluctuation theory, which accounts for the losses due to both of the absorption and the scattering, is used to

compute the effective permittivity of the medium. For a mixture of two components, the frequency, the correlation lengths, the fractional volume, and the permittivities of the two constituents are needed to obtain the polarimetric backscattering coefficients. Theoretical predictions are illustrated by comparing the results with experimental data for vegetation fields and sea ice.

The random medium model with three-layer configuration is developed to study fully polarimetric scattering of electromagnetic waves from geophysical media. This model can account for the effects on wave scattering due to weather, diurnal and seasonal variations, and atmospheric conditions such as ice under snow, meadow under fog, and forest under mist. The top scattering layer is modeled as an isotropic random medium which is characterized by a scalar permittivity. The middle scattering layer is modeled as an anisotropic random medium with a symmetric permittivity tensor whose optic axis can be tilted due to the preferred alignment of the embedded scatterers. The bottom layer is considered as a homogeneous half-space. Volume scattering effects of both random media are described by three-dimensional correlation functions with variances and correlation lengths corresponding to the strengths of the permittivity fluctuations and the physical sizes of the inhomogeneities, respectively. The strong fluctuation theory is used to derive the mean fields in the random media under the bilocal approximation with singularities of the dyadic Green's functions properly taken into account and effective permittivities of the random media are calculated with two-phase mixing formulas. The distorted Born approximation is then applied to obtain the covariance matrix which describes the fully polarimetric scattering properties of the remotely sensed media.

The three-layer configuration is first reduced to two-layers to observe fully polarimetric scattering directly from geophysical media such as snow, ice, and vegetation. Such media exhibit reciprocity as experimentally manifested in the close proximity of the measured backscattering radar cross sections  $\sigma_{vh}$  and  $\sigma_{hv}$  and theoretically established in the random medium model with symmetric permittivity tensors. The theory is used to investigate the signatures of isotropic and anisotropic random media on the complex correlation coefficient  $\rho$  between  $\sigma_{hh}$  and  $\sigma_{vv}$  as a function of incident angle. For the isotropic random medium,  $\rho$  has the value of approximately 1.0. For the untilted anisotropic random medium,  $\rho$  has complex values with both the real and imaginary parts decreased as the incident angle is increased. The correlation coefficient  $\rho$  is shown to contain information about the tilt of the optic axis in the anisotropic random medium. As the tilted angle becomes larger, the magnitude of  $\rho$  is maximized at a larger incident angle where the phase of  $\rho$  changes its sign. It should be noted that the tilt of the optic axis is also related to the nonzero depolarization terms in the covariance matrix.

The effects on polarimetric wave scattering due to the top layer are identified by comparing the three-layer results with those obtained from the two-layer configuration. The theory is used to investigate the effects on polarimetric radar returns due to a low-loss and a lossy dry-snow layers covering a sheet of thick first-year sea ice. For the low-loss snow cover, both  $\sigma_{hh}$  and  $\sigma_{vv}$  are enhanced compared to those observed from bare sea ice. Furthermore, the boundary effect is manifested in the form of the oscillation on  $\sigma_{hh}$  and  $\sigma_{vv}$ . The oscillation can also be seen on the real and imaginary parts of the correlation coefficient  $\rho$ . The magnitude of  $\rho$ , however, does not exhibit the oscillation while clearly retaining the same characteristics as observed directly from the uncovered sea ice. In contrast to the low-loss case, the lossy top layer can diminish both  $\sigma_{hh}$  and  $\sigma_{vv}$  and depress the boundary-effect oscillation. When the thickness of the lossy top layer increases, the behavior of the correlation coefficient  $\rho$  becomes more and more similar to the isotropic

case signifying that the information from the lower anisotropic layer is masked. At appropriate frequency, the fully polarimetric volume scattering effects can reveal the information attributed to the lower layer even if it is covered under another scattering layer. Due to the physical base, the random medium model renders the polarimetric scattering information useful in the identification, classification, and radar image simulation of geophysical media.

Polarimetric radar backscatter data observed with satellite and airborne synthetic aperture radars (SAR) have demonstrated potential applications in geologic mapping and terrain cover classification. Accurate calibration of such polarimetric radar systems is essential for polarimetric remote sensing of earth terrain. A polarimetric calibration algorithm using three in-scene reflectors has been developed which will be a useful tool in the radar image interpretation.

The transmitting and receiving ports of the polarimetric radar are modeled by two unknown polarization transfer matrices. The measured scattering matrix is equal to the product of the transfer matrix of the receiving port, scattering matrix of the illuminated target, the transfer matrix of the transmitting port, and a common phase factor. The objective of polarimetric radar calibration is to determine these two unknown polarization transfer matrices using measurements from targets with known scattering matrices.

The transfer matrices for the transmitting and receiving ports are solved in terms of measurements from three in-scene reflectors with arbitrary known scattering matrices. The solutions for several sets of calibration targets with simple scattering matrices are first presented. Then, the polarimetric calibration using three targets with general arbitrary scattering matrices is derived using the method of simultaneous diagonalization of two matrices. A transformation matrix is found to convert the general scattering matrices into the simple cases, and the problem is solved in the transformed domain. The solutions to the original problem then can be expressed in terms of the solutions obtained for the simple scattering matrices. All possible combinations of calibration targets are discussed and the

solutions of each case are presented. Thus, if three scatterers with known scattering matrices are known to exist within a radar image, then the whole image can be calibrated using the exact solution presented. The effects of misalignment of calibration targets and of receiver noise are also illustrated for several sets of calibration targets.

A multivariate K-distribution is proposed to model the statistics of fully polarimetric radar data from earth terrain with polarizations HH, HV, VH, and VV. In this approach, correlated polarizations of radar signals, as characterized by a covariance matrix, are treated as the sum of  $N$   $n$ -dimensional random vectors;  $N$  obeys the negative binomial distribution with a parameter  $\alpha$  and mean  $\bar{N}$ . Subsequently, an  $n$ -dimensional K-distribution, with either zero or nonzero mean, is developed in the limit of infinite  $\bar{N}$  or illuminated area. The Probability Density Function (PDF) of the K-distributed vector normalized by its Euclidean norm is independent of the parameter  $\alpha$  and is the same as that derived from a zero-mean Gaussian-distributed random vector. The above model is well supported by experimental data provided by MIT Lincoln Laboratory and the Jet Propulsion Laboratory in the form of polarimetric measurements. The results are illustrated by comparing the higher-order normalized intensity moments and Cumulative Density Functions (CDF) of the experimental data with theoretical results of the K-distribution.

The three-layer random medium model is developed for microwave remote sensing of snow-covered sea ice. The electromagnetic wave theory and strong fluctuation theory are employed to study the propagation and volume scattering of electromagnetic waves in the medium. With the application of the Feynman diagrammatic technique and the renormalization method, mean fields for the isotropic and anisotropic random media are derived under the bilocal approximation. Then, the effective permittivities for both random media are obtained from the dispersion relations of the mean fields. Further, with the discrete-scatterer concept for two-phase mixtures, the scattering parts of effective permittivities are computed, in the low-frequency limit, for both isotropic and anisotropic random media

with specified correlation functions. The distorted Born approximation is then used to compute the co-polarized and cross-polarized backscattering coefficients which are compared with scatterometer data at 9 and 13 GHz for bare and dry-snow covered thick first year sea ice taken at Point Barrow, NWT.

For active and passive microwave remote sensing, the correlation function used in the random medium model provides a direct link between electrical behaviors and physical properties of geophysical media. The distribution, shape, size, and orientation of embedded inhomogeneities, such as ice grains in snow and brine inclusions in sea ice, can be characterized by the functional form of the correlation function, the variance, and the correlation lengths. Based on the probability theory, analytical expressions of correlation functions for two-phase mixtures with randomly distributed inclusions of spherical and spheroidal shapes are derived. It is shown that the functional form of the correlation function is determined by the shape and orientation of inclusions while correlation lengths are related to the fractional volume of the scatterers and the total common surface area.

Supervised and unsupervised classification procedures are developed and applied to Synthetic Aperture Radar (SAR) polarimetric images in order to identify their various earth terrain components. For supervised classification processing, the Bayes technique is used to classify fully polarimetric and normalized polarimetric SAR data. Simpler polarimetric discriminates, such as the absolute and normalized magnitude response of the individual receiver channel returns, in addition to the phase difference between the receiver channels, are also considered. Another processing algorithm, based on comparing general properties of the Stokes parameters of the scattered wave to that of simple scattering models, is also discussed. This algorithm, which is an unsupervised technique, classifies terrain elements based on the relationship between the orientation angle and handedness of the transmitting and receiving polarization states. These classification procedures have been applied to San Francisco Bay and Traverse City SAR images, supplied by the Jet

Propulsion Laboratory. It is shown that supervised classification yields the best overall performance when accurate classifier training data is used, whereas unsupervised classification is applicable when training data is not available.

There is considerable interest in determining the optimal polarizations that maximize contrast between two scattering classes in polarimetric radar images. A systematic approach is developed to obtain the optimal polarimetric matched filter, i.e., that filter which produces maximum contrast between two scattering classes. The maximization procedure involves solving an eigenvalue problem where the eigenvector corresponding to the maximum contrast ratio is optimal polarimetric matched filter. To exhibit the physical significance of this filter, it is transformed into its associated transmitting and receiving polarization states, written in terms of horizontal and vertical vector components. For the special case where the transmitting polarization is fixed, the receiving polarization which maximizes the contrast ratio is also obtained. Polarimetric filtering is then applied to synthetic aperture radar images obtained from the Jet Propulsion Laboratory. It is shown, both numerically and through the use of radar imagery, that maximum image contrast can be realized when data is processed with the optimal polarimetric matched filter.

Earth terrains are modeled by a two-layer configuration with a random permittivity described by a three-dimensional correlation function horizontal and vertical correlation lengths and variances. Using the wave theory with Born approximations carried to the second order, this model is applied to derive the polarimetric backscattering coefficients of the Mueller and covariance matrices. From a physical point of view, the Born first- and second-order approximations account for the single and double scattering processes, respectively.



For the isotropic random permittivity configuration, five out of the nine elements of the covariance matrix are zero under the Born first-order approximation. For the uniaxial tilted random permittivity case, the covariance matrix does not contain any zero elements. Furthermore, in order to account for different directions of scattering especially for vegetation, an averaging scheme is developed in which the backscattering coefficients are averaged over the azimuthal direction. In this case, the covariance matrix is described by four zero elements though the tilt angle is different from zero. Applying the Born approximation to the second-order, the covariance matrix is computed for the isotropic and the uniaxial untilted random permittivity configurations. The covariance matrix has four zero elements, and a depolarization factor is obtained, even for the isotropic case.

To describe the effect of the random medium on electromagnetic waves, the strong permittivity fluctuation theory, which accounts for the losses due to both of the absorption and the scattering, is used to compute the effective permittivity of the medium. For a mixture of two components, only the frequency, the correlation lengths, the fractional volume, and the permittivities of the two constituents are needed to obtain the polarimetric backscattering coefficients. Theoretical predictions are illustrated by comparing the results with experimental data for vegetation fields and sea ice.

A mathematically rigorous and fully polarimetric radar clutter model is developed to evaluate the radar backscatter from various types of terrain clutter such as forested areas, vegetation canopies, snow covered terrains, or ice fields. With this model, we can calculate the radar backscattering coefficients ( $\sigma^0$ ) for the multi-channel polarimetric radar returns, in addition to the complex cross correlation coefficients between elements of the polarimetric measurement vector. The complete polarization covariance matrix can be computed and the scattering properties of the clutter environment characterized over a broad range of incident angles and frequencies.

Algorithms have been developed to identify and classify different features in polarimetric SAR images. Optimal schemes are designed to enhance radar target detection and discrimination. The fully polarimetric, multi-frequency, multi-incident angle, and multi-layer random medium model are employed in the evaluation of synthetic clutter signatures that can be used in a hardware-in-the-loop test system. With the Generalized K-distribution, better description of the statistics of the polarimetric SAR data are obtained. The identification and classification procedures have been applied to JPL polarimetric SAR images containing different features. RCS codes are improved to predict radar cross sections from various targets. Practically, the developments reported in this document are highly applicable to the target-clutter detection problems such as land mines disguised under vegetation or soil covers.

Earth terrain media, such as vegetation, forest, snow, and ice exhibit strong volume scattering effects. To study polarimetric radar backscatter of earth terrains from the point of view of electromagnetic wave theory, we use a layered random medium model to characterize the terrain clutter. The random medium is described by a background permittivity with a fluctuating component; the randomness of the fluctuation is characterized by a three-dimensional correlation function with a variance and horizontal and vertical correlation lengths. The variance corresponds to the strength of the fluctuation, whereas the correlation lengths coincide with the geometrical size of the basic scattering elements. The polarimetric backscattering coefficients can be obtained from the electromagnetic wave theory by calculating the covariance matrix of the polarimetric measurement vector.

The problem of scattering by a layer of random medium (e.g. snow field, meadow, etc.) can be solved with a number of different techniques. We developed a wave approach by applying the Born approximation. An integral equation is formulated for the electric field by using the unperturbed Green's function for a layered random medium in the absence of permittivity fluctuations. The random fluctuations are treated as induced scattering sources in the integral equation, which will then be solved by iteration to obtain a Neumann series. To include the depolarization effects, the Born approximation is carried out to the second order. Physically, the Born first-order and second-order approximations account, respectively, for a single and double scattering process. The calculated covariance matrix for a layered isotropic random medium has four of its elements equal to zero, indicating absence of correlation between the HV and HH terms and HV and VV terms. The theoretical results are shown to be consistent with measurement data obtained from the MIT Lincoln Laboratory.

With the same approach, the polarimetric scattering effects from a layer of anisotropic random medium (e.g. sea ice) or from a layer of isotropic random medium on top of another layer of anisotropic random medium (e.g. tree canopy, snow-covered sea ice, etc.) are investigated and the complete covariance matrices with nine non-zero elements are computed. Theoretically calculated covariance matrices will be compared with experimental polarimetric HH, HV, and VV clutter data collected from the various terrains. Physical interpretations will be illustrated along with the other properties of the covariance matrix elements.

The evaluation of clutter backscatter coefficients for HH, HV and VV polarimetric returns is useful in the design and analysis of optimal radar target detection, discrimination and classification schemes. Another important application is the generation of random clutter returns for Monte-Carlo simulations. The application of the fully polarimetric clutter model in the terrain classification will be illustrated. The optimal (Bayes) fully polarimetric and normalized polarimetric classifiers as well as simpler polarimetric discriminants will also be presented. In addition, the optimal polarimetric matched filter will be introduced as a means of enhancing the contrast between two areas within radar polarimetry. Fully polarimetric synthetic aperture radar images, obtained from the Jet Propulsion Laboratory, will be used to demonstrate various terrain classification schemes and the contrast enhancement obtained using the polarization matched filter.

A clutter model is used to simulate fully polarimetric returns for a coherent, stepped-frequency radar. The objective is to create site-dependent synthetic clutter signatures that can be utilized in a hardware-in-the-loop test system. The fully polarimetric, multi-frequency, and multi-incident angle two-layer anisotropic random medium model is employed to compute the normalized backscatter coefficients of terrain clutter. Polarization covariance matrices are calculated for each of  $N$  high resolution range bins, at each of the  $M$  discrete frequencies that comprise the stepped-frequency bandwidth. The covariance matrices are decomposed, multiplied by complex Gaussian noise, and weighted according to the random product model to account for the spatial variability of clutter. This generates the normalized electric field backscattered from each of the  $N$  range bins, at each of the  $M$  discrete frequencies. These fields are coherently added, taking into account the effects of terrain shadowing and overlay, in order to realize the single-frequency polarimetric return that a radar would measure from the specified terrain. The radar return for each of the other discrete frequencies is computed in a similar manner. In addition, the real-time implementation of this algorithm is considered in the context of synthetic wide-band processing. The result of this procedure yields the clutter's coherent phase-history

profile. The clutter phase-history returns can then be coherently superimposed on the target phase-history returns. The combined (or clutter only) returns can be reduced to obtain either (1) the coherent high resolution range profile (HRRP) or (2) the noncoherent autocorrelation range profile.

Existing radar cross section (RCS) prediction algorithms using the Physical Optics and the Physical Theory of Diffraction techniques have been shown to give erroneous results for cases in which multiple scattering between portions of the target is significant. In particular, double reflections between flat plate surfaces are important for geometries resembling the corner reflector, and this effect is neglected by current algorithms which include only single surface interactions. To overcome this limitation a method is presented of extending the conventional results obtained using Physical Optics to include a field due to double reflections between two polygonal plate surfaces.

An integral expression is derived, applying the tangent plane approximation at each surface, and correctly accounting for the potentially near-field interactions between the two perfectly conducting plates. The initial complexity of this expression necessitates numerical evaluation of the integrals and results in a large computational burden. The requirement of numerical integration is eliminated, however, by applying the method of Stationary Phase and expanding quadratically the exact inter-plate phase term. The two surface integrations are replaced by line integrals using Stokes' Theorem, and for polygonal plates, the contour is subdivided into linear segments on which the integration is performed analytically. In the case where the conducting plates are loaded with one or more layers of dielectric, the equivalent electric and magnetic surface currents are derived using the reflection coefficients at each plate.

The resulting field expressions are derived with sufficient generality so as to permit incorporation in standard RCS prediction codes allowing arbitrary geometry and illumination. Comparisons with measurements of several simple two-plate targets confirm the accuracy of the predicted field and demonstrate a significant improvement over existing algorithms which neglect multiple reflections or which assume a far field interaction between the surfaces.

Polarimetric radar backscatter data have been used extensively to classify terrain cover. Since it is difficult to calibrate out the effects of amplitude and phase errors induced by atmospheric effects, path loss, etc., absolute amplitude and phase of radar returns are not reliable features for terrain classification purposes. The use of normalized polarimetric data is proposed such that only the relative magnitudes and phases will be utilized to discriminate different terrain elements. It is shown that the Bayes classification error does not depend on the form of the normalization function if the unknown radar system calibration factor is modeled as a multiplicative term in the received signal. Assuming a multivariate Gaussian distribution for the un-normalized polarimetric data, the Probability Density Function (PDF) of the normalized data and the corresponding Bayes classifier distance measure for the normalized data are derived. Furthermore, by assuming a specific form of the covariance matrix for the polarimetric data, exact PDFs are given for HH, HV, VV and span type normalization schemes. Corresponding classification errors are evaluated to verify their independence from all normalization functions.

The scattering of electromagnetic waves from a randomly perturbed periodic surface is formulated by the Extended Boundary Condition (EBC) method and solved by the Small Perturbation Method (SPM). The scattering from periodic surface is solved exactly and this solution is used in the SPM to solve for the surface currents and scattered fields up to the second order. The random perturbation is modeled as a Gaussian random process. The theoretical results are illustrated by calculating the bistatic and backscattering

coefficients. It is shown that as the correlation length of the random roughness increases, the bistatic scattering pattern of the scattered fields show several beams associated with each Bragg diffraction direction of the periodic surface. When the correlation length becomes smaller, then the shape of the beams become broader. The results obtained using the EBC/SPM method is also compared with the results obtained using the Kirchhoff approximation. It is shown that the Kirchhoff approximation results show quite a good agreement with EBC/SPM method results for the hh and vv polarized backscattering coefficients for small angles of incidence. However, the Kirchhoff approximation does not give depolarized returns in the backscattering direction whereas the results obtained using the EBC/SPM method give significant depolarized returns when the incident direction is not perpendicular to the row direction of the periodic surface.

A general mixing formula is derived for discrete scatterers immersed in a host medium. The inclusion particles are assumed to be ellipsoidal. The electric field inside the scatterers is determined by quasistatic analysis, assuming the diameter of the inclusion particles to be much smaller than the wavelength. The results are applicable to general multiphase mixtures, and the scattering ellipsoids of the different phases can have different sizes and arbitrary ellipticity distribution and axis orientation, i.e., the mixture may be isotropic or anisotropic. The resulting mixing formula is nonlinear and implicit for the effective complex dielectric constant, because the approach in calculating the internal field of scatterers is self-consistent. Still, the form is especially suitable for iterative solution. The formula contains a quantity called the apparent permittivity, and with different choices of this quantity, the result leads to the generalized Lorentz - Lorenz formula, the generalized Polder - van Santen formula, and the generalized coherent potential - quasicrystalline approximation formula.

We have used the strong fluctuation theory to derive the backscattering cross sections. The study of the strong fluctuation theory for a bounded layer of random discrete scatterers is further extended to include higher order co-polarized and cross-polarized second moments. The backscattering cross sections per unit area are calculated by including the mutual coherence of the fields due to the coincidental ray paths and that due to the opposite ray paths which are corresponding to the ladder and cross terms in the Feynman diagrammatic representation. It is proved that the contributions from ladder and cross terms for co-polarized backscattering cross sections are the same, while the contributions for the cross-polarized ones are of the same order. The bistatic scattering coefficients in the second-order approximation for both the ladder and cross terms are also obtained. The enhancement in the backscattering direction can be attributed to the contributions from the cross terms.

A two-layer anisotropic random medium model is developed for the active and passive microwave remote sensing of ice fields. The dyadic Green's function for this two-layer anisotropic medium is derived. With a specified correlation function for the randomness of the dielectric constant, the backscattering cross sections are calculated with the Born approximation. It is shown that the depolarization effects exist in the single-scattering process and that the backscattering cross section of horizontal polarization can be greater than that of vertical polarization even in the half-space case. The principle of reciprocity and the principle of energy conservation are invoked to calculate the brightness temperatures. The bistatic scattering coefficients are first calculated and then integrated over the upper hemisphere to be subtracted from unity, in order to obtain the emissivity for the random medium layer. It is shown that both the absorptive and randomly fluctuating properties of the anisotropic medium affect the behavior of the resulting brightness temperatures both in theory and in actual controlled field measurements. The active and passive results match favorably well with the experimental data obtained from the corn stalks with detailed ground-truth information.



The vegetation canopy and snow-covered ice field have been studied with a three-layer model, an isotropic random medium layer overlying an anisotropic random medium. We have calculated the dyadic Green's functions of the three-layer medium and the scattered electromagnetic intensities with Born approximation. The backscattering cross sections are evaluated for active microwave remote sensing. The theoretical approach can be extended to derive the bistatic scattering coefficients.

Backscattering and propagation of electromagnetic pulses with different shapes in earth terrain media such as snow-ice, vegetation, and forest are studied with the random medium model. The backscattering cross sections are computed with both the Born and the distorted Born approximations. We study the pulse shape distortion by considering a two-layer random medium model with different correlation lengths and varying variances. The degree of distortion is inversely proportional to the pulse width and determined by the magnitude of the randomly fluctuating permittivity strength. Both the like-polarized and cross-polarized radar backscattering coefficients are examined and illustrated.

## PUBLICATIONS SUPPORT BY WATERWAYS EXPERIMENTAL STATION

Applications of EMSARS background model to MMW vegetation scattering simulation (C. C. Hsu, Y. E. Yang, R. T. Shin, J. A. Kong, C. Kohler, T. Nguyen, H. Nguyen, and J. Ho), 3rd Ground Target Modeling and Validation Conference, Michigan Technical University, Houghton, MI, August 18-20, 1992.

External calibration of polarimetric radars using point and distributed targets (S. H. Yueh, J. A. Kong, and R. T. Shin), *Journal of Electromagnetic Waves and Applications*, Vol. 6, No. 7, 1992.

Simulation of forest backscatter as a function of forest and ground parameters (A. Beaudoin, T. Le Toan, C. C. Hsu, H. C. Han, J. A. Kong, and R. T. Shin), International Geoscience and Remote Sensing Symposium, Houston, Texas, USA, May 26-29, 1992.

Branching model for vegetation (S. H. Yueh, J. A. Kong, J. K. Jao, R. T. Shin, and T. Le Toan), *IEEE Transactions on Geoscience and Remote Sensing*, Vol. 30, No. 2, 390-402, March 1992.

Theoretical modeling for passive microwave remote sensing of earth Terrain (J. A. Kong), URSI Specialists Meeting on Microwave Radiometry and Remote Sensing, Boulder, Colorado, January 24-26, 1992.

Theoretical models for polarimetric microwave remote sensing of earth terrain (M. Borgeaud, J. A. Kong, R. T. Shin, and S. V. Nghiem), in *Direct and Inverse Methods in Radar Polarimetry, Part 2*, 1139-1190, Kluwer Academic Publishers, The Netherlands, 1992.

K-distribution and multi-frequency polarimetric terrain radar clutter (H. A. Yueh, J. A. Kong, J. K. Jao, R. T. Shin, H. A. Zebker, and T. Le Toan), *Journal of Electromagnetic Waves and Applications*, Vol. 5, No. 1, pp. 1-15, 1991.

Polarimetric passive remote sensing of periodic surfaces (M. E. Veysoglu, H. A. Yueh, R. T. Shin and J. A. Kong), *Journal of Electromagnetic Waves and Applications*, Vol. 5, No. 3, 267-280, 1991.

External calibration of polarimetric radars using point and distributed targets (S. H. Yueh, J. A. Kong, and R. T. Shin), *Proceedings of the Third Airborne Synthetic Aperture Radar (AIRSAR) Workshop*, JPL, Pasadena, CA, May 23-24, 1991

Application of neural networks to sea ice classification using polarimetric sar images (R. Kwok, Y. Hara, R. G. Atkins, S. H. Yueh, R. T. Shin and J. A. Kong), *International Geoscience and Remote Sensing Symposium (IGARSS'91)*, Helsinki University of Technology, Espoo, Finland, June 3-6, 1991.

Electromagnetic scattering of waves by random rough surface: a finite-difference time-domain approach (C. H. Chan, S. H. Lou, L. Tsang, and J. A. Kong), *Microwave and Optical Technology Letters*, Vol. 4, No. 9, 355 - 359, August 1991.

Application of random medium model to remote sensing of vegetation (T. Le Toan, S. V. Nghiem, J. A. Kong, H. C. Han,) *International Geoscience and Remote Sensing Symposium (IGARSS'91)*, Helsinki University of Technology, Espoo, Finland, June 3-6, 1991.

Multiple ellipsoidal species in layer random medium model (S. V. Nghiem, J. A. Kong, R. T. Shin, T. Le Toan), *Progress in Electromagnetics Research Symposium*, Cambridge, Massachusetts, July 1 - 5, 1991.

Polarimetric passive remote sensing of an azimuthally asymmetric periodic soil surface (S. V. Nghiem, M. E. Veysoglu, J. A. Kong, R. T. Shin, K. O'Neill, A. W. Lohanick), *Progress in Electromagnetics Research Symposium*, Cambridge, Massachusetts, July 1 - 5, 1991.

Radiative transfer theory for passive microwave remote sensing of a vegetation canopy (H. C. Han, W. Au, S. H. Yueh, R. T. Shin, J. A. Kong), *Progress in Electromagnetics Research Symposium*, Cambridge, Massachusetts, July 1 - 5, 1991.

Analytical solution of the vector radiative transfer equation with rough surface boundary condition (H. C. Han, J. A. Kong, S. V. Nghiem, T. Le Toan), *Progress in Electromagnetics Research Symposium*, Cambridge, Massachusetts, July 1 - 5, 1991.

Branching model for polarimetric remote sensing of vegetation (S. H. Yueh, J. A. Kong, J. K. Jao, S. Ayasli, R. T. Shin), *Progress in Electromagnetics Research Symposium*, Cambridge, Massachusetts, July 1 - 5, 1991.

Radiative transfer modeling of vegetation clusters (C. C. Hsu, S. H. Yueh, H. C. Han, R. T. Shin, J. A. Kong), *Progress in Electromagnetics Research Symposium*, Cambridge, Massachusetts, July 1 - 5, 1991.

Polarimetric passive remote sensing of periodic structures (M. E. Veysoglu, S. H. Yueh, R. T. Shin, J. A. Kong), *Progress in Electromagnetics Research Symposium*, Cambridge, Massachusetts, July 1 - 5, 1991.

A radar scattering model for structured vegetation (S. H. Yueh, J. A. Kong, J. K. Jao, R. T. Shin, T. Le Toan), *Progress in Electromagnetics Research Symposium*, Cambridge, Massachusetts, July 1 - 5, 1991.

Application of neural networks to polarimetric sar image classification (Y. Hara, R. G. Atkins, S. H. Yueh, R. T. Shin, J. A. Kong, R. Kwok), *Progress in Electromagnetics Research Symposium*, Cambridge, Massachusetts, July 1 - 5, 1991.

Covariance of phase and amplitude fluctuations of electromagnetic waves propagating through a random medium (J. G. Fleischman, S. Ayasli, R. T. Shin, N. C. Chu, S. H. Yueh, S. V. Nghiem), *Progress in Electromagnetics Research Symposium*, Cambridge, Massachusetts, July 1 - 5, 1991.

Observation and modelling of polarimetric sar signatures of forests (T. Le Toan, A. Beaudoin, S. Goze, S. V. Nghiem, J. A. Kong), *Progress in Electromagnetics Research Symposium*, Cambridge, Massachusetts, July 1 - 5, 1991.

Electromagnetic wave modeling for remote sensing (S. V. Nghiem, J. A. Kong, and T. Le Toan), *International Conference on Directions in Electromagnetic Wave Modeling*, New York, October 22-24, 1990.

Simulation of electromagnetic phenomena using a finite difference-time domain technique (K. Li, M. A. Tassoudji, R. T. Shin, and J. A. Kong), *7th Annual Review of Progress in Applied Computational Electromagnetics*, Naval Postgraduate School, Monterey, pp. 38-55, March 18-22, 1991.

Layer model with random spheroidal scatterers for remote sensing of vegetation canopy (S. V. Nghiem, J. A. Kong, H. C. Han, T. Le Toan, and M. Borgeaud), to be submitted to *Journal of Electromagnetic Waves and Applications*.

Finite difference method for electromagnetic scattering problems (C. F. Lee, R. T. Shin, and J. A. Kong), *Progress In Electromagnetics Research*, edited by J. A. Kong, Vol. 4, Chapter 11, p. 373-442, Elsevier, New York, 1990.

Calibration of polarimetric radars using in-scene reflectors, (S. H. Yueh, J. A. Kong, and R. T. Shin), *Progress In Electromagnetic Research*, edited by J. A. Kong, Chapter 9, Vol. 3, p. 451-510, Elsevier, New York, 1990.

Classification and maximum contrast of earth terrain using polarimetric synthetic aperture radar images, (J. A. Kong, S. H. Yueh, H. H. Lim, R. T. Shin, and J. J. van Zyl), *Progress In Electromagnetic Research*, edited by J. A. Kong, Chapter 6, Vol. 3, p. 327-370, Elsevier, New York, 1990.

K-distribution and polarimetric terrain radar clutter, (S. H. Yueh, J. A. Kong, J. K. Jao, R. T. Shin, H. A. Zebker, T. Le Toan, and H. Öttl), *Progress In Electromagnetic Research*, edited by J. A. Kong, Chapter 4, Vol. 3, p. 237-275, Elsevier, New York, 1990.

Polarimetric remote sensing of geophysical media with layer random medium model (S. V. Nghiem, M. Borgeaud, J. A. Kong, and R. T. Shin), *Progress In Electromagnetic Research*, edited by J. A. Kong, Chapter 1, Vol. 3, p. 1-73, Elsevier, New York, 1990.

Classification of earth terrain using synthetic aperture radar images (H. Lim, A. A. Swartz, H. A. Yueh, J. A. Kong, R. T. Shin, and J. J. Van Zyl), *Journal of Geophysical Research*, Vol. 94, No. B6, 7049-7057, June 10, 1989.

K-distribution and polarimetric terrain radar clutter (H. A. Yueh, J. A. Kong, J. K. Jao, R. T. Shin, and L. M. Novak), *Journal of Electromagnetic Waves and Applications*, Vol. 3, No. 8, 747-768, 1989.

Calibration of polarimetric radar using in-scene reflectors (H. A. Yueh, J. A. Kong, R. M. Barnes, and R. T. Shin), *Journal of Electromagnetic Waves and Applications*, Vol. 4, No. 1, 27-49, 1990.

A neural net method for high range resolution target classification (R. G. Atkins, R. T. Shin, and J. A. Kong), *Progress In Electromagnetics Research*, edited by J. A. Kong, Chapter 7, Vol. 4, p. 255-292, Elsevier, New York, 1990.

Scattering from randomly oriented scatterers with strong permittivity fluctuations, (H. A. Yueh, R. T. Shin, and J. A. Kong), *Journal of Electromagnetic Waves and Applications*, Vol. 4, No. 10, p. 983-1004, 1990.

Polarimetric remote sensing of earth terrain with two-layer random medium model, (M. Borgeaud, J.A. Kong, R.T. Shin, and S. V. Nghiem), *Progress in Electromagnetics Research Symposium*, Boston, July 25-26, 1989.

Three-layer random medium model for fully polarimetric remote sensing of geophysical media (S. V. Nghiem, F. C. Lin, J. A. Kong, R. T. Shin, and H. A. Yueh), *Progress in Electromagnetics Research Symposium*, Boston, July 25-26, 1989.

Faraday polarization fluctuations in transionspheric polarimetric VLF waves (S. V. Nghiem and J. A. Kong), *Progress in Electromagnetics Research Symposium*, Boston, July 25-26, 1989.

Calibration of polarimetric radars using in-scene reflectors (H. A. Yueh, J. A. Kong, R. M. Barnes and R. T. Shin), *Progress in Electromagnetics Research Symposium*, Boston, July 25-26, 1989.

K-distribution and polarimetric terrain radar clutter (H. A. Yueh, J. A. Kong, J. K. Jao, R. T. Shin, and L. M. Novak), *Progress in Electromagnetics Research Symposium*, Boston, July 25-26, 1989.

Theoretical models for polarimetric microwave remote sensing of earth terrain (M. Borgeaud, S. V. Nghiem, R. T. Shin, and J. A. Kong), *Journal of Electromagnetic Waves and Application*, Vol. 3, No. 1, 61-81, 1989.

The optimal polarizations for achieving maximum contrast in radar polarimetry (A. A. Swartz, H. A. Yueh, J. A. Kong, L. M. Novak, and R. T. Shin), *Journal of Geophysical Research*, Vol. 93, No. B12, 15252-15260, Dec. 1988.

Theoretical models for polarimetric microwave remote sensing of earth terrain (M. Borgeaud, J. A. Kong, R. T. Shin, and S. V. Nghiem) *Proceedings of the 1988 NATO Advanced Research Workshop*, Nuremberg, F. R. Germany, September, 1988.

Polarimetric clutter modeling: theory and application (J. A. Kong, F. C. Lin, M. Borgeaud, H. A. Yueh, A. A. Swartz, H. H. Lim, L. M. Novak, and R. T. Shin), *GACIAC PR-88-03, The Polarimetric Technology Workshop*, Rocket Auditorium, Redstone Arsenal, U. S. Army Missile Command, Huntsville, Alabama, August 16-19, 1988.

Polarimetric remote sensing of earth terrain with three-layer random medium model (S. V. Nghiem, F. C. Lin, J. A. Kong, R. T. Shin, and H. A. Yueh), *GACIAC PR-88-03, The Polarimetric Technology Workshop*, Rocket Auditorium, Redstone Arsenal, U. S. Army Missile Command, Huntsville, AL, Aug. 16-19, 1988.

Radar range profile simulation of terrain clutter using the random medium model (A. A. Swartz, L. M. Novak, R. T. Shin, D. A. McPherson, A. V. Saylor, F. C. Lin, H. A. Yueh, J. A. Kong) *GACIAC PR-88-03, The Polarimetric Technology Workshop*, Rocket Auditorium, Redstone Arsenal, U. S. Army Missile Command, Huntsville, AL, Aug. 16-19, 1988.

Three-layer random medium model for polarimetric remote sensing of earth terrain (H. A. Yueh, S. V. Nghiem, F. C. Lin, J. A. Kong, and R. T. Shin), *IEEE AP-S International Symposium and URSI Radio Science Meeting*, Syracuse, June 6 - 10, 1988.

The optimal polarizations for achieving maximum contrast in radar polarimetry (A. A. Swartz, L. M. Novak, R. T. Shin, H. A. Yueh, and J. A. Kong), *IEEE AP-S International Symposium and URSI Radio Science Meeting*, Syracuse, June 6 - 10, 1988.

K-distribution and polarimetric terrain radar clutter (H. A. Yueh, J. A. Kong, J. K. Jao, and R. T. Shin), *IEEE AP-S International Symposium and URSI Radio Science Meeting*, Syracuse, June 6 - 10, 1988.

Classification of earth terrain using polarimetric synthetic aperture radar imagery (H. H. Lim, A. A. Swartz, H. A. Yueh, J. A. Kong and J. J. van Zyl), *IEEE AP-S International Symposium and URSI Radio Science Meeting*, Syracuse, June 6 - 10, 1988.

Theoretical model for snow-covered sea ice (F. C. Lin, J. A. Kong, R. T. Shin, A. J. Gow, and D. Perovich), *IEEE AP-S International Symposium and URSI Radio Science Meeting*, Syracuse, June 6 - 10, 1988.

Effect of multiple scattering on the radar cross section of polygonal plate structures (R. G. Atkins and R. T. Shin), *IEEE AP-S International Symposium and URSI Radio Science Meeting*, Syracuse, June 6 - 10, 1988.

Bayes classification of terrain cover using normalized polarimetric data (H. A. Yueh, A. A. Swartz, J. A. Kong, R. T. Shin, and L. M. Novak), *Journal of Geophysical Research*, Vol. 93, No. B12, 15261-15267, December 1988.

Scattering of electromagnetic waves from a periodic surface with random roughness (H. A. Yueh, R. T. Shin, and J. A. Kong), *Journal of Applied Physics*, vol.64, no.4, 1657-1670, August 1988.

Scattering of electromagnetic waves from a periodic surface with random roughness (H. A. Yueh, R. T. Shin, and J. A. Kong), *SPIE Proceedings*, vol. 927, Florida, April 6 - 8, 1988.

Polarimetric microwave remote sensing of anisotropic earth terrain with strong fluctuation theory (M. Borgeaud, J. A. Kong, and R. T. Shin), *IGARSS 87 and URSI Meeting*, University of Michigan, Ann Arbor, MI, May 18-21, 1987.

Theoretical models for active and passive microwave remote sensing of snow-covered sea ice (F. C. Lin, J. A. Kong, and R. T. Shin), *IGARSS 87 and URSI Meeting*, University of Michigan, Ann Arbor, MI, May 18-21, 1987.

Theoretical models for polarimetric radar clutter (M. Borgeaud, R. T. Shin, and J. A. Kong), *Journal of Electromagnetic Waves and Applications*, vol. 1, no. 1, pp. 73-89, 1987.

Applications of EMSARS Background Model to  
MMW Vegetation Scattering Simulation

C. C. ESN, Y. E. Yang, R. T. Shin, J. A. Keng  
Massachusetts Institute of Technology  
Cambridge, Massachusetts 02139

C. Kohler, T. Nguyen, H. Nguyen, J. Ho  
US Army CECOM Night Vision and Electro-Optics Directorate (NVEOD)  
Ft. Belvoir, Virginia 22060

Abstract

EMSARS (Electromagnetic Model of Scattering Applied to Remote Sensing) is an electromagnetic background scattering model developed at the Massachusetts Institute of Technology. The physical characterization of the terrain background is in terms of layered continuous random medium and discrete scatterer models. Various theories and mathematical techniques such as the analytical Wave Theory with the Born Approximation and the Radiative Transfer Theory are used to solve the integral equations characterizing the electromagnetic scattering effects.

In this paper, applications of the EMSARS model to millimeter wave scattering by vegetation will be presented. Tree is modeled as discrete scatterers with multiple sizes for the trunk, the branches and leaves, respectively. Currently, the leaves of coniferous trees, the branches, and the trunks are modeled as circular cylinders. For deciduous trees, the leaves are modeled as thin circular disks. The physical optics approximation is used to calculate the millimeter wave returns from circular disks while finite cylinder approximation is used for circular cylinders. Then, the branching structure and their orientation distributions are applied to obtain the radar returns from vegetation. The trunk is model as a circular cylinder with random surface roughness where geometrical optics approximation is used to calculate the radar return from the surface of trunk. Except for the case in which the ground is illuminated, we only consider single scattering returns. Transmission loss factors, due to absorption and scattering, are included when computing the contribution from interior branches and leaves. Theoretical predictions will be compared with the measurement data recently collected in Bend, Oregon by NVEOD using a 94GHz radar.

I. Introduction

Electromagnetic scattering from earth terrains is a very sophisticated physical phenomenon. During the past two decades, researchers at the Massachusetts Institute of Technology have been engaged in the development and study of various theoretical models for the microwave remote sensing of earth terrain. The collection of research efforts on these models and associated computer programs is called EMSARS (Electromagnetic Modeling of Scattering Applied to Remote Sensing). As summarized in the monograph *"Theory of Microwave Remote Sensing"* [1], electromagnetics models have been developed to account for the effects of absorption, layering, volume scattering and rough interfaces, and have been applied in the interpretation of active and passive remote sensing data collected from various types of earth terrain, such as forests, vegetation canopies, road surfaces, lava, snow-ice fields, under environmental and seasonal changes.

In dealing with radar returns from background media, we have to consider the effects of both surface and volume scattering. The surface scattering effect can be dealt with by the random rough surface model in EMSARS. This model provides a simple approach to account for returns from highly reflective surfaces such as road, sand-covered terrain, and lake. We have implemented composite rough surface model, which includes the Kirchhoff Approximation (KA) and the Small Perturbational Method (SPM) algorithms for computing scattering from large- and small- scale surface roughnesses. In addition, we have developed the extended boundary condition (EBC) and integral equation techniques for dealing with the randomly perturbed periodic rough surface model, which accounts for row structures in plowed fields.



The volume scattering effect is important for returns from bare soils, vegetation, forest, snow-ice fields, in which the underlying scatterers play important roles. The volume scattering effect is also useful in explaining diurnal changes. A layered random medium model has been developed. Each layer of the medium is described using both deterministic and statistical parameters. For example, layer thickness can be used to model vegetation heights, snow depth, etc., and correlation length and variance are closely related to the shape and density of leaves and water contents. It has been shown that a two-layer random medium model works very well in the interpretation of data collected from snow covered terrain, and vegetation fields such as corn, alfalfa, milo, and soybeans. Three-layer random medium model has also been developed and can be used to model more sophisticated background.

In the three-dimensional mm wave radar simulation, it is sometimes necessary to consider isolated trees and shrubs as part of the background. In this case, we may have to add some other parameters, such as the size of the canopy, when using the layered random medium model. Alternatively, a discrete random scatterer model can be applied. This model provides means of summing the contributions from individual scatterers, including multiple scattering effects, thus allows us to work on a tree-by-tree basis. Basically, the tree trunk can be treated as a deterministic scatterer much like targets, whereas for branches and leaves we shall apply the random scatterer model to calculate returns.

One popular way of solving the scattering problem is through wave theory technique by expanding the solution to the wave integral equation in the form of Born series. The first order term in the Born series represents the single scattering effects and the higher order terms contribute to multiple scattering effects in the radar returns. The Born series technique produces solution in analytical form, but the expression becomes very complicated if multiple scattering effects are to be considered. In contrast, the radiative transfer (RT) theory has been commonly used owing to its simplicity and ease of handling multiple scattering to some extent. The radiative transfer theory consists of the radiative transfer equations, which govern the electromagnetic energy propagation through scattering media. Various models have been developed based on this theory [2-4]. The conventional RT theory ignores the relative phase information associated with structured scatterers, which may play an important role in the overall scattering behavior [5] because vegetation generally consists of structures of many different scale lengths. For example, the trunk, primary branches, secondary branches, and leaves, give rise to different scattering effects at any given wavelength. Vegetation elements of each scale are connected to elements of other scales in a fashion statistically described by the unique architecture pertaining to each tree species group. For the microwave remote sensing of forest, the vegetation structures not only cause the separation of scattering centers, but also provide partially coherent scattering by different scatterers with statistically prescribed relative positions.

In this paper, a RT model is constructed for the modeling of the vegetation. The model makes use of the branching model for vegetation [5] to account for the scattering properties of trees. Section II summarizes the basics of radiative transfer theory. In Section III, the phase matrix based on branching model is formulated. In Section IV, formula for the calculation of range profile of trees is given. Section V presents the comparison of model with experimental data collected by NVEOD using a 94 GHz radar.

## II. Radiative Transfer Theory

The canopy of a tree can be modeled as a random medium of certain shape, e.g. a cone. The random medium is composed of discrete scatterers embedded in homogeneous background, as shown in Figure 1.

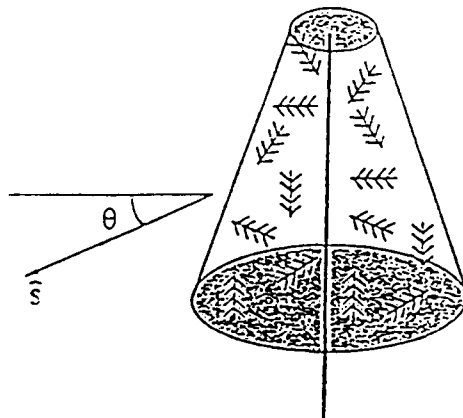


Fig. 1 Tree model.

The vector radiative transfer equation for the specific intensity in the scattering region is of the form

$$\frac{d\bar{I}(\theta, \phi, s)}{ds} = -\bar{\kappa}_e(\theta, \phi) \cdot \bar{I}(\theta, \phi, s) + \int_{4\pi} d\Omega' \bar{P}(\theta, \phi; \theta', \phi') \cdot \bar{I}(\theta', \phi', s) \quad (1)$$

where the Stokes vector  $\bar{I}$  contains information regarding field intensity and phase relation of the two orthogonal polarizations is defined as

$$\bar{I} = \begin{pmatrix} I_h \\ I_v \\ U \\ V \end{pmatrix} = \frac{1}{\eta} \begin{pmatrix} \langle |E_h|^2 \rangle \\ \langle |E_v|^2 \rangle \\ 2 \operatorname{Re}(E_v E_h^*) \\ 2 \operatorname{Im}(E_v E_h^*) \end{pmatrix} \quad (2)$$

In (2), the subscripts  $h$  and  $v$  represent the horizontal and vertical polarizations, respectively. The angular bracket  $\langle \rangle$  denotes ensemble average over the size and orientation distributions of scatterers; and  $\eta = \sqrt{\mu_0/\epsilon_0}$  is the free-space characteristic impedance.

The extinction matrix  $\bar{\kappa}_e$  represents the attenuation due to both the scattering and absorption, and can be obtained through the optical theorem with forward scattering functions.

$$\bar{\kappa}_e(\theta, \phi) = \frac{2\pi n_0}{k} \begin{pmatrix} 2\operatorname{Im}(f_{hh}) & 0 & \operatorname{Im}(f_{hv}) & \operatorname{Re}(f_{hv}) \\ 0 & 2\operatorname{Im}(f_{vv}) & \operatorname{Im}(f_{vh}) & -\operatorname{Re}(f_{vh}) \\ 2\operatorname{Im}(f_{vh}) & 2\operatorname{Im}(f_{hv}) & \operatorname{Im}(f_{vv}+f_{hh}) & \operatorname{Re}(f_{vv}-f_{hh}) \\ -2\operatorname{Re}(f_{vh}) & 2\operatorname{Re}(f_{hv}) & \operatorname{Re}(f_{vv}-f_{hh}) & \operatorname{Im}(f_{vv}+f_{hh}) \end{pmatrix} \quad (3)$$

The phase matrix  $\bar{P}(\theta, \phi; \theta', \phi')$  characterizes the scattering of the Stokes vector from  $(\theta', \phi')$  direction into  $(\theta, \phi)$  direction. It can be formulated in terms of scattering functions of the randomly distributed discrete scatterers.

$$\bar{P}(\theta, \phi; \theta', \phi') = n_0 \begin{pmatrix} \langle |f_{hh}|^2 \rangle & \langle |f_{hv}|^2 \rangle & \operatorname{Re}(f_{hv} f_{hh}^*) & -\operatorname{Im}(f_{hv} f_{hh}^*) \\ \langle |f_{vh}|^2 \rangle & \langle |f_{vv}|^2 \rangle & \operatorname{Re}(f_{vv} f_{vh}^*) & -\operatorname{Im}(f_{vv} f_{vh}^*) \\ 2\operatorname{Re}(f_{vh} f_{hh}^*) & 2\operatorname{Re}(f_{vv} f_{hv}^*) & \operatorname{Re}(f_{vv} f_{hh}^* + f_{vh} f_{hv}^*) & -\operatorname{Im}(f_{vv} f_{hh}^* - f_{vh} f_{hv}^*) \\ 2\operatorname{Im}(f_{vh} f_{hh}^*) & 2\operatorname{Im}(f_{vv} f_{hv}^*) & \operatorname{Im}(f_{vv} f_{hh}^* + f_{vh} f_{hv}^*) & \operatorname{Re}(f_{vv} f_{hh}^* - f_{vh} f_{hv}^*) \end{pmatrix} \quad (4)$$

where  $n_0$  is number density of scatterers,  $k$  is the free space wave number,  $f_{ab}$  is the element of scattering matrix with incident field having polarization  $b$ , and scattered field has polarization  $a$ .  $a, b$  can be horizontal or vertical polarization.

The scattering matrix which relates the incident electric field to the scattered electric field is defined as

$$\begin{pmatrix} E_{hs} \\ E_{vs} \end{pmatrix} = \frac{e^{ikr}}{r} \begin{pmatrix} f_{hh} & f_{hv} \\ f_{vh} & f_{vv} \end{pmatrix} \cdot \begin{pmatrix} E_{hi} \\ E_{vi} \end{pmatrix} \quad (5)$$

where  $e^{ikr}/r$  is the spherical wave transformation.

Along with the boundary conditions that require the Stokes vector to be continuous, we can solve the radiative transfer equations iteratively for the backscattering radar cross-section [1].

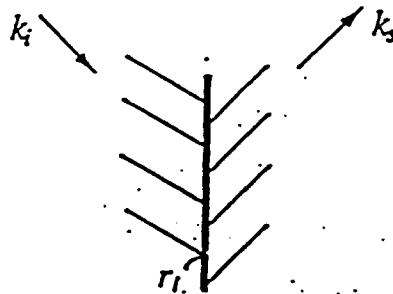


Fig. 2 Cylinder cluster.

### III. Scattering Function for Clustered Structure

To take into account the partially coherent effect due to clustered vegetation structures, we formulate the phase matrix based on the branching model for vegetation. Take a cylinder cluster for example. For a cluster that has one center cylinder and  $N$  branching cylinders as shown in Figure 2, the total backscattering function  $f_{\alpha\beta}$  is

$$f_{\alpha\beta} = f_{0\alpha\beta} + \sum_{n=1}^N f_{n\alpha\beta} e^{i\phi_n} \quad (6)$$

where  $f_{0\alpha\beta}$  is the  $\alpha\beta$ -th element of the scattering matrix for the center cylinder, and  $f_{n\alpha\beta}$  is  $\alpha\beta$ -th element of the scattering matrix for the  $n$ -th branching cylinder.  $\alpha, \beta, \gamma, \delta$  represent horizontal or vertical polarization.

Assuming all the branching cylinders are identical and independent of each other, and their relative position is independent of their scattering properties such as size and orientation, the correlation of  $f$  is

$$\begin{aligned} \langle f_{\alpha\beta} f_{\gamma\delta}^* \rangle &= \langle f_{0\alpha\beta} f_{0\gamma\delta}^* \rangle + N \langle f_{n\alpha\beta} f_{n\gamma\delta}^* \rangle \\ &\quad + 2N \operatorname{Re} [\langle f_{0\alpha\beta} \rangle \langle f_{n\gamma\delta}^* \rangle \langle e^{-i\phi_n} \rangle] \\ &\quad + N(N-1) \langle f_{m\alpha\beta} \rangle \langle f_{n\gamma\delta}^* \rangle \langle e^{i\phi_m} \rangle \langle e^{-i\phi_n} \rangle \end{aligned} \quad (7)$$

The relative phase of the  $n$ -th branch with respect to the center cylinder is defined as

$$\phi_n = (\bar{k}_i - \bar{k}_s) \cdot \bar{r}_n$$

where  $\bar{k}_i$  and  $\bar{k}_s$  are the incident and scattered wave vectors, respectively.  $\bar{r}_n$  is the location of the  $n$ -th branching cylinder relative to the center cylinder.

In (6), the third and fourth terms are the coherent terms. It can be seen that the incoherent approximation is valid when the average of the random phase factor  $\langle e^{i\phi_j} \rangle$  is so small that the coherent terms are negligible as compared with the incoherent terms. However, this is not true for vegetation structures with scale lengths comparable to the wavelength, as was demonstrated with a two-scale cluster[5].

For the calculation of scattered fields of different cluster elements, dielectric cylinders can be used to model trunks, branches, and coniferous leaves [6,7]. Leaves of deciduous tree can be modelled as disks [6,8]. The physical optics approximation is used for the calculation of scattering from disks. The truncated infinite cylinder approximation [9] is employed in this study to calculate scattered fields from cylinders.

### IV. Calculation of Range Profile

In cases when the elevation angle is small, ignoring the ground effect, the first-order iterative solution of the RT equation, which specifies the scattering Stokes vector  $\bar{I}_s$  in terms of incident Stokes vector  $\bar{I}_0$  is as follows:

$$\begin{aligned} \bar{I}_s(\theta, \phi, s = l_2) &= \int_{l_1}^{l_2} ds' \bar{D}(\beta(\theta, \phi)(l_2 - s')) \bar{D}(\beta(\pi - \theta_0, \phi_0)(l_2 - s')) \bar{P}(\theta, \phi, \pi - \theta_0, \phi_0) \cdot \bar{I}_0(\pi - \theta_0, \phi_0, s = l_2) \\ &= \bar{M} \cdot \bar{I}_0(\pi - \theta_0, \phi_0, s = l_2) \end{aligned} \quad (8)$$

where  $\bar{D}(\beta(\theta, \phi)s')$  is the  $4 \times 4$  diagonal matrix with  $e^{(\beta_i(\theta, \phi)s')}$  as its  $ii$ -th elements. Here  $\beta_i$  is the  $i$ -th eigenvalue of  $\bar{\kappa}_e$ .  $s'$  is in the direction of the propagation and  $l_1, l_2$  are the boundaries of the random medium.

Equation (8) represents the single scattering by the discrete scatterers inside the random medium.  $\bar{D}$  is the attenuation factor and  $\bar{P}$  can be considered as the scattering intensity.  $\bar{M}$  is Mueller matrix.  $M_{11}$  and  $M_{22}$  are the radar cross-sections per unit area for  $H$ - and  $V$ - polarizations, respectively.

If the random medium is azimuthally symmetrical around the propagation direction, the backscattering radar cross section per unit area for the co-polarized returns can be further simplified as

$$\begin{aligned}
M_{11} &= \int_{l_1}^{l_2} ds' n_0 \langle |f_{hh}|^2 \rangle \cdot e^{-2\kappa_a(l_2-s')} \\
M_{22} &= \int_{l_1}^{l_2} ds' n_0 \langle |f_{vv}|^2 \rangle \cdot e^{-2\kappa_a(l_2-s')}
\end{aligned}
\tag{9}$$

where  $\kappa_a = \frac{2\pi n_a}{k} \cdot 2Im \langle f_{aa} \rangle$  is the attenuation constant for polarization  $a$ .  $a$  could be  $h$  or  $v$ .

Therefore the radar cross-section per unit length in the propagation direction for polarization  $a$  can be expressed as

$$\sigma_{aa} = 4\pi \int_{l-\delta_l}^{l+\delta_l} ds' \int dA' n_0 \langle |f_{aa}|^2 \rangle \cdot e^{-2\kappa_a(l_2-s')/2\delta_l}
\tag{10}$$

In the computation of trunk scattering contributions, surface roughness is an important factor. At 94 GHz the wavelength is much smaller than the radius of trunk and thus the surface roughness, no matter how small, can still be comparable to the wavelength. The radar cross-section is calculated by breaking up the trunk surface into small pieces and summing up the response from individual pieces. The radar cross-section of each small surface is calculated by multiplying the area with the scattering coefficient. Thus the backscattering radar cross-section per unit length is

$$\int dA' \gamma(\theta, \phi, \bar{r}) \cdot e^{-k_a s'}
\tag{11}$$

where  $\gamma$  is the scattering coefficient for the reflected wave from the trunk surface. It is a function of incident angle and the local curvature of trunk.

To calculate the range profile, we need to convolve the radar cross-section per unit length (from Equations 10 and 11) with the radar response of the point target. This impulse response is determined by the bandwidth and the filter function of the radar system.

## V. Comparison with Experimental Data and Sensitivity Study

Theoretical prediction and computer simulation of mm wave radar range profile are based on the experiment conducted by NVEOD in Bend, Oregon with a truck-mounted 94 GHz FM CW radar. A high range resolution of about 1(one) foot is achieved by stepping the radar frequency through the 470MHz bandwidth. With frequency step size of 10MHz and total of 48 steps, the system provides range ambiguity to about 15 meters.

The NVEOD radar was aimed at two isolated coniferous trees, as shown in Figure 3. The elevation angles are around 5 degrees (looking up); therefore, we can safely neglect the ground effect in our calculation. Within the cluster, the contribution to scattered field at 94 GHz mainly comes from the leaves. Thus the branches were omitted from our calculation. The scattered field from trunk has also been computed separately. The small needles of the tree leaves inside the canopy are modeled as randomly oriented dielectric cylinders.

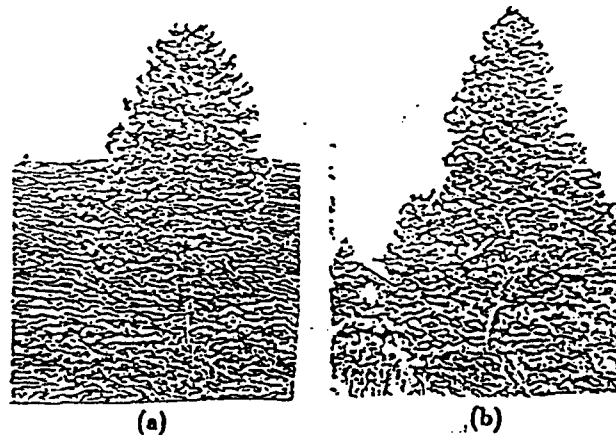


Figure 3 (a) is tree number 1 and (b) is tree number 2, the stick on the ground is 4 feet long.

The canopy of both trees is considered as a random medium of cone shape. The radius and length of the dielectric cylinders, of which the random medium is composed, are assumed to be 0.1cm and 2cm, respectively. The number density of leaves is  $12000/\text{m}^3$  and dielectric constant is  $7 + i1.5$ . Using the photographs taken at the scene, in which a yardstick is inserted in front of each tree, we can estimate the tree height. The first one is estimated at 9 meters high and crown length of 7 meters (calculated from the the first live branch to the top of tree) The radii of top and bottom circles are 0.75m and 3.0m, respectively. As for the second tree, the height of canopy is estimated at 8 meters and crown length of 6.5 meters. The upper and lower circle radii are 0.2m and 2.7m, respectively.

The comparisons between the predicted and measured range profiles from the crown of both trees are given in Figure 4. The measurement and prediction results are given for the HH polarization. Because we did not have the ground truth information for nearby terrains, the comparison is limited to the extent of the trees.

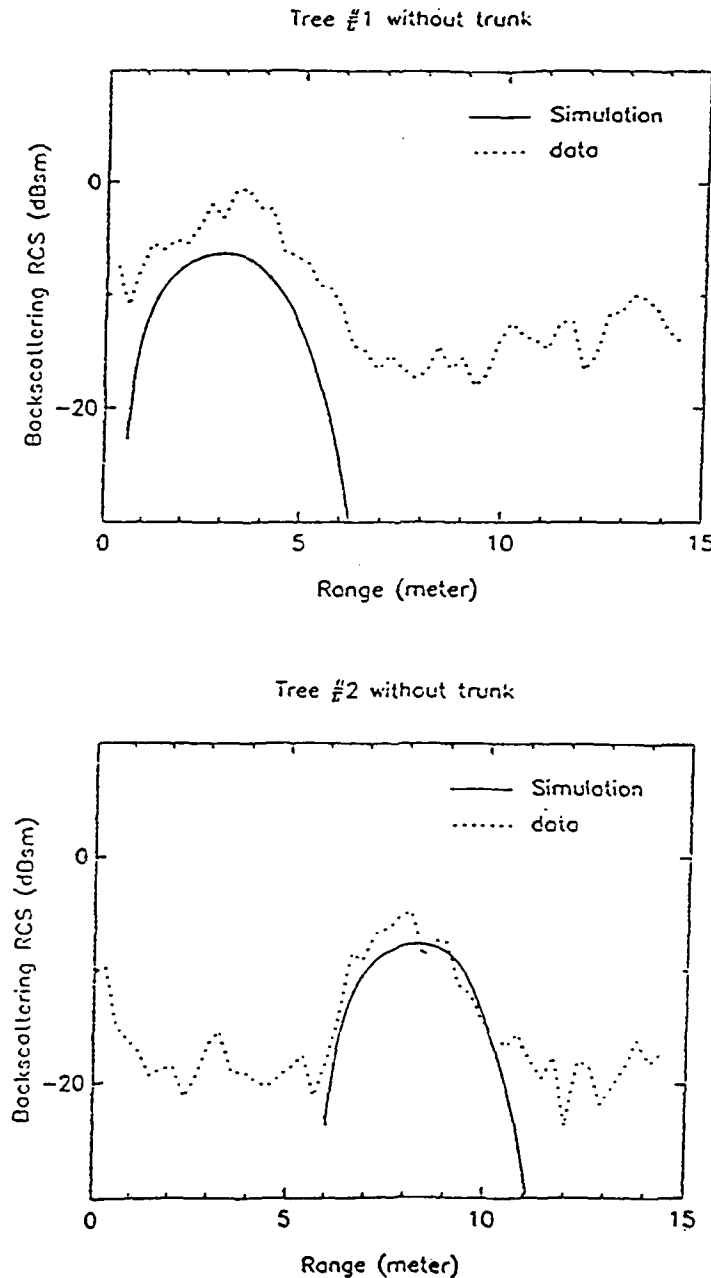


Fig. 4 Comparison of range profile from experimental data and theoretical simulation with crown only.

Solid curve is simulated result, dotted curve is data measured with 1 foot resolution.

The scattering from trunk is calculated with the trunk surface having rms height 0.2cm and correlation length 1cm. The radius of first tree is estimated to be 0.2m and the radius of second tree to be 0.15m. Using the geometrical optics approximation and assuming the slope of surface roughness is Gaussian distributed, the range profile calculated for the whole tree is shown in Figure 5. It is shown that the scattering of trunk will add a small peak on the range profile. The agreement between the theoretical prediction and the experimental data are generally good for the second tree. As for the first tree, the theoretical simulation is about 2 to 3 dB lower than the data. The discrepancy may due to that the multiple scattering effect is ignored in our calculation, or that perhaps the finite cylinder approximation is not accurate enough.

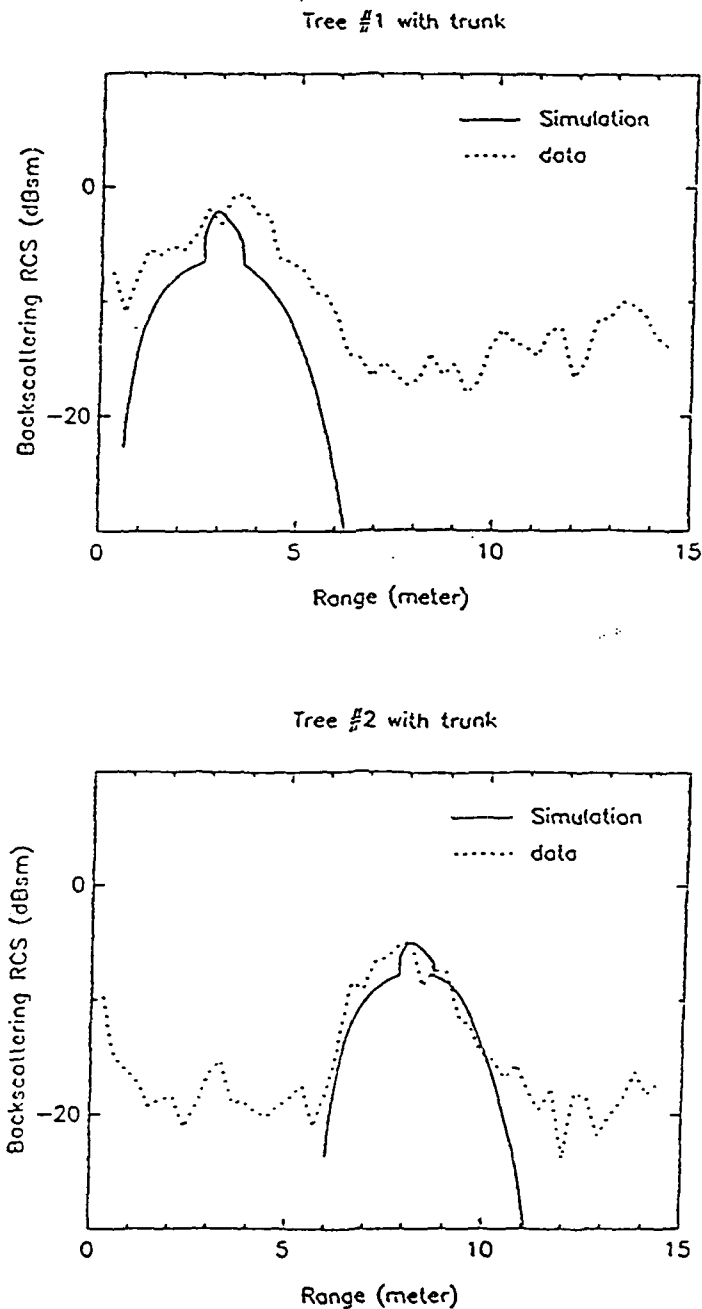


Fig. 5 Comparison of range profile from experimental data and theoretical simulation with both crown and trunk. Solid curve is simulated result, dotted curve is data measured with 1 foot resolution.

As part of this study, we are also interested in the quantitative dependence of the range profile on selective parameters of the tree model. These parameters tend to vary from trees to trees, and hence should provide more insights to the modeling effort. The following is a sensitivity study based on the tree size, number density of leaves and the scattering/attenuation ratio is presented. The variations are limited to the leaves, so the contribution from trunk are not shown in the comparison.

Figure 6(a) shows the range profile of two trees with different sizes. One has radii of top and bottom circles at 0.75m and 3.0m, respectively, and is 9m high. Another has radii of top and bottom circles at 1.125m and 4.5m, respectively, and is 13.5m high. It was shown that the peak radar cross-section of the second tree is about 2 to 3 dB higher and the range of significant radar return is about 50% wider. This matches the increase in the tree size. The simulation on different number density of the leaves is shown in Fig. 6(b). As the number density increases, the radar cross-section from the front part of range profile increase, but it also decrease faster with increasing range at the backside of the tree. This is because as the number density of leaves increase, the scattering and attenuation both increase. The radar return from the front part of tree would increase but the return from the back side of tree would decrease thanks to higher attenuation. A few simplifications in our model may have affected the accuracy. Firstly, the scattering and attenuation from the leaves are calculated from the finite cylinder approximation. Also, the multiple scattering effect is ignored. These two likely impact upon the scattering/attenuation ratio. We performed a simulation in which the scattering coefficient is kept intact but the attenuation coefficient is decreased. As the results shown in fig. 6(c), the front part of the range profile does not change, as was expected since the attenuation does not affect this part significantly. But for the backside of the tree, the lower attenuation, the bigger the radar cross-section and the wider the range with appreciated radar return. Therefore in the model, the correct estimate of attenuation is very important.

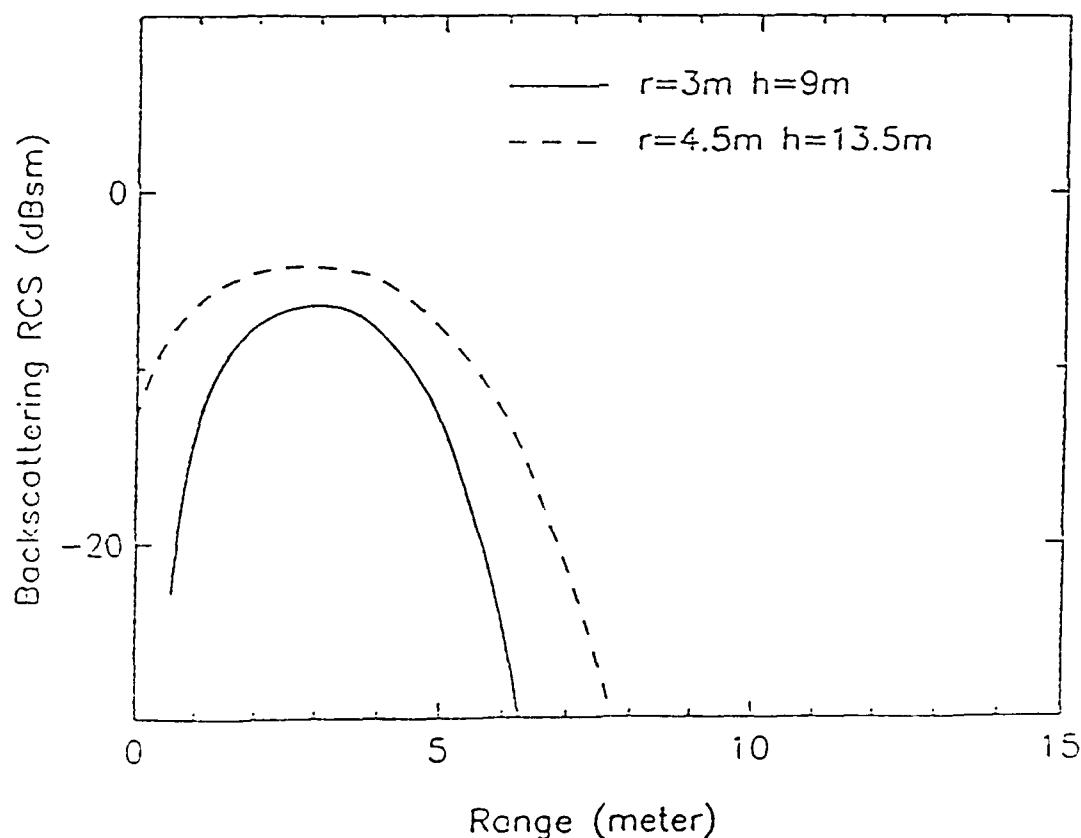


Fig. 6(a) Simulated range profile of trees with different tree size,  $r$  is the bottom circle radius of canopy,  $h$  is tree height.

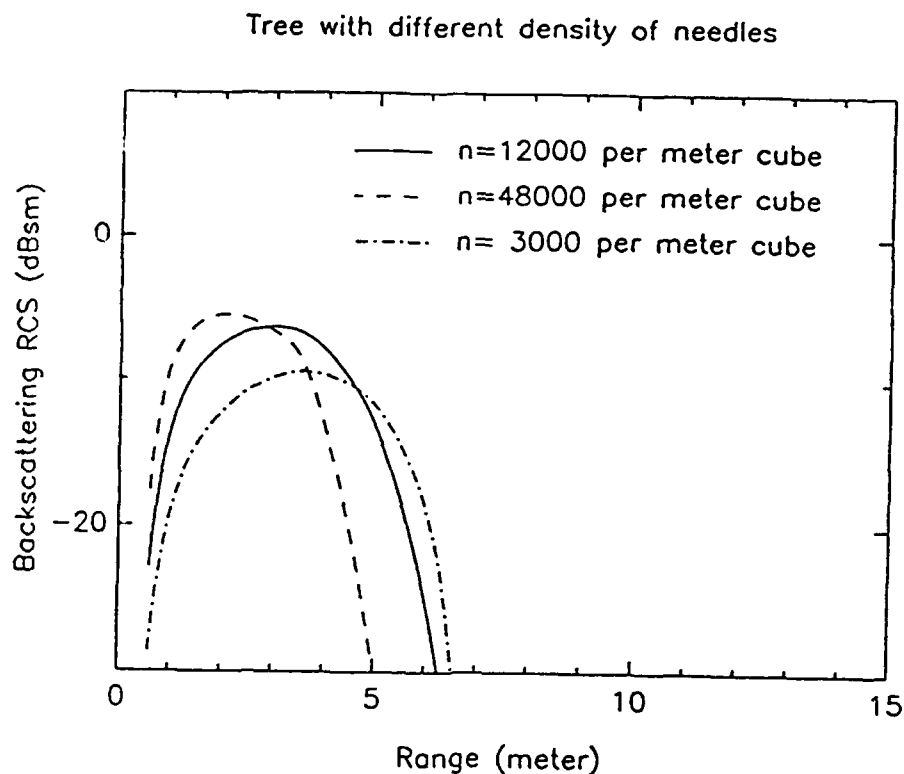


Fig. 6(b) Simulated range profile of trees with different number density of leaves,  $n$  is the number density of leaves per  $m^3$ .

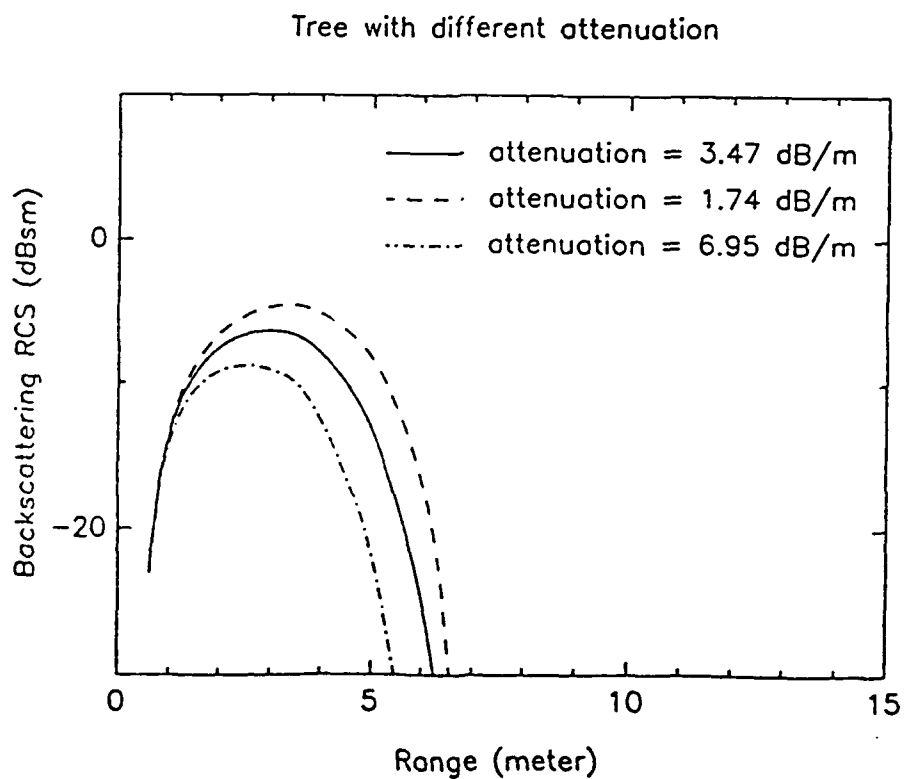


Fig. 6(c) Simulated range profile of trees with different attenuation and fixed scattering amplitude of unit volume.



## VI. Conclusion

In this paper, an electromagnetic scattering model of vegetation based on the radiative transfer theory is presented. The phase matrix is derived with the coherent effects from the clustered structures of leaves. Using this simple model, theoretical prediction has been derived for the range profile simulation and the RCS prediction of single trees. The slight discrepancy with experimental data may be due to the approximation in calculating the attenuation coefficient. A simulation is also presented to examine the sensitivity of different parameters.

## References

- [1] Tsang, L., J. A. Kong, and R. T. Shin, *Theory of Microwave Remote Sensing*, Wiley-Interscience, New York, 1985.
- [2] Tsang, L., J. A. Kong, and R. T. Shin, "Radiative transfer theory for active remote sensing of a layer of nonspherical particles," *Radio Science*, Vol. 19, 629-642, 1984.
- [3] Shin, R. T., and J. A. Kong, "Radiative transfer theory for active remote sensing of two-layer random medium," *Progress in Electromagnetic Research*, Vol. 1, Chapter 4, ed. by J. A. Kong, Elsevier, New York, 1989.
- [4] Han, H. C., S. V. Nghiem, and J. A. Kong, "Analytical solution of vector radiative transfer equation with rough surface boundary condition," *Progress in Electromagnetics Research Symposium*, Cambridge, Massachusetts, 1991.
- [5] Yueh, S. H., J. A. Kong, J. K. Jao, R. T. Shin, and T. Le Toan, "Branching model for vegetation," *IEEE Trans. Geosci. Remote Sensing*, Vol. GE-30, No. 2, 1992.
- [6] Karam, M. A., A. K. Fung, and Y. M. M. Antar, "Electromagnetic wave scattering from some vegetation samples," *IEEE Trans. Geosci. Remote Sensing*, Vol. GE-26, No. 6, 799-808, 1988.
- [7] Durden, S. L., J. J. van Zyl, and H. A. Zebker, "Modeling and observation of the radar polarization signature of forested areas," *IEEE Trans. Geosci. Remote Sensing*, Vol. GE-27, No. 3, 290-301, 1989.
- [8] Lang, R. H., and H. A. Saleh, "Microwave inversion of leaf area and inclination angle distribution from backscattered data," *IEEE Trans. Geosci. Remote Sensing*, Vol. GE-23, No. 5, 685-694, 1985.
- [9] van de Hulst, H. C., *Light Scattering by Small Particles*, Dover, New York, 1981.

## Extenal Calibration of Polarimetric Radars Using Point and Distributed Targets

S. H. Yueh, J. A. Kong, and R. T. Shin

Department of Electrical Engineering and Computer Science  
and Research Laboratory of Electronics  
Massachusetts Institute of Technology  
Cambridge, MA 02139, USA

**Abstract**—Polarimetric radar calibration algorithms using a combination of point targets and reciprocal distributed targets are developed. From distributed target reciprocity, a matrix equation is derived which can be converted into an equivalent point target response, and can also be utilized to make a polarimetric radar reciprocal. The equivalent point target corresponds physically to a 90-degree polarization rotator which is non-reciprocal and rotation-invariant. Due to this equivalent-point-target interpretation, the cases of polarimetric calibration using two point targets and one distributed target then reduce to those using three point targets, which have been solved in previous research. Regarding the calibration using one point target and one reciprocal distributed target, two cases are analyzed with the point target being a sphere (triangular reflector) or a polarimetric active radar calibrator (PARC). For both cases, the general solutions of system distortion matrices are written as a product of a particular solution and a matrix with one free parameter, and then an additional assumption about the distributed target is made to determine the free parameter. For the triangular-reflector case, when the particular solution is applied for calibration, the measured polarimetric data can be calibrated to the level that only rotation errors remain, and once azimuthal symmetry is assumed for the distributed target, an iterative scheme is devised to solve the rotation parameter. For the PARC case, the residual error is like the channel imbalance after the data are calibrated by the particular solution, and the free parameter can be determined by knowing one ratio of two covariance matrix elements of the distributed target. Numerical results were simulated to demonstrate the validity of the algorithms developed in this paper.

## 1. INTRODUCTION

Accurate calibration of polarimetric radar systems is essential for polarimetric remote sensing of earth terrain. The concept and formulation of polarimetric calibration were developed by Barnes [1], who modelled the transmitting and receiving ports of the polarimetric radar as two polarization transferring matrices. In this model the measured polarization scattering matrix corresponding to a target is given by

$$X = eRST \quad (1)$$

where  $S$  is the undistorted polarization scattering matrix of the imaged target. The matrices  $T$  and  $R$  account for the channel imbalance and cross-polarization coupling of the transmitting and receiving ports, respectively. Propagation delay and loss between the radar and the target is accounted for by the complex

scalar parameter  $c$ . The objective of polarimetric calibration is to solve for the  $R$  and  $T$  matrices using responses from targets with known polarization scattering parameters.

For general polarimetric systems, six parameters are to be estimated for polarimetric calibration, three from each of the transmitting and receiving ports. These three parameters include one for channel imbalance and two for cross-talk. To calibrate a general polarimetric system, algorithms using three point targets (in-scene reflectors) have been developed in [1-5], and a calibration algorithm using one distributed target and two point targets is presented in [6, 7].

For specific forms of polarimetric radars, the number of calibration targets can be reduced. For example, by assuming cross-talk factors are identical for a single-antenna system, a three-parameter model was derived and four possible solutions were determined using only the response from a trihedral reflector [8]. Another commonly adopted model is a reciprocal radar ( $R$  being the transpose of  $T$ ). In this case, a calibration technique using responses from natural distributed targets with azimuthal symmetry and trihedral corner reflectors was developed [9]. The method is based on the theoretical results that the co- and cross-polarized components of the scattering matrix are uncorrelated for natural targets with azimuthal symmetry [10].

In this paper, we will investigate algorithms for calibrating a general polarimetric system using a combination of point and distributed targets. Section II will derive an equivalent point target from the response of a reciprocal distributed target. It is then shown that a polarimetric radar can be made reciprocal by using the equivalent point target response. In Section III, calibration using two point targets and one reciprocal distributed target is discussed. Sections IV and V address the use of responses from one point target and one reciprocal distributed target. Two cases are investigated with the point target being a trihedral reflector or a PARC [2]. Numerical simulations are performed in Section VI to demonstrate the usefulness of the algorithms presented.

## II. EQUIVALENT POINT TARGET RESPONSE USING DISTRIBUTED TARGET RECIPROCIITY

In this section, we will derive an equivalent point target from the responses of reciprocal distributed targets, and the model of polarimetric radars defined by (1) will be utilized for formulation.

Let us define a mapping between the scattering matrix  $X$  and a column vector  $\chi$  as follows:

$$X = \begin{bmatrix} X_{11} & X_{12} \\ X_{21} & X_{22} \end{bmatrix} \longleftrightarrow \chi = \begin{bmatrix} X_{11} & X_{12} & X_{21} & X_{22} \end{bmatrix}^t \quad (2)$$

where the superscript  $t$  signifies transpose.

Likewise, we can map the matrix  $S$  into the column vector  $\mathcal{S}$ . Thereafter, Equation (1) can be converted into a matrix equation

$$\chi = AS \quad (3)$$

## External Calibration of Polarimetric Radars

where  $A$  is the direct product of  $R$  and  $T^t$

$$A = R \otimes T^t = \begin{bmatrix} R_{11}T^t & R_{12}T^t \\ R_{21}T^t & R_{22}T^t \end{bmatrix} \quad (4)$$

Note that the parameter  $c$  has been omitted from (3), since only polarimetric calibration is concerned.

For the case that  $S$  is the response from a distributed target,  $S$  is random, and it is more appropriate to describe the distributed target by its covariance matrix,  $C_s$ . From (3), the measured covariance matrices of  $\chi$  and  $C_\chi$  are related to  $C_s$  by

$$C_\chi = AC_sA^+ \quad (5)$$

where '+' signifies conjugate transpose.  $C_\chi$  and  $C_s$  are defined by  $E[\chi\chi^+]$  and  $E[SS^+]$ , respectively. Here,  $E[\cdot]$  represents ensemble average.

## Equations Derived From Distributed Target Reciprocity

Assuming the distributed target is reciprocal ( $S_{12} = S_{21}$ ) and its covariance matrix  $C_s$  has rank 3, Klein and Freeman [6, 7] derived the following equation:

$$Q_\chi = c'A^{+^{-1}}Q_s \quad (6)$$

where  $Q_\chi$  and  $Q_s$  are, respectively, the eigenvectors of  $C_\chi$  and  $C_s$  with zero eigenvalue. Equation (6) was derived based on the fact that  $C_s$  and  $C_\chi$  have rank 3, they can have only one eigenvector with zero eigenvalue, and both eigenvectors can be shown to be related by (6). Note that  $c'$  is an appropriate scaling constant, taking into account the arbitrary absolute magnitudes of eigenvectors. In addition, reciprocity,  $S_{12} = S_{21}$ , means that columns 2 and 3 of  $C_s$  must be equal. Hence,  $Q_s$  can be written explicitly as

$$Q_s = \begin{bmatrix} 0 & -1 & 1 & 0 \end{bmatrix}^t \quad (7)$$

which can be shown to satisfy  $C_sQ_s = 0$ .

Equation (6) is an important observation made by Klein and Freeman [6, 7] using distributed target reciprocity. Subsequently, in their paper they carried out the inversion of  $A^+$  and matrix multiplication in (6) to obtain three nonlinear equations of matrix elements of  $R$  and  $T$  ((19) (21) in [6]). Further supplementing these three equations with the polarimetric responses from two corner reflectors, they solved the normalized matrix elements of  $R$  and  $T$  explicitly.

## A. Equivalent Point Target Response

In this paper, we will recast (6) into another form, which will render an interesting interpretation and allow it for a general application. After recognizing the fact that the mapping from (1) to (3) is one-to-one in nature, we can convert (6) into the following form by an inverse procedure.

$$Q_\chi^{t^{-1}} = \frac{1}{c'} R Q_s^{t^{-1}} T \quad (8)$$

where  $Q_s$  and  $Q_z$  are 2 by 2 matrices corresponding to vectors  $Q_s$  and  $Q_z$ , respectively, through the mapping defined by (2). ' $\bullet$ ' denotes complex conjugate. Hence,

$$Q_s = Q_z'^{-1} = \begin{bmatrix} 0 & -1 \\ 1 & 0 \end{bmatrix} \quad (9)$$

As we now can see, (8) is identical in form to (1). Therefore,  $Q_z'^{-1}$  can be interpreted as the polarimetric response from a point target with scattering matrix  $Q_z'^{-1}$ . Hence, (6) derived from target reciprocity has been converted into an equivalent point target response. It should be noticed that the scattering matrix of the equivalent point target is non-reciprocal.

Furthermore,  $Q_s$  can be physically realized as a 90-degree polarization rotator by observing that an object having a scattering matrix given by (9) will transform a horizontal polarization into a vertical polarization and a vertical polarization into a negative horizontal polarization. Two existing phenomena can produce the effects of polarization rotation. One is the Faraday rotation (non-reciprocal) and the other one is the optical activity produced by chiral media (reciprocal). Both types of media will rotate the polarization of fields as waves propagating through them.

An analysis of using an object defined by (9) as a calibration target has been given by [3], and it is known that this kind of target is rotation-invariant as it can be verified that  $Q_s$  is invariant under any coordinate rotation just like the identity matrix (scattering matrix of a sphere).

$$Q_s = MQ_s M^{-1} \quad (10)$$

where

$$M = \begin{bmatrix} \cos \theta & \sin \theta \\ -\sin \theta & \cos \theta \end{bmatrix} \quad (11)$$

which can be interpreted as a coordinate rotation matrix. Note that  $\theta$  is allowed to be complex.

The fact implied by (10) is consistent with the reciprocity assumed for distributed targets, as we know that reciprocity is preserved no matter how the distributed target is rotated. Hence, the equations derived from reciprocity should contain no information regarding the relative roll angles between the radar and targets.

### B. Reciprocation of Polarimetric Radar

As we know, a polarimetric radar is in general not reciprocal ( $R \neq T^d$ ); therefore the measured scattering matrix  $X$  is not symmetric when  $S$  is symmetric. As will be shown in the following, (8), derived from reciprocity, will be utilized to symmetrize the measured scattering matrix; in other words, it will make the polarimetric radar reciprocal.

From (8), it can be shown that

$$\begin{aligned} T &= c'^* Q_z' R^{-1} Q_z' (Q_z^+ Q_s')^{-1} \\ &= \frac{-c'^*}{\Delta(R)} R' (Q_z^+ Q_s')^{-1} \end{aligned} \quad (12)$$

For convenience, all the proportional constants like  $c'$  will not be written out explicitly from now on. Hence,

$$T = R' (Q_z^+ Q_s')^{-1} \quad (13)$$

Let

$$Y = X Q_z^+ Q_s' \quad (14)$$

Then, by substituting (13) into (1), it is easy to show that

$$Y = R S R^d \quad (15)$$

Note that if  $S$  is symmetric, so is  $Y$ , indicating that we can readily interpret  $Y$  as the response observed by a reciprocal polarimetric radar with  $T$  being the transpose of  $R$ . Hence, a polarimetric radar can be made reciprocal by using the equations derived from reciprocity.

If  $X$  is the backscatter from a reciprocal distributed target, we can derive from  $C_z$  a reciprocated covariance matrix  $C_y$  which is given by

$$C_y = A_y C_z A_y^+ \quad (16)$$

where

$$A_y = I \otimes (Q_s Q_z^+) \quad (17)$$

The results of this section show that the target reciprocity can be utilized to derive an equivalent target response, and through the use of it a polarimetric radar can be made reciprocal. In the following sections, we will further explore the applications of (8) and (15) in solving the full polarimetric calibration problem.

### III. CALIBRATION USING TWO POINT TARGETS AND ONE RECIPROCAL DISTRIBUTED TARGET

For external calibration of polarimetric radars, it is always preferable to reduce the number of calibration targets, not only because a fewer number of targets will reduce the cost and amount of effort necessary for deployment and maintenance, but also due to the fact that many sites to be imaged simply do not provide enough adequate places for target deployment. In this section, we will discuss how to use two general point targets and one reciprocal distributed target for polarimetric calibration. Note that a general class of problems where these two point targets are two reciprocal reflectors have been solved explicitly by Klein and Freeman and verified with the Jet Propulsion Laboratory polarimetric sensors [7].

Cases using more general targets are addressed in this section and the solution can be related to previous research [3]. As shown in the previous section, (6),

which was derived from the measured covariance matrix of reciprocal distributed targets by Klein and Freeman [6, 7] using reciprocity, can be recast into the form of the polarimetric response from a point target. Therefore, the problem of calibration using two point targets and one distributed target reduces to the cases of three point targets. It is known that the problem of polarimetric calibration using three point targets including non-reciprocal targets has been studied and the explicit solutions for various combinations of three targets can be found in [3].

#### IV. ONE TRIHEDRAL REFLECTOR AND ONE RECIPROCAL DISTRIBUTED TARGET

Without loss of generality, two cases will be analyzed. The point target will be considered as a trihedral reflector in this section, and as a PARC in the next section. For each case, an additional assumption about the distributed targets will be made to fully solve the calibration problem.

The problem to be dealt with in this section is how to calibrate a polarimetric radar ( $R \neq T^t$ , in general) using the responses from a trihedral reflector and one distributed target. Note that van Zyl [9] has already provided a scheme for calibrating a reciprocal polarimetric radar ( $T = R^t$ ) using one trihedral reflector and one distributed target with azimuthal symmetry. Note also that in the previous section, we have shown that a general polarimetric radar can be made symmetric by using the reciprocity, indicating that van Zyl's approach can be applied. We will take a different approach, however, in solving the problem so that partial calibration can be carried out without assuming azimuthal symmetry for distributed targets. In addition, if full calibration is required, it will be shown how the additional assumption can be applied for removing the residual error.

Suppose that accompanying the reciprocal distributed target is a trihedral reflector with a scattering matrix  $S_c$ , which is the identity matrix. Therefore, the measured point target response is given by

$$X_c = RT \quad (18)$$

Hence, the symmetrized response is

$$Y_c = X_c Q^t Q_s^t = RR^t \quad (19)$$

and  $T$  can be expressed as

$$T = R^{-1} X_c \quad (20)$$

The general solution of  $R$  can be written as the product of a particular solution  $R_p$  and a rotation matrix  $M$  defined by (11).

$$R = R_p M^{-1} \quad (21)$$

where the particular solution  $R_p$  has the following form:

$$R_p = \begin{bmatrix} R_{p11} & 0 \\ R_{p21} & R_{p22} \end{bmatrix} \quad (22)$$

Note that the total number of independent variables is the same on both sides of (21).

By substituting (21) into (19), it can be shown that

$$Y_c = R_p R_p^t \quad (23)$$

which is the same as (19), indicating that  $R_p$  is a particular solution.

The following normalized quantities can be easily solved from (23)

$$\frac{R_{p21}}{R_{p11}} = \frac{Y_{c12}}{Y_{c11}} = \frac{Y_{c21}}{Y_{c11}} \quad (24a)$$

$$\frac{R_{p22}}{R_{p11}} = \pm \sqrt{\frac{Y_{c22}}{Y_{c11}} - \left( \frac{R_{p21}}{R_{p11}} \right)^2} \quad (24b)$$

From (20), we obtain the particular solution of  $T_p$

$$T_p = R_p^{-1} X_c \quad (25)$$

and the general solution of  $T$  is given by

$$T = MT_p \quad (26)$$

Note that there are two solutions given by (24) and a priori information is needed to eliminate one of them. The reason why we cannot distinguish these two solutions is because the response from the trihedral and reciprocal relations of natural targets are invariant under the following substitution

$$R' = R \begin{bmatrix} 1 & 0 \\ 0 & -1 \end{bmatrix} \quad (27a)$$

$$T' = \begin{bmatrix} 1 & 0 \\ 0 & -1 \end{bmatrix} T \quad (27b)$$

In other words, if the set of matrices  $R$  and  $T$  is a solution, so is the set  $R'$  and  $T'$ .

Up to this point, the general forms of  $R$  and  $T$  have been deduced and are expressed in terms of one general rotation angle,  $\theta$ , which is allowed to be complex. To determine it, one more equation is required. For example, this will require one more point target, as discussed in the previous section about the calibration using two point targets and one distributed target.

In the following, we will assume that the distributed target has an azimuthal symmetry. As shown by theoretical investigations regarding scattering from terrain media [10], azimuthal symmetry implies that the following covariance matrix elements of the distributed target satisfy

$$C_{s12} = C_{s13} = 0 \quad (28a)$$

$$C_{s24} = C_{s34} = 0 \quad (28b)$$

Note that the azimuthal symmetry gives the second equal sign, whereas the reciprocity dictates the first equal sign.

By substituting (21) and (26) into (1), it can be shown that

$$Y_p = R_p^{-1} Y T_p^{-1} = M^{-1} S M \quad (29)$$

Note that  $M^{-1} = M^t$ . Therefore matrix  $X_p$  is symmetric. If we start from (29) as the description of the polarimetric radar, we can follow van Zyl's approach in solving the system parameters using azimuthal symmetry for distributed targets. It should be noticed, however, that there is only one parameter that needs to be determined in the matrix  $M$ , in contrast to two parameters in van Zyl's approach ((10) in [9]). The matrix  $M$  is similar to a rotation operation and is characterized by one parameter,

$$\alpha = \tan \theta \quad (30)$$

Representing  $X_p$  by a vector  $X_p$  according to (2), we can define the covariance matrix  $C_p = E[X_p X_p^+]$ , which is related to  $C_z$  and  $C_s$  by

$$C_p = A_p C_z A_p^+ \quad (31a)$$

$$= A_m C_s A_m^+ \quad (31b)$$

where

$$A_p = R_p^{-1} \otimes T_p^{-1t} \quad (32a)$$

$$A_m = M^{-1} \otimes M^t \quad (32b)$$

By multiplying both sides of (29) by  $M$  and calculating the ensemble average of the products of the matrix elements, we can obtain the following equations:

$$\alpha(C_{p32} + C_{s22}) + \alpha^*(C_{p14} - C_{s11}) = -(C_{p12} + |\alpha|^2 C_{p34}) \quad (33a)$$

$$\alpha(C_{p33} + C_{s23}) + \alpha^*(-C_{p11} + C_{s14}) = -(C_{p13} - |\alpha|^2 C_{p31}) \quad (33b)$$

$$\alpha(-C_{p22} - C_{s32}) + \alpha^*(C_{p44} - C_{s41}) = -(C_{p42} - |\alpha|^2 C_{p24}) \quad (33c)$$

$$\alpha(-C_{p23} - C_{s33}) + \alpha^*(-C_{p41} + C_{s44}) = -(C_{p43} + |\alpha|^2 C_{p21}) \quad (33d)$$

Adding (33a) with (33c) and using the fact that  $C_{p34} = C_{p24}$  implied by  $X_{p12} = X_{p21}$  gives

$$\alpha(C_{p32} + C_{s22} - C_{p22} - C_{s32}) + \alpha^*(C_{p14} - C_{s11} + C_{p44} - C_{s41}) = -(C_{p12} + C_{p42}) \quad (34)$$

Likewise from (33b) and (33d) and using  $C_{p31} = C_{p21}$  we obtain

$$\alpha(C_{p33} + C_{s23} - C_{p23} - C_{s33}) + \alpha^*(-C_{p11} + C_{s14} - C_{p41} + C_{s44}) = -(C_{p13} + C_{p43}) \quad (35)$$

Note that  $\alpha$  can be obtained by utilizing the solution of the following equation

$$a\alpha + b\alpha^* = c \quad (36)$$

which has the solution

$$\alpha = \frac{ca^* - c^*b}{|a|^2 - |b|^2}, \quad \text{provided } |a| \neq |b| \quad (37)$$

The criterion  $|a| \neq |b|$  can be satisfied for a large class of distributed targets as observed from (34) and (35).

If we start with a polarimetric radar having relatively good channel isolation (small  $\alpha$ ), we can use the following iterative scheme to determine the value of  $\alpha$ :

Step 1. Initialize  $\alpha$  as zero.

Step 2. Evaluate  $A_m$  from (32b) with the current value of  $\alpha$  and calculate  $C'_s = A_m^{-1} C_p A_m^{-1+}$  from (31b) as the current estimate of  $C_s$ .

Step 3. Solve  $\alpha$  from either (34) or (35) by using the current value of  $C'_s$ .

Step 4. Repeat Steps 2 and 3 until  $C'_{s12}$ ,  $C'_{s13}$ ,  $C'_{s24}$ , and  $C'_{s34}$  are smaller than a selected threshold, which in practice should be limited by the noise.

Since noise will not be considered in this paper, the threshold is set to be  $10^{-6}$  times  $C'_{s11}$  for the numerical results presented in Section VI.

(The reason for choosing  $10^{-6}$  is because only single precision is used in our computer programming on VAX). At the end of the above iterative procedure,  $C'_s$  will be the final estimate to  $C_s$ .

Here we summarize the overall procedure for calibration. First, the covariance matrix  $C_p$  is calculated from a selected region, and should have rank 3. (One rule of thumb is to select an area with substantial cross polarized backscatter). Then the eigenvector of  $C_p$  with zero eigenvalue, which in practice may not be zero and should be close to the noise floor, is set to be  $Q_z$  and is used to calculate  $Y_c$  from (19). Subsequently,  $R_p$  and  $T_p$  are evaluated using (24) and (25). Finally we find a distributed target which has azimuthal symmetry and evaluate its  $C_z$ . After evaluating  $C_p$  from (31a),  $\alpha$  is then calculated by the iterative procedure and the general solution of  $R$  and  $T$  is therefore determined.

## V. ONE PARC AND ONE RECIPROCAL DISTRIBUTED TARGET

Besides the passive corner reflectors, a set of polarimetric active radar calibrators has been used to calibrate the L band and C-band airborne imaging radar images [2]. The advantage of PARC approach is that a very high signal-to-background-noise ratio can be achieved. The tradeoff is that PARCs are more expensive, and their scattering characteristics are in general more sensitive to the angle of alignment and more susceptible to environmental changes. This section will discuss how to use a PARC with distributed targets for calibration.

Suppose that there is a PARC located inside the scene with the following scattering matrix [2],

$$S_c = \begin{bmatrix} 0 & 1 \\ 0 & 0 \end{bmatrix} \quad (38)$$

Subsequently, substituting (38) into (15) results in the equation for the transformed scattering matrix

$$Y_c = R S_c R^t \quad (39)$$

It is straightforward to show that the general solution of  $R$  has the form

$$R = R_\mu M_\mu^{-1} \quad (40)$$

where the particular solution  $R_\mu$  is

$$R_\mu = R_{11} \begin{bmatrix} 1 & Y_{c11}/Y_{c12} \\ Y_{c22}/Y_{c12} & 1 \end{bmatrix} \quad (41)$$

which satisfies (39), and

$$M_\mu = \begin{bmatrix} 1 & 0 \\ 0 & 1/\beta \end{bmatrix} \quad (42)$$

Here  $\beta$  is a free parameter. In addition, the particular solution of  $T$  is obtained from (8) and is given by

$$T_\mu = Q_\mu^t R_\mu^{-1} Q_\mu^{-1+} \quad (43)$$

It can be shown that the general solution of  $T$  can be written as

$$T = \frac{1}{\beta} M_\mu^{-1} T_\mu \quad (44)$$

Substituting (40) and (44) into (1) and ignoring the proportional constant results in

$$M_\mu^{-1} S M_\mu^{-1} = R_\mu^{-1} X T_\mu^{-1} \quad (45)$$

Let  $X_\mu = R_\mu^{-1} X T_\mu^{-1}$  and vectorize it as  $X_\mu$  by (2). We can relate the covariance matrix,  $C_\mu = E[X_\mu X_\mu^+]$ , to  $C_z$  by

$$C_\mu = A_\mu C_z A_\mu^+ \quad (46)$$

where

$$A_\mu = R_\mu^{-1} \otimes T_\mu^{-1+} \quad (47)$$

Multiplying  $X_\mu$  by  $R_\mu$  from the left hand side and carrying out the ensemble average of the products of the matrix elements gives us

$$C_{\mu 11} = C_{s 11} \quad (48a)$$

$$C_{\mu 12} = C_{\mu 13} = \beta^* C_{s 12} = \beta^* C_{s 13} \quad (48b)$$

$$C_{\mu 14} = \beta^{*2} C_{s 14} \quad (48c)$$

$$C_{\mu 22} = C_{\mu 23} = C_{\mu 33} = |\beta|^2 C_{s 22} = |\beta|^2 C_{s 23} = |\beta|^2 C_{s 33} \quad (48d)$$

$$C_{\mu 24} = C_{\mu 34} = |\beta|^2 \beta^* C_{s 24} = |\beta|^2 \beta^* C_{s 34} \quad (48e)$$

$$C_{\mu 44} = |\beta|^4 C_{s 44} \quad (48f)$$

Here we can see that, in order to solve the parameter  $\beta$ , we need to know the relative magnitudes of the matrix elements of  $C_s$ . Listed are some formulas derived from the above equations,

$$\beta = \left( \frac{C_{s 11} C_{\mu 12}}{C_{s 12} C_{\mu 11}} \right)^* = \left( \frac{C_{s 11} C_{\mu 13}}{C_{s 13} C_{\mu 11}} \right)^* \quad (49a)$$

$$= \frac{C_{s 12} C_{\mu 22}}{C_{s 22} C_{\mu 12}} = \frac{C_{s 13} C_{\mu 23}}{C_{s 23} C_{\mu 13}} \quad (49b)$$

$$= \left( \frac{C_{s 22} C_{\mu 24}}{C_{s 24} C_{\mu 22}} \right)^* = \left( \frac{C_{s 23} C_{\mu 34}}{C_{s 34} C_{\mu 23}} \right)^* \quad (49c)$$

and

$$\beta = \pm \sqrt{\left( \frac{C_{s 11} C_{\mu 14}}{C_{s 14} C_{\mu 11}} \right)^*} \quad (50a)$$

$$= \pm \sqrt{\frac{C_{s 14} C_{\mu 44}}{C_{s 44} C_{\mu 14}}} \quad (50b)$$

Note that only one of the ratios of the matrix elements of  $C_s$  is required beforehand in order to solve  $\beta$ . Also notice that (49) is not applicable to distributed targets with azimuthal symmetry which will result in the cases of zero divided by zero.

As an example for the application of (50), if there are gentle rough surfaces, such as water areas, inside the scene, the Kirchhoff rough surface model predicts that  $C_{s 11} = C_{s 14} = C_{s 44}$ . Here  $C_{s 11}$  and  $C_{s 44}$  correspond to the cross sections of HH and VV responses, respectively, and  $C_{s 14}$  gives the covariance of HH and VV returns. For this case  $\beta$  can be determined from measurements.

The procedure for polarimetric calibration using one PARC and reciprocal distributed targets is similar to the case of trihedral reflectors as discussed at the end of the previous section. Here, as in the trihedral case,  $Q_z$  is calculated from  $C_z$  of the selected distributed target. Subsequently,  $R_\mu$  is calculated using (41) and  $C_\mu$  is evaluated from (46). Finally, an appropriate distributed target is selected to calculate  $\beta$  using (49) and (50). Then,  $R$  and  $T$  are determined from (40) and (44).

## VI. NUMERICAL SIMULATION AND DISCUSSION

In this section numerical simulation of algorithms discussed in previous sections will be presented. First, the parameters of a polarimetric radar are assumed. Then the scattering matrix of a point target and the covariance matrix of a distributed target as would be observed by the polarimetric radar are calculated by using (1) and (5), respectively. Afterwards, the radar parameters evaluated from the calibration algorithms are compared with the assumed system parameters to test the effectiveness of each algorithm.

The polarization transfer matrices of the polarimetric radar are assumed to be

$$R = \begin{bmatrix} 1 & 0.0426\angle -169.5^\circ \\ 0.0532\angle 113.6^\circ & 1.0638\angle -86.3^\circ \end{bmatrix} \quad (51)$$

$$T = \begin{bmatrix} 1 & 0.1042\angle -77.8^\circ \\ 0.0625\angle 30^\circ & 1.0417\angle -57.9^\circ \end{bmatrix} \quad (52)$$

This set of system matrices corresponds to the distortion matrices of the Jet Propulsion Laboratory C-band radar estimated by the three point target approach [11]. Note that the cross-talk errors are smaller than -20 dB and the channel imbalances are around 0.5 dB. The most severe errors are the differences in phases between channels, which significantly distort the co-polarization signature [12] of the trihedral reflectors, Fig. 1, and make it look like that of a dihedral reflector.

Before proceeding with the analysis, let us define the covariance parameters for distributed targets. In this paper, we denote channels 1 and 2 as horizontal (h) and vertical (v) polarizations, respectively. Therefore, the covariance matrix  $C_s$  under this linear polarization basis is defined as

$$C_s = \sigma_{hh} \begin{bmatrix} 1 & \sqrt{\epsilon_{hv}}\rho_{hhv} & \sqrt{\epsilon_{vh}}\rho_{hvh} & \sqrt{\gamma}\rho_{hvv} \\ \sqrt{\epsilon_{hv}}\rho_{hhv}^* & \epsilon_{hh} & \sqrt{\epsilon_{hv}}\epsilon_{vh}\rho_{hvh} & \sqrt{\epsilon_{hv}}\gamma\rho_{hvv} \\ \sqrt{\epsilon_{vh}}\rho_{hvh}^* & \sqrt{\epsilon_{hv}}\epsilon_{vh}\rho_{hvh}^* & \epsilon_{vh} & \sqrt{\epsilon_{vh}}\gamma\rho_{hvv} \\ \sqrt{\gamma}\rho_{hvv}^* & \sqrt{\epsilon_{hv}}\gamma\rho_{hvv}^* & \sqrt{\epsilon_{vh}}\gamma\rho_{hvv}^* & \gamma \end{bmatrix} \quad (53)$$

Here,  $\rho_{\alpha\beta\gamma\delta}$  represents the correlation coefficient of ' $\alpha\beta$ ' and ' $\gamma\delta$ ' polarizations. For distributed targets with azimuthal symmetry,  $\rho_{hhv} = \rho_{hvh} = \rho_{hvv} = \rho_{vhh} = 0$ .

Listed in column 2 of Table 1 are the covariance parameters of the distributed target to be used for the simulation of calibration algorithms, and its co-polarization signature is shown in Fig. 2a. Due to the channel imbalance and cross-talk for the radar defined by (51) and (52), the observed co-polarization signature will be that shown in Fig. 2b. The dominant factor which causes the significant distortion is the phase imbalance between the h and v channels.

After the reciprocity is applied, the co-polarization signature corresponding to the reciprocated covariance matrix  $C_v$  is illustrated in Fig. 2c. It is symmetric with respect to the 90-degree orientation angle unlike the distorted signature, Fig. 2b.

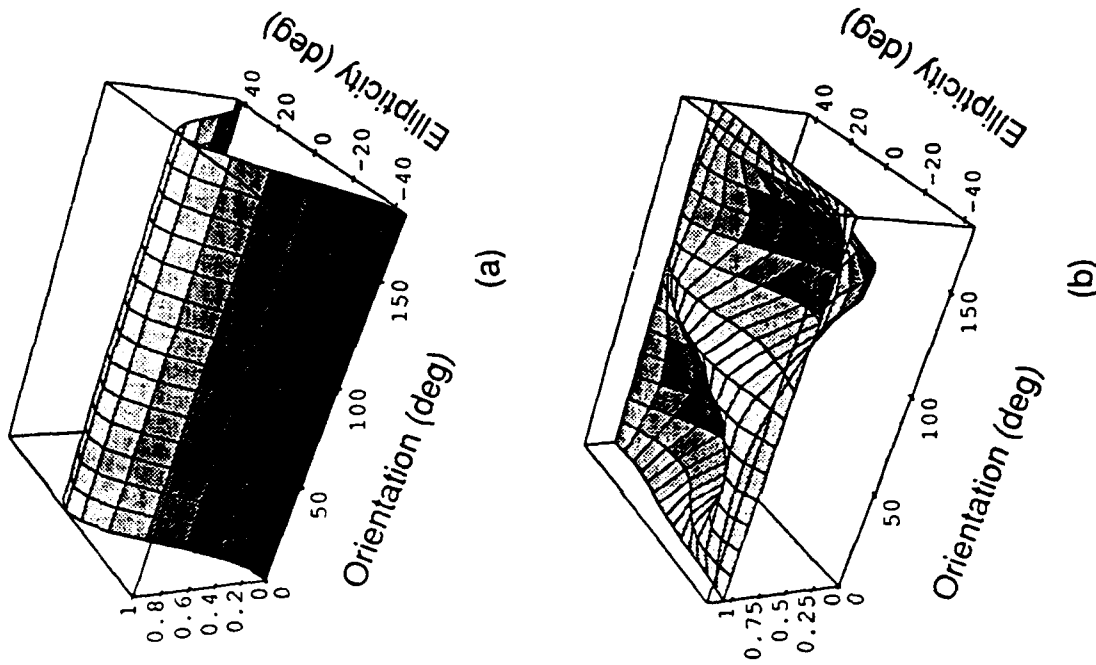


Figure 1. Co-polarization signatures of trihedral reflectors: (a) original and (b) distorted.



Covariance Matrix Parameters	Original and Fully Calibrated	Observed (distorted)	Calibrated by $R_{p1}$ and $T_{p1}$	Calibrated by $R_{p2}$ and $T_{p2}$
$\epsilon_{aa}$	0.1	0.1162	0.1006	0.1006
$\epsilon_{ab}$	0.1	0.1150	0.1006	0.1006
$\gamma$	0.5	0.6104	0.5011	0.5011
$\rho_{AHH}$	0.6	0.5942/144°	0.6012 - 0.044°	0.6012 - 0.044°
$\rho_{AHV}$	0	0.2662/84.97°	0.0532 - 20.9°	0.0532/159.1°
$\rho_{AVH}$	0	0.0742 - 108.7°	0.0532 - 20.9°	0.0532/159.1°
$\rho_{VVH}$	1	0.932/29.45°	1.0	1.0
$\rho_{HVV}$	0	0.1162/57.03°	0.02512 - 22.35°	0.02512/157.7°
$\rho_{VHV}$	0	0.082/106.42°	0.02512 - 22.35°	0.02512/157.7°

Table 1. Original, observed, and calibrated covariance matrix parameters by using the responses from a trihedral reflector and azimuthal symmetric distributed targets.

#### A. One Trihedral Reflector and One Reciprocal Distributed Target

Considered below is the trihedral reflector approach. After the simulation was carried out, two solutions were obtained which are related to each other by (27). It is found that the calibration algorithm accurately obtained the system parameters and took only three iterations to converge, indicating the effectiveness of the iteration scheme. Simulation with larger cross-talk, around ten times the magnitudes of those shown in (51) and (52) ( $\sim 0.5$ ), has also been carried out, and correct estimation of the parameter  $\alpha$  can be achieved within five iterations.

Using these two solutions to calibrate the radar, the calibrated covariance parameters of the distributed target are the same as those given in column 1 of Table 1, due to the fact that both responses from the trihedral reflectors and the azimuthally symmetric distributed targets are invariant under the substitution given by (27).

When azimuthally symmetric distributed targets are not available in the imaged scene, calibration by particular solutions may prove to be effective if the system has good cross-talk isolation like the radar described by (51) and (52).

Particular solutions of the case considered are given by

$$R_{p1} = \begin{bmatrix} 1 & 0 \\ 0.0982/109.24^\circ & 1.062 - 86.40^\circ \end{bmatrix} \quad (54)$$

$$T_{p1} = \begin{bmatrix} 1 & 0.06982 - 96.51^\circ \\ 0.10382/22.21^\circ & 1.04822 - 57.84^\circ \end{bmatrix} \quad (55)$$

and

$$R_{p2} = \begin{bmatrix} 1 & 0 \\ 0.0982/109.24^\circ & 1.062/93.6^\circ \end{bmatrix} \quad (56)$$

$$T_{p2} = \begin{bmatrix} 1 & 0.06982 - 96.51^\circ \\ 0.10382 - 157.79^\circ & 1.04822/122.16^\circ \end{bmatrix} \quad (57)$$

Note that the first solution is very close to the correct system parameters, in particular, the channel imbalance. If the system is calibrated by the particular solution only, the calibrated distributed target parameters are given in columns 4 and 5 of Table 1, and the corresponding polarization signatures are shown in Figs. 2d and 2e, respectively. The polarization signatures are not visibly distinguishable from the correct signature, Fig. 2a. This is due to the fact that the cross-polarization couplings are essentially small for this case and the dominant errors in channel imbalances are essentially removed by the particular solutions.

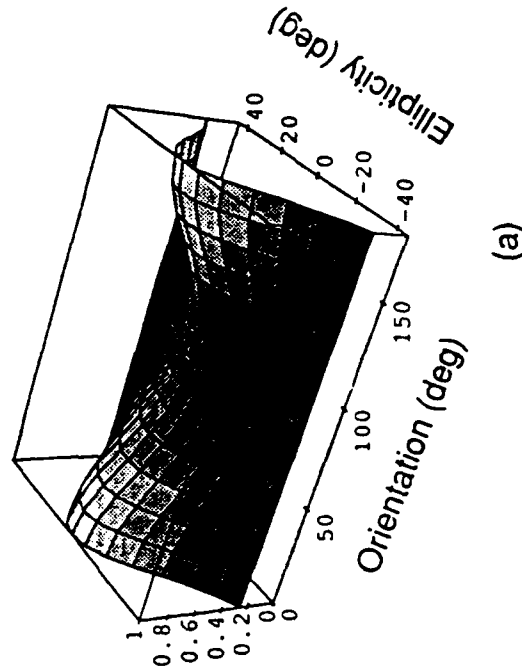
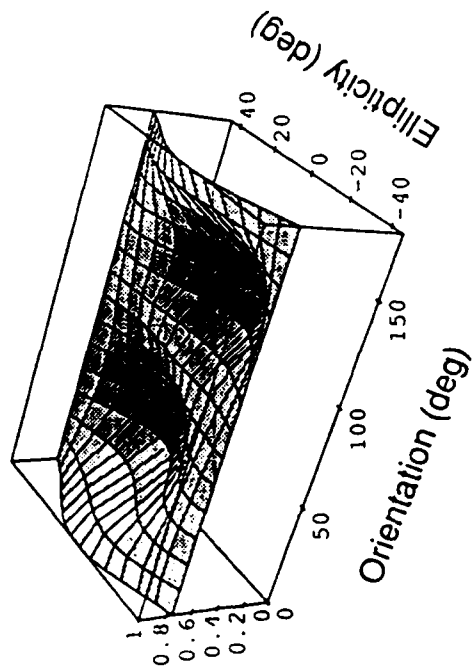
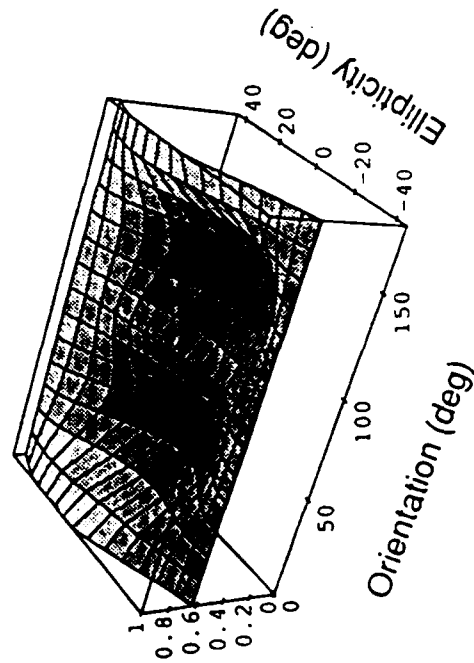


Figure 2. Co-polarization signatures of a distributed target with azimuthal symmetry: (a) original.

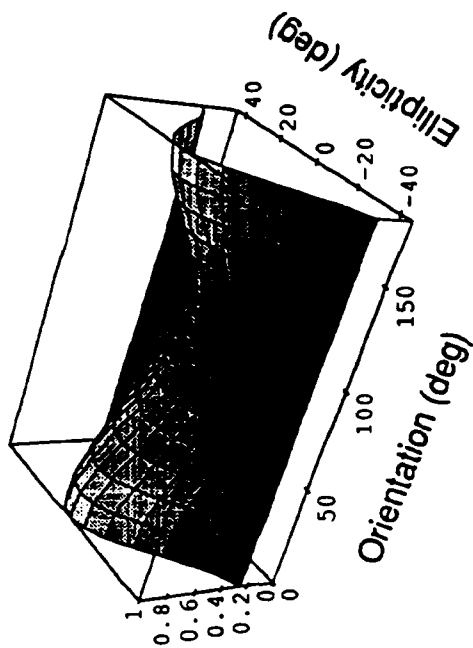


(b)

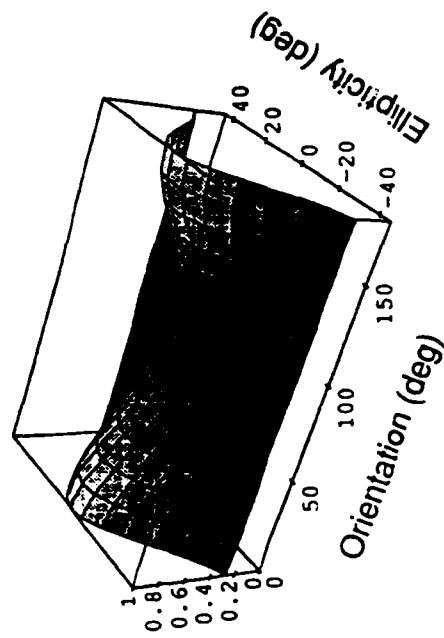


(c)

**Figure 2.** Co-polarization signatures of a distributed target with azimuthal symmetry: (b) distorted ( $C_z$ ), (c) reciprocated ( $C_y$ ).



(d)



(e)

**Figure 2.** Co-polarization signatures of a distributed target with azimuthal symmetry: (d) calibrated by the particular solution,  $R_{p1}$  and  $T_{p1}$ , and (e) calibrated by the particular solution,  $R_{p2}$  and  $T_{p2}$ .

### B. One Polarimetric Active Radar Calibrator and One Reciprocal Distributed Target

To be considered is the PARC approach. In this regard, we assume without loss of generality that the distributed target parameters are given in column 2 of Table 1 and the PARC present in the scene has the scattering matrix defined by (38). As with the trihedral case, the system is assumed to have the parameters given by (51) and (52). After carrying out the simulation, the particular solution is given by

$$R_{\mu} = \begin{bmatrix} 1 & 0.400\angle -83.2^{\circ} \\ 0.0532\angle 113.6^{\circ} & 1.0 \end{bmatrix} \quad (58)$$

$$T_{\mu} = \begin{bmatrix} 1 & 0.1042\angle -77.8^{\circ} \\ 0.0538\angle 116.3^{\circ} & 0.9792\angle 28.4^{\circ} \end{bmatrix} \quad (59)$$

After comparing the above equations with (51) and (52), we can see that  $R_{\mu 21}$  and  $T_{\mu 12}$  are the correct solutions of  $R_{21}$  and  $T_{12}$ . This can be shown by comparing both sides of (40) and (44). Hence, the error that occurred in the estimation of  $\beta$  will only affect the estimation of  $R_{12}$ ,  $R_{22}$ ,  $T_{21}$ , and  $T_{22}$ .

In order to obtain the general solution, we further assume that two of the distributed target parameters,  $\gamma$  and  $\rho_{hhvv}$ , are known. Hence, (50) is applied for the calculation of  $\beta$  and two solutions are obtained. One of the general solutions correctly predicts the system parameters, whereas the other is related to it by (27) with a sign difference in the channel imbalances. By calibrating the system using these two solutions, the calibrated covariance matrix parameters are given in column 2, Table 2 and correctly match the original parameters. It should be noticed that if the correlation coefficients  $\rho_{hhvv}$ ,  $\rho_{hhvh}$ ,  $\rho_{hvvh}$ , and  $\rho_{vhvv}$  are not zeros, then the correlation parameters after being calibrated by the wrong solution will carry an opposite sign.

Also shown in Table 2 are the parameters when the system is calibrated by the particular solution alone. In this case,  $C_{\mu}$  represents the calibrated covariance matrix. Note that all the correlation coefficients are well calibrated except the phase of  $\rho_{hhvv}$ , as expected from (48c) to (48f). Hence, if we have a system with an ideal phase balance between  $h$  and  $v$  channels, then all the correlation coefficients can be well calibrated by the particular solution  $R_{\mu}$  and  $T_{\mu}$ . This implies that the combination of PARCs and reciprocal distributed targets is useful in removing the cross-talks if the system has good channel balances. If further information is provided, such as the ratio of covariance matrix elements of the distributed target or responses from other point targets, then the system can be fully calibrated.

Covariance Matrix Parameters	Original and Fully Calibrated	Observed (distorted)	Calibrated by $R_{\mu}$ and $T_{\mu}$
$\epsilon_{hv}$	0.1	0.1162	0.1132
$\epsilon_{vh}$	0.1	0.1150	0.1132
$\gamma$	0.5	0.6104	0.6404
$\rho_{hhvv}$	0.6	$0.594\angle 144^{\circ}$	$0.6\angle 172.6^{\circ}$
$\rho_{hhhv}$	0	$0.266\angle 84.97^{\circ}$	0
$\rho_{hhvh}$	0	$0.074\angle -108.7^{\circ}$	0
$\rho_{hvvh}$	1	$0.93\angle 29.45^{\circ}$	1.0
$\rho_{vvvv}$	0	$0.116\angle 57.03^{\circ}$	0
$\rho_{vhvv}$	0	$0.08\angle 106.42^{\circ}$	0

Table 2. Original, observed, and calibrated covariance matrix parameters by using the responses from a PARC and azimuthal symmetric distributed targets with known  $\gamma$  and  $\rho_{hhvv}$ .

### C. Comparison of the Trihedral Reflector and PARC Approaches

In the above two sub-sections, two algorithms regarding the calibration using the one point target and the one reciprocal distributed target are simulated for the point target being a trihedral reflector or a polarimetric active radar calibrator. For both cases, the general solutions of the system distortion matrices are written as a product of a particular solution and a matrix with one free parameter which is determined by an additional assumption about the distributed target.

When the particular solution alone is applied for calibration, the residual error is in the form of rotation errors for the trihedral-reflector case, whereas the remaining error is like the channel imbalance for the PARC case. In addition, by comparing the particular solution with the system function, the trihedral-reflector approach is quite robust in calibrating the channel imbalance and weak at detecting the rotation error; hence the cross polarization couplings. In contrast the PARC approach is poor at removing the channel imbalance and useful in estimating the channel cross-talk. Hence, it can be said that these two approaches are complementary to each other. The results indicate that the trihedral-reflector approach is useful when the system has relatively small cross-talk, and the PARC approach is useful when the system has good channel balance. For these two situations, the radar can be well calibrated by using the particular solution only and no further assumption about the distributed targets is necessary.

Nevertheless, in order to fully calibrate a polarimetric system, additional information regarding the distributed targets is required. In this paper, we assume

natural targets with azimuthal symmetry for the trihedral-reflector approach, and one known relative magnitude of distributed target covariance matrix elements for the PARC approach.

Regarding the performance of both approaches, we should notice that the alignment of point targets is less critical in the trihedral-reflector approach than in the PARC approach where the PARCs needs to be carefully aligned in order to avoid artificial cross-talks. The PARC approach, however, can provide a larger signal to noise ratio than the trihedral-reflector approach.

#### ACKNOWLEDGMENTS

This work was supported by the NASA Contract NAGW-1272, the ARMY Corp of Engineers Contract DACA39-87-K-0022, the NASA Grant NAG5-270, and the ONR Contract N00014-83-K-0258.

This work was also sponsored by the Defense Advanced Research Projects Agency. The views expressed are those of the authors and do not reflect the official policy or position of the U.S. Government.

The Editor thanks M. F. Toups and one anonymous Reviewer for reviewing the paper.

#### REFERENCES

1. Barnes, R. M., "Antenna polarization calibration using in-scene reflectors," *Proceedings of the Tenth DARPA/Thi-Service Millimeter Wave Symposium*, U. S. Army Harry Diamond Lab., Adelphi, MD, April 8-10, 1986.
2. Freeman, A., Y. Shen, and C. Werner, "Polarimetric SAR calibration experiment using active radar calibrators," *IEEE Trans. Geosci. Remote Sensing*, Vol. 28, No. 2, 224-240, 1990.
3. Yueh, S. H., J. A. Kong, and R. T. Shin, "Calibration of polarimetric radars using in-scene reflectors," *Progress In Electromagnetics Research*, Elsevier, New York, Vol. 3, Chapter 9, 1990.
4. Yueh, S. H., J. A. Kong, R. M. Barnes, and R. T. Shin, "Calibration of polarimetric radars using in-scene reflectors," *J. Electro. Waves Applic.*, Vol. 4, No. 1, 27-49, 1990.
5. Whitt, M. W., and F. Ulaby, "A polarimetric radar calibration technique with insensitivity to target orientation," *Radio Science*, Vol. 25, No. 6, 1137-1143, 1990.
6. Klein, J. D., "Polarimetric SAR calibration using two targets and reciprocity," *Proc. IGARS '90 Symposium*, 1105-1108, Washington, D.C., May 20-24, 1990.
7. Klein, J. D., and A. Freeman, "Quadrupolarization SAR calibration using target reciprocity," *J. Electro. Waves Applic.*, in press, 1991.
8. Sarabandi, K., and F. Ulaby, "A convenient technique for polarimetric calibration of single-antenna radar systems," *IEEE Trans. Geosci. Remote Sensing*, Vol. 28, No. 6, 1022-1033, 1990.
9. van Zyl, J. J., "Calibration of polarimetric radar images using only image parameters and trihedral corner reflectors responses," *IEEE Trans. Geosci. Remote Sensing*, Vol. 28, No. 3, 337-348, 1990.
10. Borgeaud, M., R. T. Shin, and J. A. Kong, "Theoretical models for polarimetric radar clutter," *J. Electro. Waves Applic.*, Vol. 1, No. 1, 67-86, 1987.
11. Zink, M., F. Heel, and H. Kietzmann, "Airborne SAR calibration," submitted for publication in *J. Electro. Waves Applic.*, 1990.

12. van Zyl, J. J., H. A. Zebker, and C. Elachi, "Imaging radar polarization signature: theory and observation," *Radio Science*, Vol. 22, No. 4, 529-543, 1987.

Simon H. Yueh received the B.S. (1982) and M.S. (1984) from Electrical Engineering Department of National Taiwan University, Taiwan, and the Ph.D. degree in Electrical Engineering in 1991 from Massachusetts Institute of Technology, Cambridge. He is now on the Technical Staff in the SAR Systems Development and Processing Group at the Jet Propulsion Laboratory. His current fields of interest including microwave remote sensing, electromagnetics, and analysis of polarimetric SAR data.

J. A. Kong is Professor of Electrical Engineering and Chairman of Area IV on Energy and Electromagnetic Systems in the Department of Electrical Engineering and Computer Science at the Massachusetts Institute of Technology in Cambridge, Massachusetts. His research interest is in the field of electromagnetic wave theory and applications. He has published seven books and over 300 refereed journal and conference papers, and is the Editor of the Wiley Series in Remote Sensing, and Chief Editor of the Elsevier book series of Progress In Electromagnetics Research (PIER).

Robert T. Shin received his B.S. (1977), M.S. (1980), and Ph.D. (1984) in Electrical Engineering from the Massachusetts Institute of Technology. Since 1984 he has been on the Research Staff in the Air Defense Techniques Group at the MIT Lincoln Laboratory. His research interest is in the areas of electromagnetic wave scattering and propagation and theoretical model development and data interpretation for microwave remote sensing. He is the coauthor of *Theory of Microwave Remote Sensing* (Wiley, 1985). Dr. Shin is a member of the IEEE, American Geophysical Union, Tau Beta Pi, Eta Kappa Nu, and a commission F of the International Union of Radio Science.

# SIMULATION OF FOREST BACKSCATTER AS A FUNCTION OF FOREST AND GROUND PARAMETERS

A. Beaudoin and T. Le Toan

CESR, 9 Ave Colonel Roche, 31400 Toulouse, France / Tel: 61.55.66.71 - Fax: 61.55.67.01

C.C. Hsu, H.C. Han, J.A. Kong and R.T. Shin

MIT, Cambridge MA02139, USA / Tel: (613)253-5625 - Fax: (613)253-0987

## ABSTRACT

To develop an algorithm for retrieving forest biomass using SAR data, a study is performed, which includes: 1) observations on the relation between backscatter and forest biomass, 2) interpretation of the observations by modelling and 3) simulation of radar response for a wide range of forest and ground conditions. This paper presents preliminary results of P-band backscatter simulations as functions of radar incidence angle, ground slope, undergrowth vegetation state, vegetation moisture content, and crown structure.

**Keywords:** P-band SAR backscatter, forest biomass, modelling, simulations, forest and ground parameters.

## 1. INTRODUCTION

The analysis of JPL SAR data over the Landes forest (MAESTRO-1 campaign) revealed strong correlation between L- and especially P-band backscatter  $\sigma^0$  and the pine forest parameters including trunk biomass [1]. However, it was not obvious to conclude about the particular effect of a given forest parameter on  $\sigma^0$  since those parameters were found strongly correlated. To explain the physical link between the P-band backscatter and biomass, a new polarimetric backscattering model, based on the vector radiative transfer theory including a branching model, was developed and successfully validated with the measurements for P-band data [2].

## 2. RELATING P-BAND $\sigma^0$ TO BIOMASS

Fig. 1 presents the main scattering contributions to the P-band  $\sigma^0$  as functions of pine forest age. The major contribution to the HH return is the crown scattering for young forest and trunk-ground double scattering for mature forest. The VV and HV returns are dominated by crown scattering, which comes mainly from the primary branches, modelled as dielectric cylinders. Thus, VV and HV  $\sigma^0$  are directly linked to diameter, length, fractional volume and moisture content of primary branches. For the available age range (8 to 46 yrs), the primary branch mean length and radius were found to vary from 1.2 to 2.5m and 1.2 to 3cm respectively. Therefore  $\sigma^0$  increase with branch

fresh biomass (total volume  $\times$  dry density + water mass) is obvious.

According to this result, high correlation observed between HV and VV returns and trunk biomass [1] is indirect and arises from a correlation between biomass in each tree parts, i.e. the crown and trunk. Fig.2 shows the trunk, branch and total above-ground biomass at the stand level as a function of forest age, derived using an allometric model [3], which estimates tree biomass by parts using the trunk section (tree basal area). Biomass by parts increase quasi-linearly with age and are highly intercorrelated through proportional biomass production relative to total above-ground biomass.

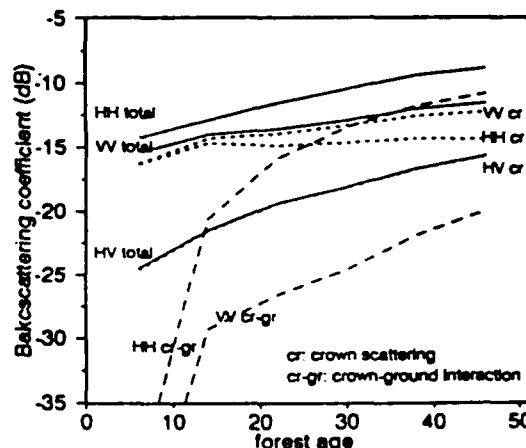


Figure 1: P-band main scattering contributions to HH, HV and VV backscatter as a function of forest age

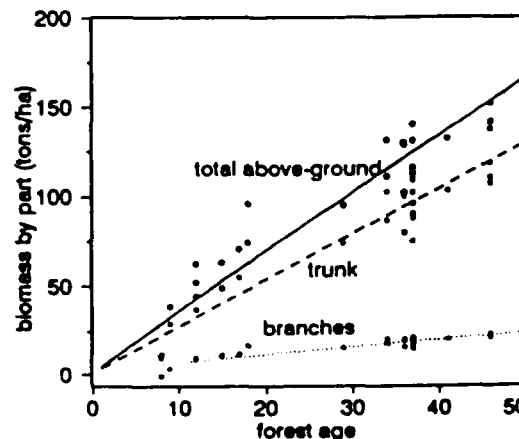


Figure 2: Biomass by part as a function of stand age

The above results provide a significant improvement of our knowledge on the scattering mechanisms of forest canopy. Notice that the VV and HV returns should not be directly affected by environmental conditions in bottom forest layers (bush density, soil moisture, ground slope,...) compared to HH return, but should be affected by crown structure which is highly species dependent. These points are addressed in the following.

### 3. SIMULATION STUDY

#### 3.1 Changing Incidence angle

As P-band yields best sensitivity to biomass, we study the effect of radar incidence angle  $\theta$  on  $\sigma^0$  relative to forest age (hence forest biomass). Fig 3. shows  $\sigma^0$  as a function of  $\theta$  for pine stands at different ages. The peak values have been found in the range 30°-50° depending on the polarization. This also should depend clearly upon the crown structure at HV and VV. Here, an incidence of 40° is particularly adapted, for both  $\sigma^0$  sensitivity to forest age (thus biomass) and for the interesting high HV  $\sigma^0$  values.

#### 3.2 Changing forest and ground parameters

##### Effect of ground slope

Fig.4 presents  $\sigma^0$  as a function of local ground slope facing the radar. As the local slope affects mainly the ground, ground-trunk, crown-ground scattering terms, it is expected that VV and HV will not be changed with varying local slope, whereas HH return should be significantly affected. This is confirmed in Fig 4, where the HH return is fastly decreasing with local slope for old forests where the trunk-ground term dominates, and is approaching to the crown scattering term. No significant changes occur for HV and VV.

##### Effect of undergrowth vegetation

To account for varying understory conditions,  $\sigma^0$  are computed for a canopy without understory vegetation and with a relatively dense bush layer. Since HV and VV return results from the crown scattering, no change is observed. The decrease of  $\sigma^0$  for HH, caused by the attenuation of trunk-ground term, does not exceed 1 dB with the addition of the bush layer (height = 1m, LAI = 1.0)

##### Effect of vegetation moisture condition

To account for variations in vegetation moisture conditions related to seasonal or diurnal effects, the backscatter coefficients are calculated as a function of vegetation gravimetric moisture content from 55% to 65%, HH is not significantly sensitive to this variation, whereas VV and HV returns are more affected, the variation in backscatter coefficient is of the order of 1dB.

##### Effect of crown structure

Relations between the  $\sigma^0$  and forest biomass should be species dependent through the dependence on crown structure. As P-band HV and VV come mainly from primary branches, a major structural parameter to consider is the mean elevation angle  $\beta$  of the primary branch orientation. Fig.5 presents the simulated  $\sigma^0$  as a function of  $\beta$ , for different forest ages observed at 45° incidence. At HV and VV, the maximum sensitivity to forest age is found respectively at 60° ( $\beta$  value for maritime pine) and 45° (plagiophile species). For low  $\beta$  (erectophile species) there is no significant sensitivity to forest age. This is also the case for VV for high  $\beta$  (planophile species). However, for a majority of tree species,  $\beta$  ranges from 45° to 90°. In this range, the sensitivity observed for forest from 6 to 46 years is from 7 to 10 dB in this simulation case. For VV, incidence angles complementary to  $\beta$  should yield the best sensitivity of  $\sigma^0$  to forest biomass. For HH returns, no effect of  $\beta$  on the  $\sigma^0$  sensitivity to biomass is observed, as the return results mainly from trunk-ground interaction. HH is therefore less sensitive to species diversity.

### 4. DISCUSSION AND CONCLUDING REMARKS

At present, the modelling and simulation studies were performed at P-band, which was found optimal for retrieval of forest biomass. HH return was found physically related to both trunk and crown biomass, whereas VV and especially HV returns were found tightly linked to crown biomass and unaffected directly by environmental parameters such as soil moisture, ground local slope and presence of an understory bush layer. Therefore, it is possible to derive total above-ground biomass from P-band HV or VV SAR data, if the relations between biomass found in different tree parts are known. On the other hand, HH return should be less species dependent as contribution of the crown is lower compared to trunk-ground interaction, but is more affected by environment conditions stated above.

### REFERENCES

- [1] T. Le Toan, A. Beaudoin, J. Riou and D. Guyon (1992), "Relating forest biomass to SAR data", IEEE Trans. on Geo. and Rem. Sens., Vol.30, No 2, March 1992.
- [2] C.C. Hsu, H.C. Han, R.T. Shin, J.A. Kong, A. Beaudoin and T. Le Toan (1992), "Radiative Transfer theory for polarimetric remote sensing of pine forest", to appear in IGARSS'92 Proceedings, Houston, TX, USA, May 1992.
- [3] Lemoine B., J. Gelpe, J. Ranger and C. Nys (1986), "Biomasses et croissance du pin maritime. Etude de la variabilité dans un peuplement de 16 ans", Ann. Sci. For., Vol. 43 No. 1, pp. 67-84.

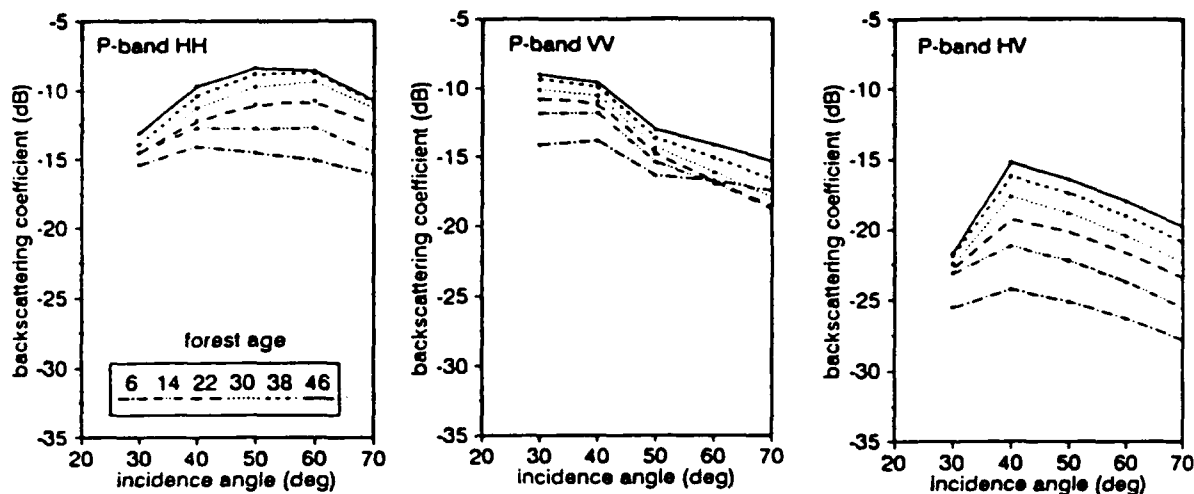


Figure 3 : Effect of incidence angle on pine backscatter at P-band HH,VV and HV

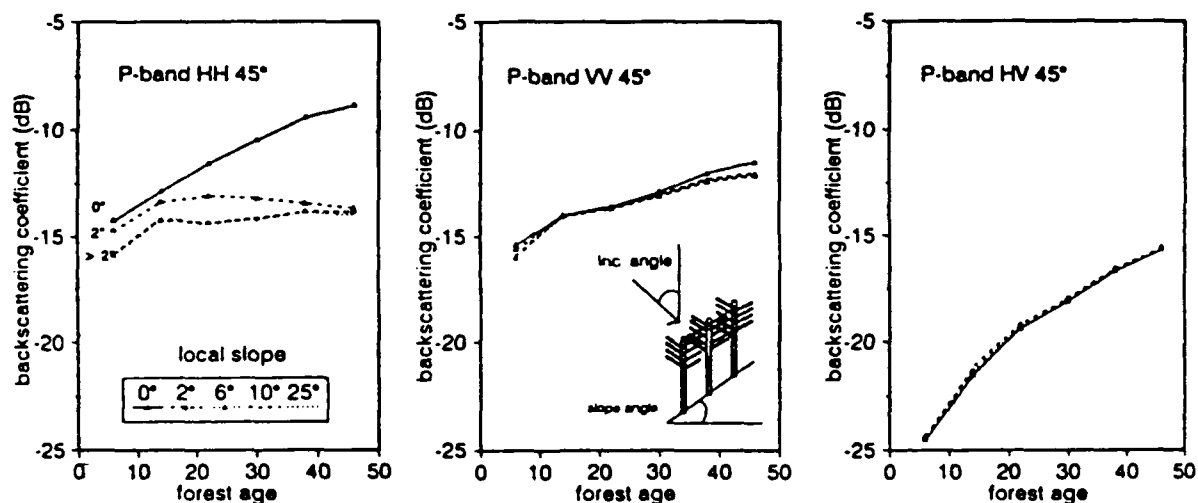


Figure 4 : effect of ground slope on pine backscatter at HH, HV and VV pol.

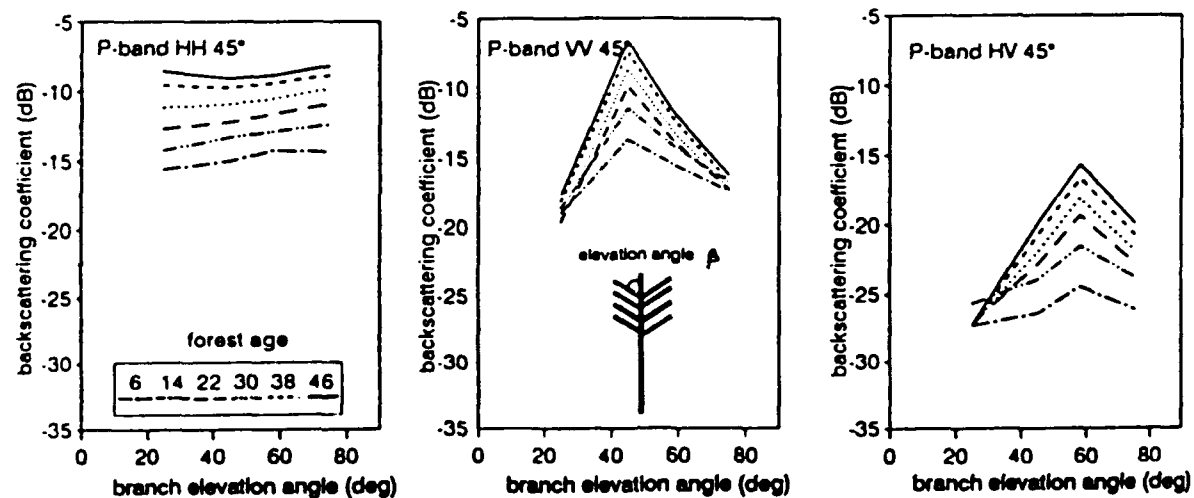


Figure 5 : Simulation of backscattering coefficients as a function of primary branches elevation angle, for 6 forest ages

# Branching Model for Vegetation

Simon H. Yueh, J. A. Kong, *Fellow, IEEE*, Jen King Jao, *Member, IEEE*,  
Robert T. Shin, *Senior Member, IEEE*, and Thuy Le Toan

**Abstract**—A branching model is proposed for the remote sensing of vegetation. The frequency and angular responses of a two-scale cylinder cluster are calculated to demonstrate the significance of vegetation architecture. The results indicate that it is necessary for theoretical models to take into account the architecture of vegetation which plays an important role in determining the observed coherent effects. A two-scale branching model is implemented for soybean with its internal structure and the resulting clustering effects considered. Furthermore, at the scale of soybean fields, the relative location of soybean plants is described by a pair of distribution function. The polarimetric backscattering coefficients are obtained in terms of the scattering properties of soybean plants and the pair distribution function. Theoretical backscattering coefficients evaluated using the hole-correction pair distribution are in good agreement with extensive data collected from soybean fields. Compared with the independent-scatterer pair distribution, it is found that the hole-correction approximation, which prevents two soybean plants from overlapping each other, is more realistic and improves the agreement between the model calculation and experimental data near normal incidence. Extension to a multiscale branching model can be achieved by recursion of the two-scale modeling approach presented in this paper.

## I. INTRODUCTION

THERE has been growing interest in the investigation of vegetation using polarimetric remote sensing measurements. In the past, theoretical models, including continuous random medium and discrete scatterer approaches, have been applied for the electromagnetic modeling of vegetation [1].

Continuous random medium approach utilizes a random process described by a correlation function to represent the permittivity distribution of terrain medium. In this approach, the effective permittivity is evaluated to account for the attenuation and phase delay of wave propagation inside the medium. Subsequently, the polarimetric backscatter coefficients are calculated and used to interpret the scattering from various

geophysical media [1], [2]. This approach has been applied for the interpretation of polarimetric backscattering measurement from vegetation with selected correlation function parameters [2].

Discrete scatterer approach models the medium as a random collection of discrete scatterers with different size and shapes. The relative location of scatterers is described by a pair distribution function, and the backscattering coefficients and effective propagation constants have been evaluated under various approximations [1]. With the application of discrete scatterer theory to vegetation, trunk and branches have been modeled as dielectric cylinders [3], [4], and the internal and scattered fields were estimated by invoking the finite cylinder approximation [5]. To take into account the leaves of deciduous trees, leaves were modeled as dielectric disks [3], [6], and the internal and scattered fields were calculated by using the generalized Rayleigh Gans approximation [3] and the physical optics approximation [7]. In this discrete scatterer approach, the radiative transfer theory was applied for the backscattering cross section of randomly embedded scatterers [8], [9].

Durden *et al.* [4] modeled the forest as the following three layers: the crown layer contained randomly oriented cylinders representing branches; the trunk layer below the crown region contained nearly vertical cylinders representing tree trunks; and the bottom layer was a rough surface representing the forest floor. A radiative transfer approach was also used to evaluate the effective propagation constant and the transfer of the Stokes matrix when the waves traverse through the crown or trunk layer. Because the crown and trunk layers are assumed to be uniform, the propagation effects were then represented by a transmission matrix. Hence the backscattered Stokes matrix was approximated as the sum of five terms corresponding to five different scattering mechanisms. The calculated polarization signatures were shown to be consistent with the observed polarization signatures from forested areas.

However, the form or structure of vegetation has not been addressed in these models. In other words, none of the current models takes into account the differing growth pattern of vegetation or tree architectures. In the book *Fractal Geometry of Nature* [10], Mandelbrot utilized the "pipe model," which describes trees as bundles of nonbranching vessels of fixed diameter, connecting roots to the leaves, to simulate botanical trees. The resulting vegetation patterns are very appealing due to the consideration of vegetation architecture. Besides its significant impact on the vivid simulation of vegetation patterns, architecture or structure is also very important in the computation of electromagnetic scattering and radiation. For

Manuscript received September 30, 1991; revised October 21, 1991. This work was supported by NASA Contract NAGW-1272, The Army Corps of Engineers Contract DACA39-87-K-0022, NASA Grant NAG5-270, ONR Contract N00014-83-K-02580, and U.S. Air Force Contract F19628-90-C-0002.

The views expressed are those of the authors and do not reflect the official policy or position of the U.S. Government.

J. A. Kong is with the Department of Electrical Engineering and Computer Science and Research Laboratory of Electronics, Massachusetts Institute of Technology, Cambridge, MA 02139.

S. H. Yueh was with the Department of Electrical Engineering and Computer Science and Research Laboratory of Electronics at MIT. He is now with the Jet Propulsion Laboratory, Pasadena, CA 91106.

J. K. Jao and R. T. Shin are with the MIT Lincoln Laboratory, Lexington, MA 02173.

T. Le Toan is with the Centre d'Etude Saptiale des Rayonnements, CNRS, 31400 Toulouse Cedex, France.

IEEE Log Number 9105695.



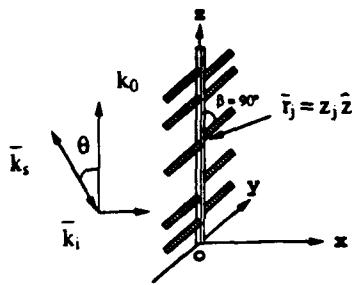


Fig. 1. Configuration of a two-scale cluster with a center cylinder and perpendicularly attached cylinders.

example, the structure of antenna array has significant effects on the radiation pattern and polarizations of fields. Furthermore, by including the concept of multiple scale structure into the antenna, such as the log-periodic array, the antenna array would cover a broad frequency band [11].

In general, vegetation consists of structures of many length scales, and each type of vegetation has its own particular structure and form [12]. Crops have simpler structures and fewer scales, whereas trees have more scales and are more complicated in form. By making an analogy between vegetation and antenna arrays, it can be anticipated that the information pertaining to the structure and biomass of vegetation is embedded in the frequency, angle, and polarization responses of electromagnetic backscatter. Hence, structure, playing an important role in determining the frequency and angular responses of radiation and scattering, should not be ignored in the electromagnetic modeling of vegetation.

In this paper, a branching model is proposed for the remote sensing of vegetation. Section II illustrates the importance of coherence effects observed in the frequency and angular electromagnetic responses of a vegetation-like cluster. Section III presents the modeling approach of a two-scale branching model for soybean. In Section IV, theoretical results are compared with experimental soybean data to validate the proposed model. The approach of a multiscale branching model and related issues for the modeling of vegetation are discussed in Section V.

## II. BRANCHING MODEL FOR A TWO-SCALE CLUSTER

This section is designed to illustrate the approach of branching model and its significance. The approach will be described for the scattering of a scalar field from a two-scale cluster. Examples will be given to demonstrate the effects of coherence on the frequency and angular responses of scattered power which is the quantity of interest.

Fig. 1 illustrates a typical two-scale vegetation cluster with some smaller cylinders attached to a large cylinder. To simplify the computation all the branch elements will be assumed to be mutually independent and statistically identical, independent of their growth locations, and independent of the center trunk.

Scattering from such a cluster can be approximated by a

sum of single scattering terms.

$$S = S_0 + \sum_{j=1}^N S_j \exp(i\xi_j) \quad (1)$$

where  $S_0$  is the return from the center trunk and  $S_j$  represents the response of branch element  $j$ .  $N$  represents the number of branches. A phase factor,  $\xi_j$ , is used to account for the additional phase delay with respect to the reference point "O", and is given as

$$\xi_j = (\bar{k}_i - \bar{k}_s) \cdot \bar{r}_j \quad (2)$$

Here  $\bar{r}_j$  represents the branching location of element  $j$ . Definitions of wave vectors are given in Appendix A.

The scattered power can then be expressed as

$$|S|^2 = |S_0|^2 + \sum_{j=1}^N |S_j|^2 + 2 \sum_{j=1}^N \text{Re}[S_0^* S_j \exp(i\xi_j)] + \sum_{j=1}^N \sum_{i \neq j}^N S_i^* S_j \exp[i(\xi_j - \xi_i)] \quad (3)$$

where "\*" denotes complex conjugate. The third and fourth terms, not having been accounted for in current radiative transfer models of vegetation, take into consideration the phase interference between scattering elements and affect the overall scattering pattern of the cluster.

Employing the assumptions that all the branch elements are statistically identical, mutually independent, uniformly distributed on the trunk, and independent of the center trunk, yields the ensemble average of scattered power,

$$\langle |S|^2 \rangle = \langle |S_0|^2 \rangle + N \langle |S_j|^2 \rangle + 2N \text{Re}[\langle S_0^* \rangle \langle S_j \rangle \langle \exp(i\xi_j) \rangle] + N(N-1) \langle S_i^* \rangle \langle S_j \rangle \langle \exp(-i\xi_i) \rangle \langle \exp(i\xi_j) \rangle. \quad (4)$$

In current radiative transfer models of vegetation, the third and fourth terms in (4) have not been considered in the theoretical models due to the fact that the total phase matrix is calculated as an incoherent sum of the phase matrices of individual elements. Incoherent approximation is valid when the average of a random phase factor,  $\langle \exp(i\xi_j) \rangle$ , is so small that the magnitudes of the last two terms are negligible as compared with the first two terms. However, that may not be valid at lower frequencies and various incident angles for such a cluster like that shown in Fig. 1. Moreover, it can be expected that when  $N$  is a large number, the third and fourth terms in (4) will become significant.

Figs. 2 and 3 illustrate the radar cross section in the backscattering direction versus angles of incidence and frequencies for the two-scale cluster shown in Fig. 1. The center cylinder in Fig. 1 is aligned with the  $z$ -axis, i.e.,  $\bar{r}_j = z_j \hat{z}$ . All the branches are located on  $y$ - $z$  plane, equally probably distributed on both sides of the center cylinder, and perpendicular to the center cylinder.  $\bar{k}_i$  and  $\bar{k}_s$  are on  $x$ - $z$  plane. The finite cylinder approximation [3], [9] is used

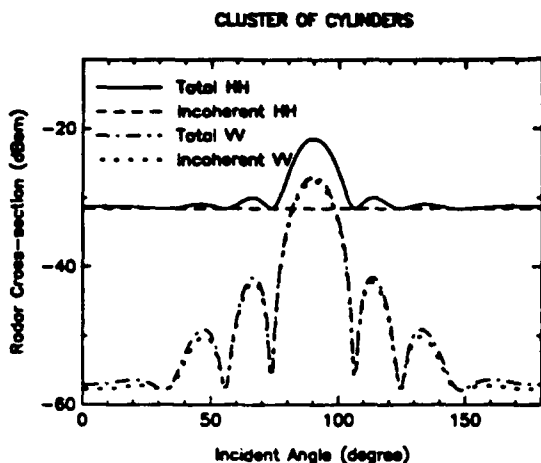


Fig. 2. HH and VV backscattered responses from a two-scale cluster versus incident angle at frequency 5.3 GHz. The dielectric constant of cylinders is  $(29.0 + j9.0)$ . The length and radius of center cylinder are 10 cm and 0.1 cm. The length and radius of branches are 2 cm and 0.1 cm.  $N = 10$ .

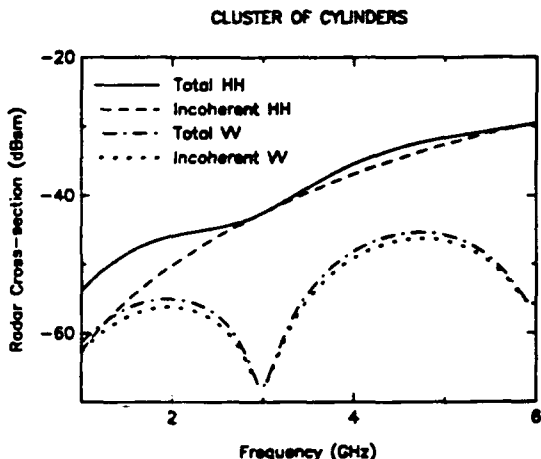


Fig. 3. HH and VV backscattered responses from a two-scale cluster versus frequency at  $\theta = 60$  degree incidence. The dielectric constant of cylinders is  $(29.0 + j9.0)$ . The length and radius of center cylinder are 10 cm and 0.1 cm. The length and radius of branches are 2 cm and 0.1 cm.  $N = 10$ .

to calculate the scattering matrix of center and branching cylinders.

By assuming the branching elements are randomly and independent positioned, the average of random phase factor can be carried out and is given as

$$\langle \exp(i\xi_j) \rangle = \frac{1}{d} \int_0^d \exp(i\xi_j) dz_j = \frac{\exp(i2k_{zi}d) - 1}{i2k_{zi}d} \quad (5)$$

where  $d$  is the length of the center cylinder.

Fig. 2 plots the HH and VV backscatter responses versus the angle of incidence. Note that the incoherent sum for HH [the first two terms in (4)] is a flat curve showing no angular variation. That is due to the fact that HH response is dominated by the branching cylinders and the response from each one has no angular dependence. However, the phase interference which exhibits the structure of this cluster does present itself

in the coherent sum, and results in an observable 10-dB difference between the full coherent sum and the incoherent sum at incident angles near  $90^\circ$  where the phase angle  $\xi_j$  is small and the fields are essentially summed coherently. The 10-dB increase observed is due to the number of branches,  $N$ , being ten for this case. If  $N$  is further increased, the difference will also increase. In the case studied where all the branching elements are perpendicular to V polarization and have small VV response, the total VV backscatter is dominated by the center cylinder. Consequently, there is no significant difference between coherent and incoherent sums. However, if the branches are not perpendicular to the trunk, it can be expected that the difference between the coherent and incoherent sums of VV will be significant.

Fig. 3 plots the HH and VV backscatter versus the frequency at the incident angle  $\theta = 60^\circ$ . Note that the full and incoherent sums of HH show an approximately 10-dB difference at 1 GHz. This is due to the fact that the phase  $\xi_j$  decreases as the frequency decreases and all the branching elements start to act coherently.

Results of Figs. 2 and 3 indicate that it is important to incorporate coherent phase interaction in the calculation of scattering from a collection of scatterers exhibiting clustering structure, which is a typical characteristic of vegetation. As found in this section, the architecture of a cluster clearly displays its own signature in the frequency, angle, and polarization responses. In the following, we will use soybean as an example to illustrate the procedure of implementing a branching model for vegetation and how the phase interaction terms can be properly incorporated.

### III. BRANCHING MODEL FOR SOYBEAN

Soybean, *Glycine*, nowadays constitutes a very most important food legume in China, Korea, Japan, and Malaysia. Large quantities of soybean are also grown in the U.S. [13]. A soybean is an erect branching plant having a stem and terminal branches attached with leaves. The leaf of soybean is so called a compound leaf which is comprised of three leaflets (most species) and a petiole, which is a slender stem supporting the leaflets. A few species have five or seven leaflets on one compound leaf. The leaves usually fall before the fruits (pods) are mature and the pods in general contain two or three seeds. An excellent color illustration showing the architecture and length scale of soybean can be found in [13].

In this section, soybean will be modeled by a two-scale branching model shown in Fig. 4. A leaf will be modeled by a cylinder (petiole) associated with a dielectric disk (leaflets). For convenience, we will use "branch" to represent the cylinder so that the effects of terminal branches (ignored in this simplified soybean picture, Fig. 4) and petioles are both accounted for by this modeling element "branch." Leaf elements and fruits are then connected to a cylinder representing the stem to form the next order cluster—a plant. Eventually, polarimetric backscattering coefficients for soybean fields (a collection of soybean plants) will be derived for correlated soybean locations described by a pair distribution function. In the following, scattering from these two scales regarding the

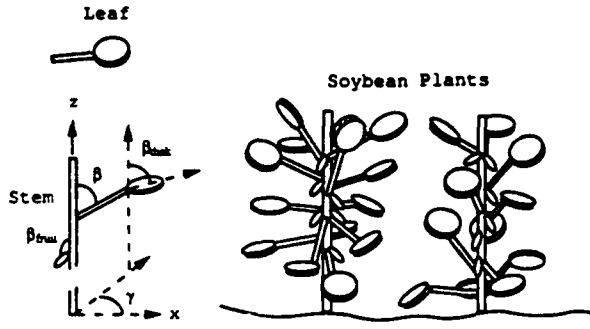


Fig. 4. Configuration of the two-scale branching model for soybean.

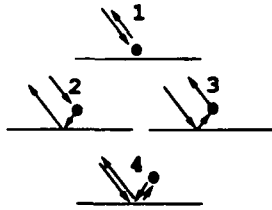


Fig. 5. Four main mechanisms for the scattering from an object above a surface.

inner structure of a soybean plant and the scale related to the distribution of soybean plants will be described separately.

#### A. Leaf

Scattering from a leaf element in the presence of a flat ground surface will be considered in this section. Due to the presence of ground surface, the incident wave may be reflected from the scatterer via four main mechanisms shown in Fig. 5. Hence, after neglecting the reflection from the upper boundary and the multiple scattering between scatterers and ground, the backscattering matrix from a leaf element consists of four main terms, direct (1), scatterer-ground (2), ground-scatterer (3), and ground-scatterer-ground (4), Fig. 5.

Neglecting the multiple scattering between the branch and the circular disk, the total backscattering matrix  $S$  is

$$S_p = S_{0p} + S_{jp} \quad (6)$$

where  $S_0$  is the return from the branch and  $S_j$  is the return from the disk. Subscript "p" denotes one of the four antenna polarization states, HH, HV, VH, and VV, where the first and the second letters denote antenna transmitting and receiving polarizations, respectively. "H" represents horizontal polarization and "V" vertical polarization (Appendix A). Furthermore, each term is constituted by four terms corresponding to four scattering mechanisms (Appendix B),

$$S_{0p} = \sum_{m=1}^4 S_{0mp}$$

$$S_{jp} = \sum_{m=1}^4 S_{jmp} \exp(i\theta_m) \quad (7)$$

The phase factor takes into account the fact that the circular disk (leaflets) is attached to the end of the branch. A translation in the position results in a phase term for the field received by the antenna.

Note that  $S_{0mp}$  ( $S_{jmp}$ ) is not the scattering matrix elements of the branch (disk). In fact,  $S_{0mp}$  and  $S_{jmp}$  consist of a term corresponding to the scattering matrix element of the object, and other terms accounting for the effects of propagation through the other vegetation material and reflection of incident and scattered fields by ground surfaces. Explicit forms for  $S_{0mp}$  or  $S_{jmp}$  are given by (B20)–(B23), Appendix B.

The phase angle  $\theta_m$  can be calculated by using (2) for four scattering mechanisms,

$$\theta_1 = 2(-k_{zi} \cos \gamma \sin \beta + k_{yi} \sin \gamma \sin \beta + k_{zi} \cos \beta)L \quad (8a)$$

$$\theta_2 = 2(-k_{zi} \cos \gamma \sin \beta + k_{yi} \sin \gamma \sin \beta)L \quad (8b)$$

$$\theta_3 = \theta_2 \quad (8c)$$

$$\theta_4 = 2(-k_{zi} \cos \gamma \sin \beta + k_{yi} \sin \gamma \sin \beta - k_{zi} \cos \beta)L \quad (8d)$$

where  $\alpha$ ,  $\beta$ , and  $\gamma$  are the Eulerian angles describing the orientation of the branch ([1], p. 158), and  $L$  is the length of branch.

Note that  $\theta_m$  is a function of the length and orientation angles of the branch. Assuming the size and orientation of branches are independent of the scattering properties of leaves, ensemble average of  $S_p$  yields

$$S_{\text{leaf},p} \stackrel{\text{def}}{=} \langle S_p \rangle = \sum_{m=1}^4 \langle S_{0mp} \rangle + \sum_{m=1}^4 \langle S_{jmp} \rangle \langle \exp(i\theta_m) \rangle \quad (9)$$

and the correlation between "p" and "q" polarizations

$$C_{\text{leaf},pq} \stackrel{\text{def}}{=} \langle S_p S_q^* \rangle$$

$$= \langle S_{0p} S_{0q}^* \rangle + \langle S_{jp} S_{jq}^* \rangle + \langle S_{0p} S_{jq}^* \rangle + \langle S_{jp} S_{0q}^* \rangle \quad (10)$$

where

$$\langle S_{0p} S_{0q}^* \rangle = \sum_{m=1}^4 \sum_{n=1}^4 \langle S_{0mp} S_{0nq}^* \rangle$$

$$\langle S_{jp} S_{jq}^* \rangle = \sum_{m=1}^4 \sum_{n=1}^4 \langle S_{jmp} S_{jnq}^* \rangle \cdot \langle \exp(i\theta_m) \exp(-i\theta_n) \rangle$$

$$\langle S_{0p} S_{jq}^* \rangle = \sum_{m=1}^4 \sum_{n=1}^4 \langle S_{0mp} \exp(-i\theta_n) \rangle \langle S_{jnq}^* \rangle$$

$$\langle S_{jp} S_{0q}^* \rangle = \sum_{m=1}^4 \sum_{n=1}^4 \langle S_{jmp} \rangle \langle S_{0nq}^* \exp(i\theta_m) \rangle \quad (11)$$

Each double sum can be decomposed into a sum of four self terms ( $m = n$ ) and 12 interaction terms between four scattering mechanisms ( $m \neq n$ ). Note that the reciprocity between scattering mechanisms 2 and 3 demands that

$$S_{02ab} = S_{03ba}, \quad (12a)$$

$$S_{j2ab} = S_{j3ba}; \quad a, b = h, v. \quad (12b)$$

Thus, the interaction terms between mechanisms 2 and 3 are essentially equal to the self-terms of mechanisms 2 or 3. In other words, the contribution from mechanisms 2 and 3 should be added coherently. However, these interaction terms have been ignored in the radiative transfer theory.

In the following, the mean and correlation of scattered fields given in (9) and (10) of a leaf element will be combined with the scattering characteristics of the center stem to calculate the polarimetric scattering from a soybean plant.

### B. Soybean Plant

Again by invoking the single scattering approximation, the scattering matrix with polarization "p" from a soybean plant can be written as a sum of the returns from the stem ( $S_0$ ), leaf elements ( $S_{jp}^L$ ), and fruits ( $S_{jp}^F$ ). For simplicity  $S_{0p}$  is assumed to be independent of  $S_{jp}^{L,F}$ , and  $S_{jp}^{L,F}$ 's are statistically identical and mutually independent:

$$S_p = S_{0p} + \sum_{j=1}^{N_l} S_{jp}^L + \sum_{j=1}^{N_f} S_{jp}^F \quad (13)$$

where  $N_l$  represents the total number of leaf elements  $N_f$  the number of fruits. Note that propagation factors have been combined with the scattering matrix of the object to define  $S_{0p}$  and  $S_{jp}$ . Appendix B (B20)–(B23).

The mean scattered field from a soybean plant is given by

$$S_{\text{soybean},p} \stackrel{\text{def}}{=} \langle S_p \rangle = \langle S_{0p} \rangle + N_l \langle S_{\text{leaf},p} \rangle + N_f \langle S_{jp}^F \rangle. \quad (14)$$

Taking the ensemble average of the second moments of scattered field  $S_p$  gives the correlation between "p" and "q" polarizations, as

$$\begin{aligned} C_{\text{soybean},pq} = & \langle S_{0p} S_{0q}^* \rangle + N_l \langle S_{\text{leaf},p} S_{\text{leaf},q}^* \rangle + N_f \langle S_{jp}^F S_{jq}^{F*} \rangle \\ & + \langle S_{0p} \rangle \langle N_l S_{\text{leaf},q}^* + N_f \langle S_{jq}^{F*} \rangle \rangle \\ & + \langle N_l S_{\text{leaf},p} + N_f \langle S_{jp}^F \rangle \rangle \langle S_{0q}^* \rangle \\ & + N_l N_f \langle S_{\text{leaf},p} \langle S_{jq}^{F*} \rangle + S_{\text{leaf},q}^* \langle S_{jp}^F \rangle \rangle \\ & + N_f (N_f - 1) \langle S_{jp}^F \rangle \langle S_{jq}^{F*} \rangle \\ & + N_l (N_l - 1) S_{\text{leaf},p} S_{\text{leaf},q}^* \end{aligned} \quad (15)$$

where all the leaf elements and fruits have been assumed to be mutually independent and statistically identical. Note that in the above expression  $\langle S_{jp}^L \rangle$  and  $\langle S_{jp}^L S_{jq}^{L*} \rangle$  corresponding to the contribution of leaf elements have been replaced by  $S_{\text{leaf},p}$  and  $C_{\text{leaf},pq}$ , respectively.

### C. Scattering from Soybean Fields

In this section, polarimetric backscattering coefficients from a collection of soybean plants within the radar beam footprint will be derived with the correlated locations of soybean plants described by a pair distribution function [1]. Applying single scattering assumption gives the total backscattered field  $S_p$  as

$$S_p = \sum_{m=1}^{N_s} S_{mp} \exp(2i\bar{k}_p \cdot \bar{\rho}_m) \quad (16)$$

where  $N_s$  signifies the total number of soybean plants within the illuminated region.  $\bar{\rho}_m$  represents the location of soybean plant "m",

$$\bar{\rho}_m = x_m \hat{x} + y_m \hat{y} \quad (17)$$

and

$$\bar{k}_p = k_{x1} \hat{x} + k_{y1} \hat{y}. \quad (18)$$

Assuming that all the soybean plants are mutually independent and statistically identical, we obtain the following field correlation,

$$\langle S_p S_q^* \rangle = N_s C_{\text{soybean},pq} + S_{\text{soybean},p} S_{\text{soybean},q}^* \quad (19)$$

where

$$F = \sum_{m=1}^{N_s} \sum_{n \neq m} \langle \exp[2i\bar{k}_p \cdot (\bar{\rho}_m - \bar{\rho}_n)] \rangle. \quad (20)$$

The assumption of statistically identical soybean plants leads to

$$F = N_s(N_s - 1) \int_A d\bar{\rho}_m \int_A d\bar{\rho}_n P_2(\bar{\rho}_m, \bar{\rho}_n) \exp[2i\bar{k}_p \cdot (\bar{\rho}_m - \bar{\rho}_n)] \quad (21)$$

where  $A$  is the illuminated area and  $P_2$  is the probability distribution of the locations of two soybean plants. According to Bayes rule,  $P_2(\bar{\rho}_m, \bar{\rho}_n)$  can be expressed as  $P(\bar{\rho}_m|\bar{\rho}_n)P(\bar{\rho}_n)$ . Assume a uniform distribution for  $\bar{\rho}_n$ , thus,  $P(\bar{\rho}_n) = 1/A$ . Subsequently, a normalized two-point distribution  $g_2$  can be defined by  $g_2(\bar{\rho}_m, \bar{\rho}_n) = AP(\bar{\rho}_m|\bar{\rho}_n)$ . For symmetric and space-invariant relative position distribution,  $g_2(\bar{\rho}_m, \bar{\rho}_n) = g(\bar{\rho}_m - \bar{\rho}_n)$  is called the pair distribution function [1]. Thus,

$$F = \frac{N_s(N_s - 1)}{A} \int_A d\bar{\rho} g(\bar{\rho}) \exp(2i\bar{k}_p \cdot \bar{\rho}). \quad (22)$$

Further assuming  $N_s \gg 1$  and substituting  $F$  into (19) yield

$$\langle S_p S_q^* \rangle = N_s (C_{\text{soybean},pq} + n_s Q S_{\text{soybean},p} S_{\text{soybean},q}^*) \quad (23)$$

where

$$Q = \int_A d\bar{\rho} g(\bar{\rho}) \exp(2i\bar{k}_p \cdot \bar{\rho}) \quad (24)$$

and  $n_s = N_s/A$  is the density of stems (number per unit area)

Several pair distribution functions have been used to evaluate the integral for  $Q$  [1]. For independent scatterer distribution,  $g(\bar{\rho})$  equals one everywhere. For a hole correction approximation, the pair-distribution function has the form

$$g(\bar{\rho}) = \begin{cases} 0, & \rho < R \\ 1, & \rho > R. \end{cases} \quad (25)$$

That means each soybean plant occupies a certain area with a radius  $R$  where the stems of other soybean plants are not allowed to grow. In other words, the minimum spacing between two stems is  $R$ . Outside of that region, stems are uniformly distributed like the independent scatterer assumption.

Let the illuminated area,  $A$ , approach infinity. The integral for  $Q$  is given by

$$Q = 4\pi^2 \delta(\bar{k}_\rho) - \begin{cases} 0, & \text{for independent scatterer} \\ \int_{r < R} d\bar{\rho} \exp(2i\bar{k}_\rho \cdot \bar{\rho}), & \text{for hole correction} \end{cases} \quad (26)$$

where the integral can be carried out and given as

$$\int_{r < R} d\bar{\rho} \exp(2i\bar{k}_\rho \cdot \bar{\rho}) = \pi R^2 \frac{2J_1(2k_\rho R)}{2k_\rho R}. \quad (27)$$

To obtain the expression of  $R$  for the hole correction, we assume that  $N_s \pi R^2 = \mu A$  which relates the area of soybean canopy to the total illuminated area, where  $\mu$  is a constant determining the minimum spacing between stems. Thus,

$$R = \sqrt{\frac{\mu}{\pi n_s}}. \quad (28)$$

The correlation of measured polarizations for oblique incidence ( $\bar{k}_\rho \neq 0$ ) reduces to

$$\langle S_p S_q^* \rangle = N_s \left[ C_{\text{soybean},pq} - 2\mu \frac{J_1(x)}{x} S_{\text{soybean},p} S_{\text{soybean},q}^* \right] \quad (29)$$

where

$$x = 2k_0 R \sin \theta_i. \quad (30)$$

To ensure the power of each polarization  $\langle S_p S_p^* \rangle$  is always greater than zero, parameter  $\mu$  must be smaller than one. Also note that when  $\mu = 0$ , the hole correction reduces to the independent scatterer assumption.

The polarimetric covariance matrix [2] having the unit as the backscattering cross section per unit area is defined by

$$\sigma_{pq} = \frac{4\pi}{A} \langle S_p S_q^* \rangle. \quad (31)$$

Substituting (29) into (31) and summing up the contribution from a rough vegetation floor give the total polarimetric backscattering coefficients as

$$\sigma_{pq} = 4\pi n_s \left[ C_{\text{soybean},pq} - 2\mu \frac{J_1(x)}{x} S_{\text{soybean},p} S_{\text{soybean},q}^* \right] + \alpha_{pq} \sigma_{\text{ground},pq} \quad (32)$$

where  $\sigma_{\text{ground},pq}$  is the contribution from a rough terrain surface. Kirchhoff approximation will be used in our soybean model to compute  $\sigma_{\text{ground},pq}$  [1]. Furthermore, due to the attenuation introduced by the vegetation cover,  $\sigma_{\text{ground},pq}$  is multiplied by a factor  $\alpha_{pq}$  which is calculated in the following manner. The propagation factor due to the vegetation cover appearing in (B20) for each polarization is evaluated at the bottom of the vegetation layer ( $z_s = -d_2$ ). Multiplying the propagation factor of "p" polarization with the complex conjugate of that of "q" polarization yields the factor  $\alpha_{pq}$ .

#### D. Models of Vegetation Elements

In the implementation of the above branching model for soybean, dielectric cylinders are used to represent stems, branches, and fruits, whereas leaflets are represented by dielectric disks. Scattering matrices are obtained by using the finite cylinder approximation for cylinder [3], [9] and the physical optics approximation for disk [6], [7]. Note that in [3], [6], [7], and [9] the  $\exp(i\omega t)$  convention was used and the vector definitions of horizontal and vertical polarizations are also different from those defined by (A3a) and (A3b). Therefore, scattering matrices are rederived using the  $\exp(-i\omega t)$  notation and definitions of polarization vectors (Appendix A) for these two elements [14]. These formulas were shown to be applicable over a wide range of frequencies. However, it is known that both approximations give nonreciprocal bistatic scattering matrices. To ensure the reciprocity, the scattering matrices in reciprocal directions are averaged. For oriented cylinders or disks, three Euler angles are used to specify the orientation of these scatterers. The scattering matrix of each element is calculated in its local coordinates and then transformed back to the antenna coordinates.

#### E. Treatment of Coherent Wave Propagation

The propagation is accounted for by using the Foldy's approximation, Appendix C. Note that the forward scattering matrix of a two-scale or multiscale system is simply the sum of forward scattering matrices from every components if the multiple scattering between scattering elements is ignored. Note that the averaging processes for the propagation and scattering of the waves are carried out independently in this paper, which is an approximation.

### IV. COMPARISON OF THEORETICAL RESULTS WITH EXPERIMENTAL DATA

#### A. Ground Truth of Soybean Data

The soybean data analyzed were backscattering coefficients of HH, HV, and VV measured at 5.3 GHz by the Centre d'Etude Spatiale des Rayonnements in France over a 2 1/2-month period in 1986. The height of radar was fixed at 14.5 m. and the 3-dB beamwidth of radar is 9.2°. Each of the data set was measured at three polarizations for six incident angles. Along with backscattering coefficients, extensive ground truth, including vegetation fractional volume ( $f$ ), water content, canopy height ( $h$ ), ground surface roughness (correlation length  $l$  and standard deviation  $\sigma$ ), and soil moisture [16], is summarized in Table I with the calculated permittivity for vegetation and soil. The soil at the experimental site contains 11.1% sand, 61.7% loam, and 27.2% clay [16]. The first column (date) corresponds to the time when the data were collected. For example, 0717 represents July 17, 1986. The permittivity of vegetation material was deduced [16] using the formula given in [17] based on the measured volumetric water content. The permittivity of vegetation material showing a decreasing trend is due to the fact that the measured volumetric water content of soybean decreased during the experimental period [16]. The permittivity of ground soil was calculated

TABLE I  
MEASURED AND CALCULATED GROUND TRUTH PARAMETERS

Date	$h$ (m)	$f$ (%)	Vegetation $\epsilon$	$\sigma$ (cm)	$l$ (cm)	Soil $\epsilon$	Plant Density $n_s$ (No./m <sup>2</sup> )
0717	0.20	0.11	67.64 + i 20.75	1.7	14	13.09 + i 2.65	18
0725	0.29	0.18	60.07 + i 18.44	1.7	14	9.33 + i 1.64	18
0807	0.44	0.29	48.93 + i 15.13	1.6	14	11.93 + i 2.34	18
0814	0.52	0.60	45.44 + i 14.10	1.6	14	15.57 + i 3.34	18
0820	0.59	0.87	40.22 + i 12.55	1.5	13	7.02 + i 1.04	18
0828	0.68	0.89	32.43 + i 10.23	1.4	13	16.50 + i 3.60	18
0903	0.745	0.88	28.77 + i 9.14	1.3	12	8.76 + i 1.49	18
0912	0.825	0.68	24.62 + i 7.90	1.2	12	5.59 + i 0.68	18

TABLE II  
ESTIMATED FRACTIONAL VOLUMES OF VEGETATION COMPONENTS

Date	Leaves (%)	Branches and Stems (%)	Fruits (%)
0717	0.055	0.055	0
0725	0.09	0.09	0
0807	0.135	0.149	0.006
0814	0.247	0.310	0.043
0820	0.32	0.45	0.1
0828	0.293	0.36	0.237
0903	0.264	0.29	0.326
0912	0.175	0.196	0.309

in accordance with the soil texture and moisture using the formula given in [18] and has been reported in [16]. Note that the vegetation fractional volume increases at the early stage and stays constant at the fully grown stage. Afterwards, a decrease of the fractional volume is due to the fall of leaves and steady drying of vegetation material.

In addition, the weight of vegetation components was measured at 5 different days (0804, 0820, 0902, 0915, and 1003) and the fractional weight was plotted versus the day in Fig. 6 where day 1 represents July 17 and day 80 represents October 4. Note that the weights of branches and stems were not measured separately. The fruits appeared at August 7 and their weight became dominant at the end of the season reaching approximately 50% of the total vegetation weight. Due to the fact that weight measurements in general were carried out at different days from the time when the backscatter was measured, the fractional weight of each component at the days (Table I, Column 1) when the radar measurements were carried out was estimated by linearly interpolating the measurements. Further assuming the densities (weight per unit volume) of all the vegetation elements are the same, the fractional volumes of vegetation components were estimated as the product of their fractional weight and the total vegetation fractional volume (Table I, Column 3) and listed in Table II.

Some other parameters necessary for theoretical calculation are selected in the following manner. The length of stem is set to be the measured canopy height and one vegetation layer is assumed so that  $d_1 = d_2$ . Other parameters shown in Table III regarding the size and density of vegetation components are adjusted so that their fractional volumes match those shown in Table II. Hence, there are only six independent parameters (one for disks, three for branches and stem, and two for fruits)

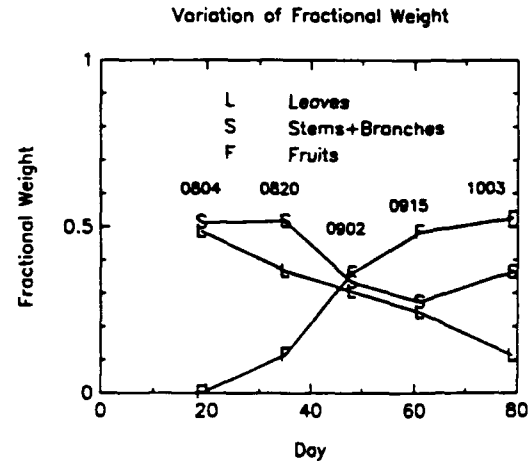


Fig. 6. Fractional weight of soybean components at 5 different days (0804, 0820, 0902, 0915, and 1003).

for each date in Table III, which are selected in such a way that a good agreement between theoretical results and experimental data is reached. Note that  $N_t(N_f)$  is calculated by multiplying the density of branches (fruits) with the height of canopy.

In selecting the parameters listed in Table III, the sizes of vegetation elements are ensured to agree with botany studies. For example, the thickness of disk (~0.2–0.3 mm) agrees well with the usual thickness of soybean leaflets. The radius of disks is chosen so that the area of disk corresponds to the total area of three leaflets. It can be seen that the radii of disk, stem, branch, and fruit are in good agreement with the sizes shown in the illustration of soybean elements [13]. Moreover, the radius of the disk agrees very well with the measured average area of a leaf at 4 days as shown in Fig. 7 where the radius for a circular disk with the same area is also indicated.

In addition, the probability distributions of orientation angles of disk, branch, and fruit are chosen to be

$$P(\beta) = \begin{cases} \frac{16}{3\pi} \sin^4 \beta, & \text{if } 0 \leq \beta \leq \frac{\pi}{2} \\ 0, & \text{otherwise.} \end{cases} \quad (33)$$

$$P(\beta_{\text{disk}}) = \begin{cases} \sin \beta_{\text{disk}}, & \text{if } \frac{\pi}{2} \leq \beta_{\text{disk}} \leq \pi \\ 0, & \text{otherwise.} \end{cases} \quad (34)$$

$$P(\beta_{\text{fruit}}) = \begin{cases} |\sin(2\beta_{\text{fruit}})|, & \text{if } \frac{\pi}{2} \leq \beta_{\text{fruit}} \leq \pi \\ 0, & \text{otherwise.} \end{cases} \quad (35)$$

$$P(\gamma) = P(\gamma_{\text{fruit}}) = \frac{1}{2\pi} \quad (36)$$

TABLE III  
SELECTED PARAMETERS FOR THEORETICAL CALCULATION

Date	Disk Radius (cm)	Disk Thickness (mm)	Branch Radius (cm)	Branch Length (cm)	Density of Branches (No./m)	Stem Radius (cm)	Fruit Radius (cm)	Fruit Length (cm)	Density of Fruits (No./m)
0717	4.0	0.22	0.12	10	27.5	0.24	—	—	0
0725	4.3	0.24	0.16	9	36	0.275	—	—	0
0807	4.8	0.25	0.2	11	41	0.3	0.25	2.0	8
0814	5.0	0.27	0.23	11	63	0.44	0.3	3.0	28
0820	5.1	0.32	0.25	11	69	0.55	0.4	3.0	37
0828	5.4	0.31	0.25	11	57	0.5	0.5	3.6	47
0903	5.2	0.31	0.24	11	54	0.44	0.5	4.0	57
0912	4.7	0.31	0.2	11	45	0.4	0.49	4.0	57

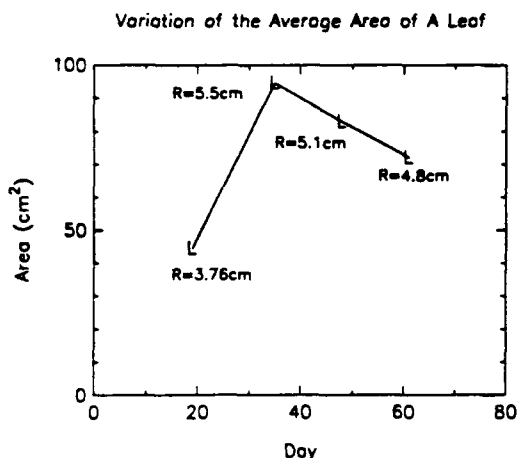


Fig. 7. Measured average area of a leaf at 4 days same as the first 4 days for the data shown in Fig. 6. The radius of a circular disk of the same area is indicated.

so that branches are more horizontally distributed and disks (leaflets) tend to bend toward the ground to account for the effects of gravitational force. As to the fruits, most of them are inclined  $45^\circ$  downward in accordance with the illustration shown in [16]. Uniform distributions for  $\gamma$  and  $\gamma_{\text{fruit}}$  are selected in order to have an azimuthally symmetric soybean canopy. There was no detailed ground truth measurement on the structure of the soybean at the time when the experiment was carried out. Hence, the above probability density functions were selected so that a good agreement between theory and data is achieved. To avoid introducing additional parameters, the same orientation distributions are used for all data sets.

#### B. Comparison of Theoretical Results with Experimental Data

Figs. 8(a)–(h) compare experimental data with theoretical results which are calculated using (33) for  $\mu = 1$  (hole correction). There is a good agreement between theoretical results and experimental data except for the data sets where the fractional volumes of vegetation are small (early stages of soybean). For the first data set, theoretical contribution from the ground surface alone is 3 dB near normal incidence, which is larger than the measured backscattering coefficients. That may be due to either the surface scattering model (Kirchhoff approximation) is not appropriate for this case or the measured roughness parameters of ground are not accurate

enough. According to a simulation using [1, eq. (59b)] based on Kirchhoff approximation, it is found that a 10% error in  $\sigma$  and  $l$  can result in a change of 1 dB for surface scattering.

Using the vegetation parameters for date 0814, Fig. 9 illustrates the deficiency of independent scatterer assumption ( $\mu = 1$ ) which is not a good description for soybean plant distribution. As observed from vegetation like trees and crops, there is always a certain spacing between plants. In other words, individual plant tends to exclude other plants from its territory. Hence, hole correction is more appropriate for this situation. Note that the peaks observed in the HH and VV backscatter for independent scatterer assumption near normal incidence are greatly reduced by using the hole correction factor  $\mu = 1$ , and the theoretical results at higher angles of incidence are essentially unaffected where both  $2J_1(x)/x$  and  $S_{\text{soybean},p}$  are observed to be small. The reduction of the sharp peaks near normal incidence is due to the destructive interference introduced by the hole correction approximation which prevents two soybean plants from overlaying each other. It should also be noticed that the cross polarized return HV is not affected by the hole correction. This is due to the fact that the coherent backscatter  $S_{\text{soybean},hv}$  is zero for azimuthally symmetric canopy. In order to fully demonstrate the effects of coherence, experimental data collected at many frequencies in conjunction with sufficient ground truth data must be used. The soybean data presented in this paper has extensive ground truth, but the measurement was limited to C-band. For soybean, because its internal scales are in general of the order or greater than the wavelength at 5.3 GHz, we do not expect the coherence effect to be significant at C-band. We expect that coherence will be significant at lower frequencies such as L- and P-bands.

#### V. DISCUSSION

In this paper, a two-scale branching model has been implemented for soybean and validated with experimental data. To generalize the above model to vegetation with more branching scales, such as trees, the following procedure can be applied. The model for trees will consist of several scales including trunk, bough, branch, twig, and leaves. In the branching process, the leaves are first attached to the smallest branch (twig). The resulting clustered twig-leaves pattern is then attached to a larger branch to form the next order clustering. Repeating this process with branches attached to bough and

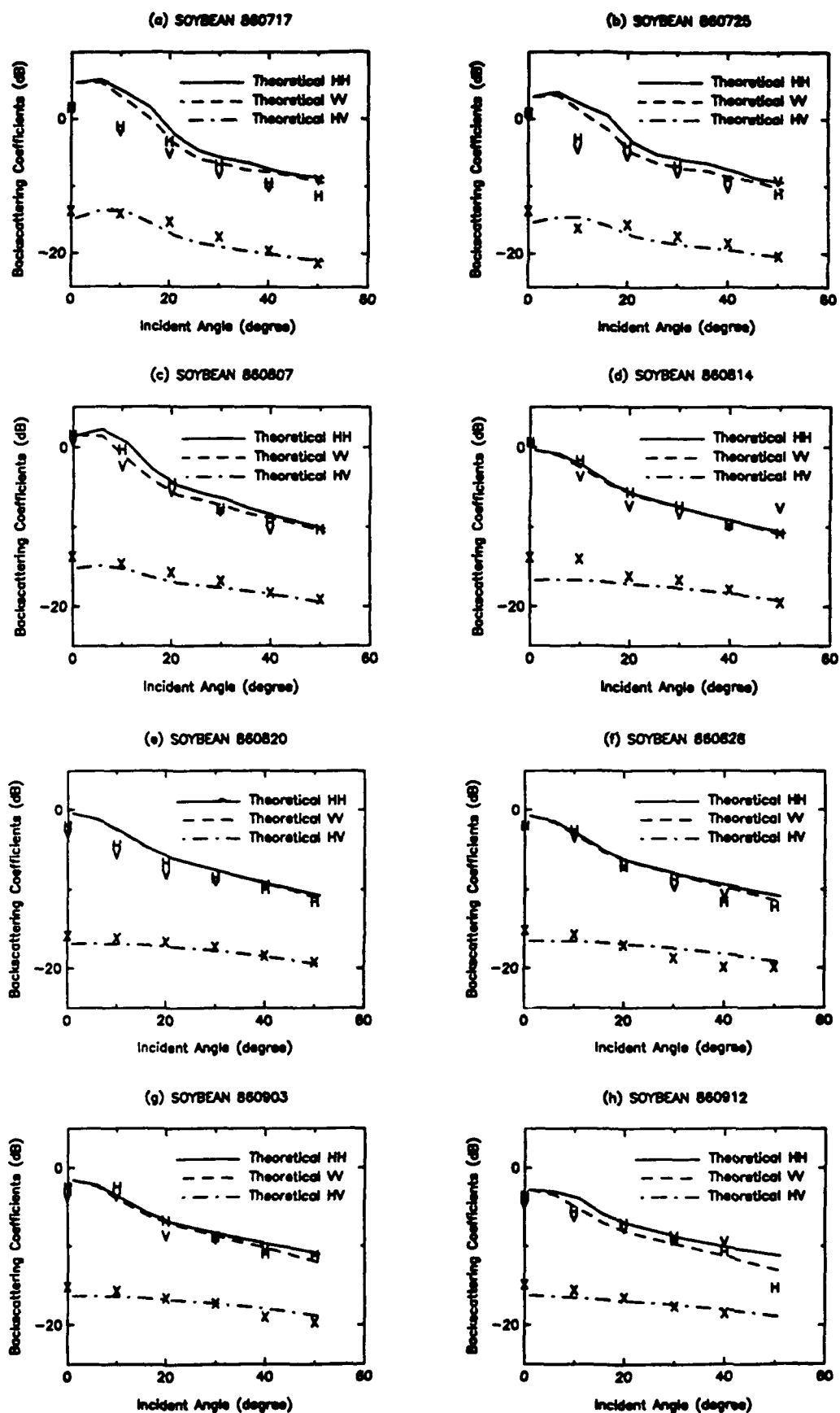


Fig. 8. Comparison of theoretical results and experimental data. Hole correction with  $\mu = 1$  is used for the pair-distribution function of soybean plants. H, V, and X represent measured backscattering coefficients of HH, VV, and HV polarizations, respectively.



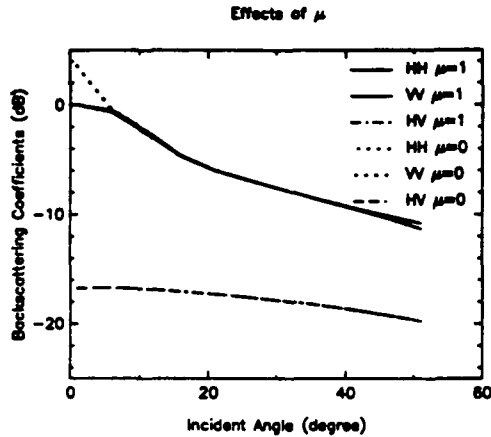


Fig. 9. Comparison of theoretical results generated by independent scatterer approximation ( $\mu = 1$ ) and hole correction  $\mu = 0$ . Parameters for date 0814 are used for calculation.

boughs attached to trunk finally forms a tree. By changing the sizes and growth direction of each scale, various tree patterns can be generated.

A recursive procedure can be used to calculate the backscattering parameters for trees by taking advantage of their branching architecture. For a tree with the above multiscale pattern, the problem of scattering from a multiscale structure can be decoupled into a cascade of scattering from two-scale structures (subscale and primary scale). For example, in the case of the smallest clustering, subscale corresponds to leaves and primary scale represents a twig. The averages polarimetric scattering matrix and covariance matrix of a two-scale structure can be expressed in terms of those of subscale and primary scale. The resulting averaged polarimetric scattering matrix and covariance matrix will correspond to those of the subscale of the next order two-scale structures. Repeating the above recursive procedure eventually leads to the averaged scattering matrix and covariance matrix of a tree. For example, a branching model for soybean is implemented by following the above procedure.

The advantages of this modeling approach over the conventional methods are that the multiscale structure of vegetation is considered and the coherence or phase interference between each component is taken into account. In the past, theoretical models did not consider the structure of vegetation. The phase interaction between vegetation components was ignored and an incoherent sum was used to compute the total scattering power from every components. In the multiscale branching model, the phase interaction or coherence, which can be observed at the inner scales of a single plant and the spatial scale of plant distribution, is retained. Hence, the model should be applicable over a larger frequency spectrum and range of incident angles than the conventional approaches for remote sensing of vegetation.

#### APPENDIX A

##### NOTATION AND DEFINITION OF VECTORS

The notation and definition of wave vectors and polarization vectors are given in this appendix (Fig. 10). The wave vector

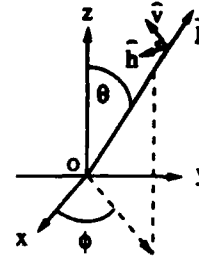


Fig. 10. Illustration of vector definition of wave vector  $\vec{k}$  and polarization vectors.

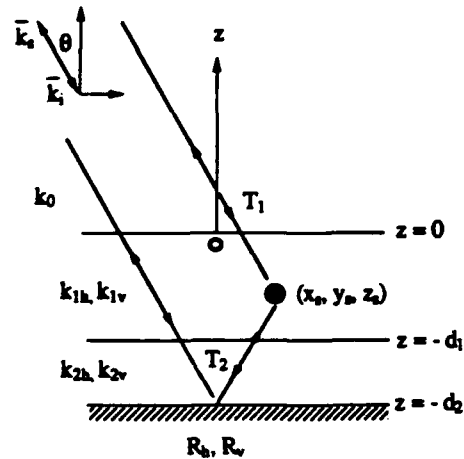


Fig. 11. Configuration of a scattering object located inside a layered medium.

of a wave propagating in the direction  $(\theta, \phi)$ , is defined as

$$\vec{k} = \hat{x}k_x + \hat{y}k_y + \hat{z}k_z \quad (\text{A1})$$

where

$$k_x = k_0 \cos \phi \sin \theta \quad (\text{A2a})$$

$$k_y = k_0 \sin \phi \sin \theta \quad (\text{A2b})$$

$$k_z = k_0 \cos \theta \quad (\text{A2c})$$

where  $k_0$  is the free space wavenumber. The horizontal and vertical polarization vectors of electric fields are defined as

$$\hat{h}(k_z) = \frac{\vec{k} \times \hat{z}}{\vec{k} \times \hat{z}} = \frac{\hat{x}k_y - \hat{y}k_x}{k_p} \quad (\text{A3a})$$

$$\hat{v}(k_z) = \frac{\hat{h} \times \vec{k}}{\hat{h} \times \vec{k}} = \frac{-\hat{x}k_x k_z - \hat{y}k_y k_z + \hat{z}k_p^2}{k_0 k_p} \quad (\text{A3b})$$

The above definition is used for both incident and scattered fields. For an incident wave with direction of incidence  $(\theta_i, \phi_i)$ , its wave vector is denoted as

$$\vec{k}_i = \hat{x}k_{xi} + \hat{y}k_{yi} + \hat{z}k_{zi} \quad (\text{A4})$$

where

$$k_{xi} = k_0 \cos \phi_i \sin \theta_i \quad (\text{A5a})$$

$$k_{yi} = k_0 \sin \phi_i \sin \theta_i \quad (\text{A5b})$$

$$k_{zi} = k_0 \cos \theta_i \quad (\text{A5c})$$

In the same manner, the wave vector of a scattered field is defined as

$$\bar{k}_s = \hat{x}k_{xs} + \hat{y}k_{ys} + \hat{z}k_{zs} \quad (A6)$$

where

$$k_{xs} = k_0 \cos \phi_s \sin \theta_s \quad (A7a)$$

$$k_{ys} = k_0 \sin \phi_s \sin \theta_s \quad (A7b)$$

$$k_{zs} = k_0 \cos \theta_s \quad (A7c)$$

and  $(\theta_s, \phi_s)$  is the direction of propagation.

#### APPENDIX B

##### SCATTERING FROM AN OBJECT INSIDE A LAYERED MEDIUM

Consider the case that a scatterer is located in a layered medium as shown in Fig. 11, characterized by the effective propagation constants,  $k_{1h}, k_{1v}, k_{2h}$ , and  $k_{2v}$  for coherent wave propagation (Appendix C). The vegetation has been assumed to have azimuthal symmetry such that  $M_{hv} = M_{vh} = 0$  in (C1) and (C2), Appendix C.

Assuming that the effective propagation constants of the middle layers are close to  $k_0$  (free space wavenumber) such that reflection and refraction due to the upper two boundaries can be ignored, we can approximate the total backscattering by the sum of four terms.

$$S = \sum_{i=1}^4 S_i \quad (B1)$$

Expressing each term explicitly yields

$$S_1 = T_1 F(\pi - \theta_i, \pi + \phi_i; \theta_i, \phi_i) T_1 \quad (B2)$$

$$S_2 = T_2 F(\theta_i, \pi + \phi_i; \theta_i, \phi_i) T_1 \quad (B3)$$

$$S_3 = T_1 F(\pi - \theta_i, \pi + \phi_i; \pi - \theta_i, \phi_i) T_2 \quad (B4)$$

$$S_4 = T_2 F(\theta_i, \pi + \phi_i; \pi - \theta_i, \phi_i) T_2 \quad (B5)$$

where  $F(\theta_s, \phi_s; \theta_i, \phi_i)$  is the scattering matrix of the object with the angle of incidence  $(\theta_i, \phi_i)$  and the angle of observation  $(\theta_s, \phi_s)$ .

There are two paths that the wave can reach the scatterer and be reflected back to the receiver. Two transfer matrices,  $T_1$  and  $T_2$ , are utilized to describe the propagation effects of the upper and lower paths, respectively,

$$T_1 = \exp(i\phi_1) \begin{bmatrix} \exp(i\phi_{1h}) & 0 \\ 0 & \exp(i\phi_{1v}) \end{bmatrix} \quad (B6)$$

$$T_2 = \exp(i\phi_2) \begin{bmatrix} \exp(i\phi_{2h}) R_h & 0 \\ 0 & \exp(i\phi_{2v}) R_v \end{bmatrix} \quad (B7)$$

where  $R_h$  and  $R_v$  are the Fresnel reflection coefficients of a flat surface for horizontal and vertical polarizations.

By selecting origin "O" as the reference for the phases of incident and scattered waves, if the scatterer is located in the upper middle layer  $(-d_1 \leq z_s \leq 0)$ , the phases are given by

$$\phi_{1h} = -k_{1h} \frac{z_s}{\cos \theta} \quad (B8)$$

$$\phi_{1v} = -k_{1v} \frac{z_s}{\cos \theta} \quad (B9)$$

$$\phi_{2h} = k_{1h} \frac{d_1 + z_s}{\cos \theta} + 2k_{2h} \frac{d_2 - d_1}{\cos \theta} + k_{1h} \frac{d_1}{\cos \theta} \quad (B10)$$

$$\phi_{2v} = k_{1v} \frac{d_1 + z_s}{\cos \theta} + 2k_{2v} \frac{d_2 - d_1}{\cos \theta} + k_{1v} \frac{d_1}{\cos \theta} \quad (B11)$$

$$\phi_1 = k_{x1} x_s + k_{y1} y_s + \frac{k_{\rho 1}^2}{k_0 \cos \theta} z_s \quad (B12)$$

$$\phi_2 = k_{x1} x_s + k_{y1} y_s - \frac{k_{\rho 1}^2}{k_0 \cos \theta} (z_s + 2d_2) \quad (B13)$$

On the other hand, if the scatterer is positioned in the lower middle layer  $(-d_2 \leq z_s \leq d_1)$ , these phases are given by

$$\phi_{1h} = k_{1h} \frac{d_1}{\cos \theta} - k_{2h} \frac{z_s + d_1}{\cos \theta} \quad (B14)$$

$$\phi_{1v} = k_{1v} \frac{d_1}{\cos \theta} - k_{2v} \frac{z_s + d_1}{\cos \theta} \quad (B15)$$

$$\phi_{2h} = k_{1h} \frac{d_1}{\cos \theta} + k_{2h} \frac{d_2 - d_1}{\cos \theta} + k_{2h} \frac{d_2 + z_s}{\cos \theta} \quad (B16)$$

$$\phi_{2v} = k_{1v} \frac{d_1}{\cos \theta} + k_{2v} \frac{d_2 - d_1}{\cos \theta} + k_{2v} \frac{d_2 + z_s}{\cos \theta} \quad (B17)$$

$$\phi_1 = k_{x1} x_s + k_{y1} y_s + \frac{k_{\rho 1}^2}{k_0 \cos \theta} z_s \quad (B18)$$

$$\phi_2 = k_{x1} x_s + k_{y1} y_s - \frac{k_{\rho 1}^2}{k_0 \cos \theta} (z_s + 2d_2) \quad (B19)$$

where  $k_{1h}$  and  $k_{1v}$  are the propagation constants of horizontal and vertical polarized waves for layer 1, and similarly,  $k_{2h}$  and  $k_{2v}$  for layer 2. The above expressions can be derived by computing the path lengths for the waves propagating in each layer and multiplying them by the effective wavenumber in each layer.

Substituting (B6) and (B7) into (B2)–(B5) and carrying out the matrix multiplication explicitly gives (B20–23) below, where the scattering matrix elements  $f_{ab}$ , which represents the scattering matrix element for  $b$  polarization incidence and "a" polarization receiving, are evaluated in the directions of incidence and scattering corresponding to (B2)–(B5), respectively. Note that  $S_1, S_2, S_3$ , and  $S_4$  including the effects of scatterer,

$$S_1 = \begin{bmatrix} f_{hh} \exp[2i(\phi_1 + \phi_{1h})] & f_{hv} \exp[i(2\phi_1 + \phi_{1h} + \phi_{1v})] \\ f_{vh} \exp[i(2\phi_1 + \phi_{1h} + \phi_{1v})] & f_{vv} \exp[2i(\phi_1 + \phi_{1v})] \end{bmatrix} \quad (B20)$$

$$S_2 = \begin{bmatrix} f_{hh} R_h \exp[i(\phi_1 + \phi_{1h} + \phi_2 + \phi_{2h})] & f_{hv} R_h \exp[i(\phi_1 + \phi_{1v} + \phi_2 + \phi_{2h})] \\ f_{vh} R_v \exp[i(\phi_1 + \phi_{1h} + \phi_2 + \phi_{2v})] & f_{vv} R_v \exp[i(\phi_1 + \phi_{1v} + \phi_2 + \phi_{2v})] \end{bmatrix} \quad (B21)$$

$$S_3 = \begin{bmatrix} f_{hh} R_h \exp[i(\phi_1 + \phi_{1h} + \phi_2 + \phi_{2h})] & f_{hv} R_v \exp[i(\phi_1 + \phi_{1h} + \phi_2 + \phi_{2v})] \\ f_{vh} R_h \exp[i(\phi_1 + \phi_{1v} + \phi_2 + \phi_{2h})] & f_{vv} R_v \exp[i(\phi_1 + \phi_{1v} + \phi_2 + \phi_{2v})] \end{bmatrix} \quad (B22)$$

$$S_4 = \begin{bmatrix} f_{hh} R_h^2 \exp[2i(\phi_2 + \phi_{2h})] & f_{hv} R_h R_v \exp[i(2\phi_2 + \phi_{2h} + \phi_{2v})] \\ f_{vh} R_h R_v \exp[i(2\phi_2 + \phi_{2h} + \phi_{2v})] & f_{vv} R_v^2 \exp[2i(\phi_2 + \phi_{2v})] \end{bmatrix} \quad (B23)$$

propagation effects, and ground reflection, are the resulting scattering matrices as would be observed by the receiver for four main scattering mechanisms.

### APPENDIX C PROPAGATION OF COHERENT FIELDS UNDER FOLDY'S APPROXIMATION

For sparse media like vegetation, Foldy's approximation [1], [15], [19], [20] can be employed to account for the absorption and scattering effects introduced by the medium. The propagation of coherent wave with  $E_h$  and  $E_v$  as the horizontal and vertical components of the electric field is governed by the following [1, p. 139]:

$$\frac{dE_h}{ds} = (ik_0 + M_{hh})E_h + M_{hv}E_v \quad (C1)$$

$$\frac{dE_v}{ds} = M_{vh}E_h + (ik_0 + M_{vv})E_v \quad (C2)$$

where  $s$  is the distance along the direction of propagation, and

$$M_{jl} = \frac{i2\pi n_0}{k_0} \langle f_{jl}(\theta, \phi; \theta, \phi) \rangle; \quad j, l = v, h. \quad (C3)$$

Here  $(\theta, \phi)$  is the direction of propagation, and  $n_0$  is the density of scatterers (number per unit volume). In the above equation, the average is carried out over the size and orientation of embedded vegetation elements. For the soybean model presented in Section III,

$$M_{jl} = \frac{i2\pi}{k_0} \frac{n_s}{h} \left[ \langle f_{jl, \text{stem}}(\theta, \phi; \theta, \phi) \rangle + N_l \langle f_{jl, \text{branch}}(\theta, \phi; \theta, \phi) \rangle + N_l \langle f_{jl, \text{disk}}(\theta, \phi; \theta, \phi) \rangle + N_f \langle f_{jl, \text{fruit}}(\theta, \phi; \theta, \phi) \rangle \right] \quad (C4)$$

where  $h$  is the height of vegetation canopy,  $n_s$  is the number of stems per unit area, and  $N_l$  and  $N_f$  are, respectively, the average number of branches and fruits per stem.

If the canopy structure exhibits statistically azimuthal symmetry, there will be no coupling between horizontal and vertical components of the coherent field. It can be shown that

$$M_{hv} = M_{vh} = 0. \quad (C5)$$

Hence, the effective propagation constant of horizontally and vertically polarized coherent waves are given by

$$k_h = k_0 + \frac{M_{hh}}{i} \quad (C6)$$

$$k_v = k_0 + \frac{M_{vv}}{i} \quad (C7)$$

### REFERENCES

- [1] L. Tsang, J. A. Kong, and R. T. Shin, *Theory of Microwave Remote Sensing*. New York: John Wiley & Sons, 1985.
- [2] M. Borgeaud, S. V. Nghiem, R. T. Shin, and J. A. Kong, "Theoretical models for polarimetric microwave remote sensing of earth terrain," *J. Electromagnetic Waves and Appl.*, vol. 3, no. 1, pp. 61-81, 1989.
- [3] M. A. Karam, A. K. Fung, and Y. M. M. Antar, "Electromagnetic wave scattering from some vegetation samples," *IEEE Trans. Geosci. Remote Sensing*, vol. 26, pp. 799-808, Nov. 1988.
- [4] S. L. Durden, J. J. van Zyl, and H. A. Zebker, "Modeling and observation of the radar polarization signature of forested areas," *IEEE Trans. Geosci. Remote Sensing*, vol. 27, pp. 290-301, May 1989.
- [5] H. C. van de Hulst, *Light Scattering by Small Particles*. New York: Dover, 1981.
- [6] R. H. Lang and H. A. Saleh, "Microwave inversion of leaf area and inclination angle distributions from backscattered data," *IEEE Trans. Geosci. Remote Sensing*, vol. GE-23, pp. 685-694, Sep. 1985.
- [7] David M. Le Vine, A. Schneider, R. H. Lang, and H. G. Carter, "Scattering from thin dielectric disks," *IEEE Trans. Antennas Propagat.*, vol. AP-33, pp. 1410-1413, Dec. 1985.
- [8] L. Tsang, M. C. Kubasci, and J. A. Kong, "Radiative transfer theory for active remote sensing of a layer of small ellipsoidal scatterers," *Radio Sci.*, vol. 16, no. 3, pp. 321-329, 1981.
- [9] M. A. Karam and A. K. Fung, "Electromagnetic scattering from a layer of finite length, randomly oriented, dielectric, circular cylinders over a rough interface with application to vegetation," *Int. J. Remote Sensing*, vol. 9, no. 6, pp. 1109-1134, 1988.
- [10] B. Mandelbrot, *Fractal Geometry of Nature*. New York: W. H. Freeman Company, 1983.
- [11] E. C. Jordan and K. G. Balmain, *Electromagnetic Waves and Radiating Systems*. Englewood Cliffs, NJ: Prentice-Hall, 1972.
- [12] G. L. Hightshoe, *Native Trees, Shrubs, and Vines for Urban and Rural America*. New York: Van Nostrand Reinhold, 1988.
- [13] M. Neushul, *Botany*. Santa Barbara, CA: Hamilton Publishing Company, 1974, p. 471.
- [14] S. H. Yueh, "Electromagnetic and statistical models for polarimetric remote sensing of vegetation," Ph.D. dissertation, Massachusetts Institute of Technology, Feb. 1991.
- [15] R. H. Lang, "Electromagnetic backscattering from a sparse distribution of lossy dielectric scatterers," *Radio Sci.*, vol. 16, pp. 15-33, 1981.
- [16] T. Le Toan, A. Beaudoin, D. L. S. Chong, J. A. Kong, S. V. Nghiem, and H. C. Han, "Study of microwave interaction with the Earth's surface," ESA Rep. ESTEC/No. 8447/89/NL/PB(SC), 1990.
- [17] F. T. Ulaby and M. A. El-Rays, "Microwave dielectric spectrum of vegetation—Part II: Dual-dispersion model," *IEEE Trans. Geosci. Remote Sensing*, vol. GE-25, no. 5, pp. 550-557, 1987.
- [18] M. T. Hallikainen, F. T. Ulaby, M. A. El-Rays, and L. K. Wu, "Microwave dielectric behaviour of wet soil—Part I: Empirical models and experimental observations," *IEEE Trans. Geosci. Remote Sensing*, vol. GE-23, pp. 25-34, Jan. 1985.
- [19] T. Oguchi, "Attenuation and phase rotation of radio waves due to rain: Calculation at 19.3 and 34.8 GHz," *Radio Sci.*, vol. 8, pp. 32-38, 1973.
- [20] A. Ishimaru and C. W. Yeh, "Matrix representation of the vector radiative transfer equations for randomly distributed nonspherical particles," *J. Opt. Soc. Am.*, vol. 1, pp. 359-364, 1984.



Simon H. Yueh received the B.S. and M.S. degrees in electrical engineering from the National Taiwan University, Taiwan, in 1982 and 1984, respectively, and the Ph.D. degree in electrical engineering from the Massachusetts Institute of Technology, Cambridge, MA, in 1991.

He is now on the technical staff in the SAR Systems Development and Processing Group at the Jet Propulsion Laboratory. His fields of interest are electromagnetics and remote sensing.



J. A. Kong (S'65-M'69-SM'74-F'85) is Professor of Electrical Engineering and Chairman of Area IV on Energy and Electromagnetic Systems in the Department of Electrical Engineering and Computer Science at the Massachusetts Institute of Technology in Cambridge, MA. His research interest is in the field of electromagnetic wave theory and applications. He has published 7 books and over 300 refereed journal and conference papers, and is the Editor of the Wiley Series in Remote Sensing, and Chief Editor of the Elsevier book series of Progress In Electromagnetics Research (PIER).



Jen King Jao (S'70-M'71-S'72-M'75) was born on October 31, 1945 in China. He received the Baccalaureate degree in 1968 from the Department of Electrophysics of National Chiao-Tung University, Taiwan and the Ph.D. degree in 1975 from the Department of Electrical Engineering and Computer Science of Massachusetts Institute of Technology.

Since then, he has worked in Riverside Research Institute and Raytheon Company before joining the MIT Lincoln Laboratory as a technical staff member. He has done substantial work in the studies and

measurements of optical and radar systems. His current activities concentrate on airborne radar systems and clutter.



Robert T. Shin (S'82-M'83-SM'90) received the B.S., M.S., and Ph.D. degrees in electrical engineering from the Massachusetts Institute of Technology in 1977, 1980, and 1984, respectively.

He has been with the Air Defense Techniques Group at the MIT Lincoln Laboratory as a research staff member, since 1984, and as a senior staff member, since 1989. His research interests are in the areas of electromagnetic wave scattering and propagation and theoretical model development and data interpretation for microwave remote sensing.

He is the coauthor of *Theory of Microwave Remote Sensing* (Wiley, 1985).

Dr. Shin is a Senior Member of IEEE and a member of The Electromagnetics Academy, AGU, Tau Beta Pi, Eta Kappa Nu, and Commission F of the International Union of Radio Science.



Thuy Le Toan received the Engineer degree and the Ph.D. degree in physics from the Paul Sabatier University, Toulouse, France.

In 1973, she joined the Centre d'Etude Spatiale des Rayonnements, where she is presently leader of the Remote Sensing Group. Since 1980, her research activity has been in the area of microwave remote sensing applied to vegetation. Her research interests include experimentation and modeling of microwave interaction with agricultural and forested media, and analysis of SAR images. She has served as the Project Coordinator and Principal Investigator of several microwave airborne experiments in Europe and is the Principal Investigator of ERS-1 and SIR-C projects.

# **THEORETICAL MODELING FOR PASSIVE MICROWAVE REMOTE SENSING OF EARTH TERRAIN**

**by**

**J. A. Kong**

**Center for Electromagnetic Theory and Applications**

**Research Laboratory of Electronics and**

**Department of Electrical Engineering and Computer Science**

**Massachusetts Institute of Technology**

**Cambridge, Massachusetts 02139, USA**

**TEL: 617-253-5625**

**FAX: 617-253-0987**

## **Abstract**

In this paper we address the issue of theoretical modeling for passive microwave remote sensing of terrain media such as snow, ice, vegetation, and periodic surfaces. Historically, the volume scattering effects stimulated the development of the continuous random medium model and the random discrete scattering model for the description of the media. Theoretical treatments were developed along two different paths. Invoking the principle of reciprocity, the wave theory based on Maxwell's equations has been used to calculate the emissivity. The other approach was to start with the radiative transfer equations and solved for the brightness temperatures directly. Attempts have been made to derive the radiative transfer theory from the wave theory. At the same time, both theoretical approaches have been used to calculate the radiometric emissions and to interpret experimentally measured data.

The successful interpretation of the Cosmos 243 data was perhaps the first most important step towards a serious development of the continuous random medium model to account for the volume scattering effects of snow ice fields. Subsequent interpretation of measurement results from snow field with both passive radiometers and active radar systems established a unique position for its description of earth terrain media. Recent efforts in classifying sea ice with correlation function characterization are demonstration of acceptance of this model. Future inverse scattering developments will perhaps rely heavily on this model.

# Direct and Inverse Methods in Radar Polarimetry

## Part 2

edited by

**Wolfgang-M. Boerner**

Communications & Sensing Laboratory,  
EECS Department,  
University of Illinois at Chicago, U.S.A.

**Hans Brand**

High-Frequency Engineering  
Laboratories, University Erlangen-  
Nürnberg, Germany

**Leonard A. Cram**

Thorn EMI, Electronics Ltd., U.K.

**William A. Holm**

GTRI-RAIL/MAL,  
Atlanta, GA,  
U.S.A.

**David E. Stein**

Westinghouse Electric Corporation,  
Baltimore, MD,  
U.S.A.

**Werner Wiesbeck**

IHE, University of Karlsruhe,  
Karlsruhe, Germany

**Wolfgang Keydel**

DLR, Institute for Radio-Frequency  
Technology, Oberpfaffenhofen, Germany

**Dino Giuli**

Radar Research Laboratory,  
Department of Electronics Engineering,  
University of Florence, Italy

**Dag T. Gjessing**

ESTP, Royal Norwegian Council of  
Industrial & Scientific Research, Kjeller,  
Norway

**Frédéric A. Molinet**

Société Mothesim,  
Le Plessis-Robinson,  
France



**Kluwer Academic Publishers**

Dordrecht / Boston / London

Published in cooperation with NATO Scientific Affairs Division

# THEORETICAL MODELS FOR POLARIMETRIC MICROWAVE REMOTE SENSING OF EARTH TERRAIN

M. Borgeaud  
DFVLR

Institute for Radiofrequency Technology  
German Aerospace Research Establishment  
Oberpfaffenhofen  
D-8031 Wessling  
Federal Republic of Germany

and

J.A. Kong, R.T. Shin and S. V. Nghiem  
Department of Electrical Engineering and Computer Science  
Massachusetts Institute of Technology  
77 Massachusetts Avenue  
Cambridge, MA 02139  
U.S.A.

## Abstract

Earth terrains are modeled by a two-layer configuration with a random permittivity described by a three-dimensional correlation function with horizontal and vertical correlation lengths and variances. Using the wave theory with Born approximations carried to the second order, this model is applied to derive the polarimetric backscattering coefficients of the Mueller and covariance matrices. From a physical point of view, the Born first- and second-order approximations account for the single and double scattering processes, respectively.

For the isotropic random permittivity configuration, five out of the nine elements of the covariance matrix are zero under the Born first-order approximation. For the uniaxial tilted random permittivity case, the covariance matrix does not contain any zero elements. To account for the azimuthal randomness in the growth direction of leaves in tree and grass fields, an averaging scheme is developed in which the backscattering coefficients are averaged over the azimuthal direction. In this case, the covariance matrix is described by four zero elements though the tilt angle is different from zero. Applying the Born approximation to the second-order, the covariance matrix is computed for the isotropic and the uniaxial untilted random permittivity configurations. The covariance matrix has four zero elements, and a depolarization factor is obtained, even for the isotropic case.

To describe the effect of the random medium on electromagnetic waves, the strong permittivity fluctuation theory, which accounts for the losses due to both of the absorption and the scattering, is used to compute the effective permittivity of the medium. For a mixture of two components, only the frequency, the correlation lengths, the fractional volume, and the permittivities of the two constituents are needed to obtain the polarimetric backscattering coefficients. Theoretical predictions are illustrated by comparing the results with experimental data for vegetation fields and sea ice.

## Introduction

For many types of earth terrain, the scattering effects due to medium inhomogeneities play an important role in the determination of radar backscattering coefficients. The volume scattering properties of a medium have been successfully modeled by the random permittivity fluctuations [1]. The random medium is characterized by a background permittivity and a random permittivity fluctuation modeled by a three-dimensional correlation function with horizontal and vertical correlation lengths and variances.

The objective of this paper is to develop a mathematically rigorous, fully polarimetric model to compute the covariance matrices in the backscattering direction for different kinds of earth terrains with a two-layer configuration medium with either an isotropic or an anisotropic random permittivity. Of all the analytical wave approaches to the study of scattering by random medium, the Born approximation is the simplest. An integral equation is first formed for the electric field using the unperturbed Green's function in the absence of permittivity fluctuations. The integral equation is then solved by iteration with the iteration series known as the Born series. With both the first and second terms of this series which respectively describes a single and a double scattering processes, the polarimetric backscattering coefficients are computed.

## Scattering, Mueller, and Covariance Matrices

Consider an electromagnetic plane wave propagating in the direction  $\bar{k}$ .

$$\bar{E} = (E_h \hat{h} + E_v \hat{v}) e^{i\bar{k} \cdot \bar{r}} \quad (1)$$

where  $E_h$  is the horizontal component,  $E_v$  is the vertical component,  $\hat{h}$  and  $\hat{v}$  are two orthogonal unit vectors satisfying the relation  $\hat{v} \times \hat{h} = \hat{k}$ . Consider an incident plane wave  $\bar{E}_i$  impinging on a particle. This particle will radiate and the scattered electric field  $\bar{E}_s$  can be related to the incident electric field  $\bar{E}_i$  by the scattering matrix [2]:

$$\begin{pmatrix} E_{hs} \\ E_{vs} \end{pmatrix} = \begin{pmatrix} HH & HV \\ VH & VV \end{pmatrix} \cdot \begin{pmatrix} E_{hi} \\ E_{vi} \end{pmatrix} \quad (2)$$

The elements of the scattering matrix are complex and the relation  $VH = HV$  holds [1] in the backscattering direction and for reciprocal media.

Instead of relating the scattered electric field to the incident electric field, the modified Stokes vector, defined by [1], can also be used to relate the scattered Stokes vector to the incident Stokes vector:

$$I_H = \frac{|E_h|^2}{\eta} \quad I_V = \frac{|E_v|^2}{\eta} \quad U = \frac{2}{\eta} \text{Re}(E_h E_v^*) \quad V = \frac{2}{\eta} \text{Im}(E_h E_v^*) \quad (3)$$



This definition is chosen since the first two modified Stokes parameters represent the intensity of the wave in the horizontal and vertical polarizations:

$$I = \begin{pmatrix} I_H \\ I_V \\ U \\ V \end{pmatrix} \quad (4)$$

In terms of the elements of the scattering matrix (2), the Mueller matrix  $\bar{M}$  relates the scattered to the incident Stokes vectors according to

$$I_s = \bar{M} \cdot I_i \quad (5)$$

is found to be

$$\begin{pmatrix} |HH|^2 & |HV|^2 & \text{Re}(HH \cdot HV^*) & -\text{Im}(HH \cdot HV^*) \\ |VH|^2 & |VV|^2 & \text{Re}(VH \cdot VV^*) & -\text{Im}(VH \cdot VV^*) \\ 2\text{Re}(HH \cdot VH^*) & 2\text{Re}(HV \cdot VV^*) & \text{Re}(HH \cdot VV^* + HV \cdot VH^*) & -\text{Im}(HH \cdot VV^* - HV \cdot VH^*) \\ 2\text{Im}(HH \cdot VH^*) & 2\text{Im}(HV \cdot VV^*) & \text{Im}(HH \cdot VV^* + HV \cdot VH^*) & \text{Re}(HH \cdot VV^* - HV \cdot VH^*) \end{pmatrix} \quad (6)$$

where all the Mueller matrix elements are real numbers. From the four elements of the scattering matrix (2), the covariance matrix may also be defined. In general the covariance is a complex matrix of sixteen elements. In the special case of the backscattering direction and for a reciprocal medium, the covariance matrix is transformed to a matrix of nine elements as follows

$$\bar{C} = \begin{pmatrix} HH \\ HV \\ VV \end{pmatrix} \begin{pmatrix} HH^* & HV^* & VV^* \end{pmatrix} = \begin{pmatrix} |HH|^2 & HH \cdot HV^* & HH \cdot VV^* \\ HV \cdot HH^* & |HV|^2 & HV \cdot VV^* \\ VV \cdot HH^* & VV \cdot HV^* & |VV|^2 \end{pmatrix} \quad (7)$$

By comparing the scattering (2), the Mueller (6), and the covariance matrices (7), it is easily seen that all the polarimetric information may be expressed in any of these matrices. The covariance and Mueller matrices can be transformed to each other since they contain the same information. However, from these two matrices, the scattering matrix cannot be fully retrieved because the absolute phase factor is not taken into account in either the covariance matrix or in the Mueller matrix.

In our study of microwave remote sensing, the random medium model is used to simulate the permittivity of the earth terrain. This implies that the simple case of a single particle can no longer be considered but the ensemble average of the electric field needs to be calculated. The polarimetric bistatic scattering coefficient  $\gamma_{\mu\nu\kappa}(\bar{k}_i, \bar{k}_s)$  is defined by [3]

$$\gamma_{\mu\nu\kappa}(\bar{k}_i, \bar{k}_s) = \lim_{\substack{A \rightarrow \infty \\ r \rightarrow \infty}} \frac{4\pi r^2}{A \cos \theta_{0i}} \frac{\langle E_{\mu s} E_{\nu i}^* \rangle}{E_{\tau i} E_{\kappa i}^*} = \lim_{\substack{A \rightarrow \infty \\ r \rightarrow \infty}} \frac{4\pi r^2}{A \cos \theta_{0i}} \langle \mu \tau \cdot \nu \kappa^* \rangle \quad (8)$$

where  $A$  is the area illuminated by the radar,  $r$  is the distance between the radar and the observed terrain, and  $\theta_0$  is the polar incident angle. Furthermore,  $\bar{k}_i$  and  $\bar{k}_s$  are the incident and scattered wave vectors, respectively. The subscripts  $s$  and  $i$  stand for scattered and incident waves, respectively. Finally,  $\mu\tau$  and  $\nu\kappa$  are the four components of the scattering matrix where  $\mu$ ,  $\tau$ ,  $\nu$ , and  $\kappa$  represent either the horizontal  $h$  or vertical  $v$  polarizations.

The polarimetric backscattering coefficient  $\sigma_{\mu\tau\nu\kappa}$  is defined [3] from the bistatic coefficient when  $\bar{k}_s = -\bar{k}_i$ ,

$$\sigma_{\mu\tau\nu\kappa} = \gamma_{\mu\tau\nu\kappa}(\bar{k}_i, -\bar{k}_i) \cos \theta_0 = \lim_{A \rightarrow \infty} \frac{4\pi r^2}{A} \frac{\langle E_{\mu s} E_{\nu i}^* \rangle}{E_{\tau i} E_{\kappa i}^*} = \lim_{A \rightarrow \infty} \frac{4\pi r^2}{A} \langle \mu\tau \cdot \nu\kappa^* \rangle \quad (9)$$

The polarimetric backscattering coefficients  $\sigma_{\mu\tau\nu\kappa}$  are complex except the three "traditional" real-valued backscattering coefficients

$$\begin{aligned} \sigma_{hhhh} &= \sigma_{hh} \\ \sigma_{hhvv} &= \sigma_{hv} \\ \sigma_{vvvv} &= \sigma_{vv} \end{aligned} \quad (10)$$

Similarly, the covariance matrix (7) constituted by the different polarimetric backscattering coefficients can be derived

$$\bar{C} = \lim_{A \rightarrow \infty} \frac{4\pi r^2}{A} \begin{pmatrix} HH \\ HV \\ VV \end{pmatrix} \cdot (HH^* \quad HV^* \quad VV^*) = \begin{pmatrix} \sigma_{hh} & \sigma_{hhvv} & \sigma_{hhvv} \\ \sigma_{hhvv}^* & \sigma_{hv} & \sigma_{hv} \\ \sigma_{hhvv} & \sigma_{hv}^* & \sigma_{vv} \end{pmatrix} \quad (11)$$

Therefore, the complete polarimetric information can be obtained by computing only six backscattering coefficients in which three are real ( $\sigma_{hh}$ ,  $\sigma_{hv}$ , and  $\sigma_{vv}$ ) and three are complex ( $\sigma_{hhvv}$ ,  $\sigma_{hhvv}^*$ ,  $\sigma_{hv}$ ).

## Formulation

Consider an electromagnetic plane wave impinging upon a two-layer random medium configuration as shown in Fig. 1. The top layer represents free space with a permittivity  $\epsilon_0$  while the bottom layer has a deterministic permittivity  $\epsilon_2$ . In between, a layer with thickness  $d$  and extending infinitely in the lateral direction is characterized by a random permittivity  $\epsilon_1(\bar{r})$

$$\epsilon_1(\bar{r}) = \epsilon_{1m} + \epsilon_{1f}(\bar{r}) \quad (12)$$

This random variable has a mean value  $\epsilon_{1m}$  and a small fluctuating term  $\epsilon_{1f}(\bar{r})$  whose average is zero. The wave equations for both regions may be written as

$$\nabla \times \nabla \times \bar{E}_0(\bar{r}) - k_0^2 \bar{E}_0(r) = 0 \quad (13)$$

$$\nabla \times \nabla \times \bar{E}_1(\bar{r}) - k_{1m}^2 \bar{E}_1(\bar{r}) = Q(\bar{r}) \bar{E}_1(\bar{r}) \quad (14)$$

where  $\bar{E}_0(\bar{r})$  and  $\bar{E}_1(\bar{r})$  denote the electric fields fluctuation in region 0 and region 1, respectively.

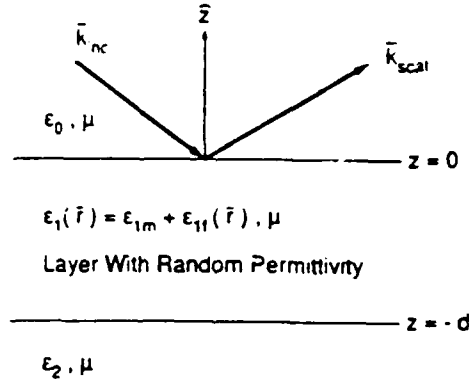


Figure 1: Isotropic two-layer configuration.

Furthermore, the following variables have been defined

$$k_0^2 = \omega^2 \mu \epsilon_0 \quad k_{1m}^2 = \omega^2 \mu \epsilon_{1m} \quad Q(\bar{r}) = \omega^2 \mu \epsilon_{1f}(\bar{r}) \quad (15)$$

With the effective source term  $Q(\bar{r}) \bar{E}_1(\bar{r})$ , (13) and (14) can be expressed in integral form as follows

$$\bar{E}_0(\bar{r}) = \bar{E}_0^{(0)}(\bar{r}) + \int d^3 \bar{r}_1 \bar{G}_{01}(\bar{r}, \bar{r}_1) Q(\bar{r}_1) \cdot \bar{E}_1(\bar{r}_1) \quad (16)$$

$$\bar{E}_1(\bar{r}) = \bar{E}_1^{(0)}(\bar{r}) - \int d^3 \bar{r}_1 \bar{G}_{11}(\bar{r}, \bar{r}_1) Q(\bar{r}_1) \cdot \bar{E}_1(\bar{r}_1) \quad (17)$$

where  $\bar{E}_0^{(0)}(\bar{r})$  and  $\bar{E}_1^{(0)}(\bar{r})$  are the specular or coherent electric fields in the absence of random permittivity in region 1. Furthermore  $\bar{G}_{01}(\bar{r}, \bar{r}_1)$  and  $\bar{G}_{11}(\bar{r}, \bar{r}_1)$  are the dyadic Green's functions for observers in regions 0 and 1, respectively, with the source in region 1. Solutions to these two coupled equations can be obtained by iteration. Substituting (17) into (16), the total electric field in region 0 is found to be in form of the Neumann series

$$\bar{E}_0(\bar{r}) = \bar{E}_0^{(0)}(\bar{r}) + \sum_{n=1}^{\infty} \bar{E}_0^{(n)}(\bar{r}) \quad (18)$$

where the  $n^{\text{th}}$  order field is given by

$$\bar{E}_0^{(n)}(\bar{r}) = \int d^3\bar{r}_1 \cdots d^3\bar{r}_n \bar{G}_{01}(\bar{r}, \bar{r}_1) Q(\bar{r}_1) \cdot \bar{G}_{11}(\bar{r}_1, \bar{r}_2) Q(\bar{r}_2) \cdots \bar{G}_{11}(\bar{r}_{n-1}, \bar{r}_n) Q(\bar{r}_n) \cdot \bar{E}_1^{(0)}(\bar{r}_n) \quad (19)$$

The so-called "Born first-order approximation" is obtained by letting  $n = 1$  in the previous equation. Hence

$$\bar{E}_0^{(1)}(\bar{r}) = \int d^3\bar{r}_1 \bar{G}_{01}(\bar{r}, \bar{r}_1) Q(\bar{r}_1) \cdot \bar{E}_1^{(0)}(\bar{r}_1) \quad (20)$$

and the "Born second-order approximation" is derived by letting  $n = 2$

$$\bar{E}_0^{(2)}(\bar{r}) = \int d^3\bar{r}_1 d^3\bar{r}_2 \bar{G}_{01}(\bar{r}, \bar{r}_1) Q(\bar{r}_1) \cdot \bar{G}_{11}(\bar{r}_1, \bar{r}_2) Q(\bar{r}_2) \cdot \bar{E}_1^{(0)}(\bar{r}_2) \quad (21)$$

## Born First-Order Approximation

### a) Isotropic random medium model

Consider an electromagnetic plane wave impinging upon a two-layer random medium configuration as shown in Fig. 1. For an incident electric field in region 0 of the following form

$$\bar{E}_0(\bar{r}) = [E_{0h}\hat{h}(-k_{0zi})e^{-ik_{0zi}z} + E_{0v}\hat{v}(-k_{0zi})e^{-ik_{0zi}z}] e^{i\bar{k}_0 \cdot \bar{r}} \quad (22)$$

where  $\hat{h}(-k_{0zi})$  and  $\hat{v}(-k_{0zi})$  are respectively the horizontal and vertical unit vectors in region 0 associated with down-going waves, the coherent electric field in the random medium is obtained [4]

$$\bar{E}_1^{(0)}(\bar{r}) = \left\{ E_{0h} [A_h \hat{h}(k_{1zi})e^{ik_{1zi}z} + B_h \hat{h}(-k_{1zi})e^{-ik_{1zi}z}] + E_{0v} [A_v \hat{v}(k_{1zi})e^{ik_{1zi}z} + B_v \hat{v}(-k_{1zi})e^{-ik_{1zi}z}] \right\} e^{i\bar{k}_0 \cdot \bar{r}} \quad (23)$$

in which the following coefficients are defined [3]

$$\begin{aligned} A_h &= \frac{X_{01i}}{D_{2i}} R_{12i} e^{i2k_{1zi}d} & A_v &= \frac{k_0}{k_1} \frac{Y_{01i}}{F_{2i}} S_{12i} e^{i2k_{1zi}d} \\ B_h &= \frac{X_{01i}}{D_{2i}} & B_v &= \frac{k_0}{k_1} \frac{Y_{01i}}{F_{2i}} \\ D_{2i} &= 1 + R_{01i} R_{12i} e^{i2k_{1zi}d} & F_{2i} &= 1 + S_{01i} S_{12i} e^{i2k_{1zi}d} \\ R_{abi} &= \frac{k_{azi} - k_{bzi}}{k_{azi} + k_{bzi}} & S_{abi} &= \frac{\epsilon_b k_{azi} - \epsilon_a k_{bzi}}{\epsilon_b k_{azi} + \epsilon_a k_{bzi}} \\ X_{abi} &= 1 + R_{abi} & Y_{abi} &= 1 + S_{abi} \end{aligned} \quad (24)$$

As can be seen in (23), the  $A$  coefficients are associated with the up-going waves while the  $B$  coefficients describe the down-going waves. Under the far-field approximation, the Green's function in (20) takes the following form in the backscattering direction [5]

$$\bar{G}_{01}(\bar{r}, \bar{r}_1) = \hat{h}(-k_{0zi}) \bar{G}_{01h}(\bar{r}, \bar{r}_1) + \hat{v}(-k_{0zi}) \bar{G}_{01v}(\bar{r}, \bar{r}_1) \quad (25)$$

$$\bar{G}_{01h}(\bar{r}, \bar{r}_1) = \frac{e^{ik_0 r}}{4\pi r} [A_h \hat{h}(k_{1zi})e^{ik_{1zi}z_1} + B_h \hat{h}(-k_{1zi})e^{-ik_{1zi}z_1}] e^{i\bar{k}_0 \cdot \bar{r}} \quad (26)$$

$$\bar{G}_{01v}(\bar{r}, \bar{r}_1) = \frac{e^{ik_0 r}}{4\pi r} [A_v \hat{v}(k_{1zi})e^{ik_{1zi}z_1} + B_v \hat{v}(-k_{1zi})e^{-ik_{1zi}z_1}] e^{i\bar{k}_0 \cdot \bar{r}} \quad (27)$$

For each polarization, both  $\bar{G}_{01}(\bar{r}, \bar{r}_1)$  and  $\bar{E}_1^{(0)}(\bar{r})$  are constituted by a down- and an up-going waves. Therefore,  $\bar{E}_0^{(1)}(\bar{r})$  is formed by the sum of four different terms as shown in Fig. 2. All the multiple reflections occurring at the boundaries are also incorporated in the model and the backscattered wave is due to the single scattering process under the Born first-order approximation.

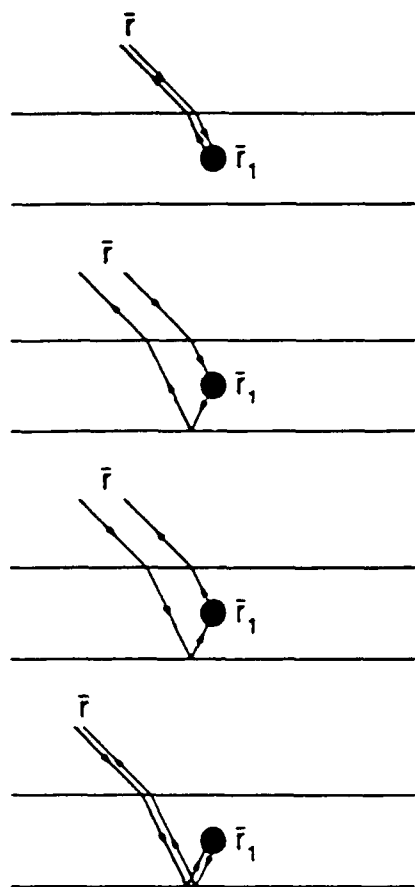


Figure 2: Physical interpretation for Born first-order approximation.

To compute the polarimetric backscattering coefficients (9), only the components of the backscattered electric field are needed. Furthermore, the polarization of the incident wave  $\vec{E}_1^{(0)}(\vec{r})$  is only along one direction, either horizontal or vertical. With the Fourier transform of the autocorrelation of the permittivity fluctuation for a statistical homogeneous random medium

$$\langle Q(\vec{r}_1)Q(\vec{r}_2)^* \rangle = \delta\omega^4 \mu^2 |\epsilon_{1m}|^2 \int_{-\infty}^{\infty} d^3\vec{\beta} \Phi(\vec{\beta}) e^{-i\vec{\beta} \cdot (\vec{r}_1 - \vec{r}_2)} \quad (28)$$

the ensemble average for the first-order backscattered intensity takes the following form

$$\langle E_{0\mu}^{(1)}(\bar{r}) E_{0\nu}^{(1)}(\bar{r})^* \rangle = \delta\omega^4 \mu^2 |\epsilon_{1m}|^2 \int d^3\bar{r}_1 d^3\bar{r}_2 \int d^3\bar{\beta} \Phi(\bar{\beta}) e^{-i\bar{\beta} \cdot (\bar{r}_1 - \bar{r}_2)} \left[ \bar{G}_{01\mu}(\bar{r}, \bar{r}_1) \cdot \bar{E}_{1\tau}^{(0)}(\bar{r}_1) \right] \left[ \bar{G}_{01\nu}(\bar{r}, \bar{r}_2) \cdot \bar{E}_{1\kappa}^{(0)}(\bar{r}_2) \right]^* \quad (29)$$

where  $\tau$  and  $\kappa$  represent either the horizontal or vertical component of the transmitted wave and  $\mu$  and  $\nu$  represent either the horizontal or vertical component of the received wave. From (23), the following term has been defined

$$\bar{E}_{1\alpha}^{(0)}(\bar{r}) = \sum_{p=-1}^1 E_{0\alpha i} X_{\alpha p} \hat{a}(pk_{1zi}) e^{ipk_{1zi}z} e^{i\bar{k}_p \cdot \bar{r}} \quad (30)$$

where  $\alpha$  stands either for  $h$  or  $v$ , and  $p$  describes either up or down-going waves. In a similar manner,

$$\bar{G}_{01\alpha}(\bar{r}, \bar{r}_1) = \frac{e^{ik_0 r}}{4\pi r} \sum_{p=-1}^1 X_{\alpha p} \hat{a}(pk_{1zi}) e^{ipk_{1zi}z_1} e^{i\bar{k}_p \cdot \bar{r}_1} \quad (31)$$

where the following definitions have been used

$$X_{h1i} = A_{h1}, \quad X_{h-1i} = B_{h1}, \quad X_{v1i} = A_{v1}, \quad X_{v-1i} = B_{v1} \quad (32)$$

Substituting (30) and (31) into (29), a sum of 16 terms is obtained

$$\langle E_{0\mu}^{(1)}(\bar{r}) E_{0\nu}^{(1)}(\bar{r})^* \rangle = \frac{\delta\omega^4 \mu^2 |\epsilon_{1m}|^2}{16\pi^2 r^2} E_{0\tau i} E_{0\kappa i}^* \sum_{p,q,r,s=-1}^1 [X_{\mu p} X_{\tau q} \hat{\mu}(pk_{1zi}) \cdot \hat{\tau}(qk_{1zi})] [X_{\nu r} X_{\kappa s} \hat{\nu}(rk_{1zi}) \cdot \hat{\kappa}(sk_{1zi})]^* \int d^3\bar{r}_1 d^3\bar{r}_2 \int d^3\bar{\beta} \Phi(\bar{\beta}) e^{-i\bar{\beta} \cdot (\bar{r}_1 - \bar{r}_2)} [e^{i(p\bar{k}_{1zi} + q\bar{k}_{1zi})z_1} e^{2i\bar{k}_p \cdot \bar{r}_1}] [e^{i(r\bar{k}_{1zi} + s\bar{k}_{1zi})z_2} e^{2i\bar{k}_r \cdot \bar{r}_2}]^* \quad (33)$$

As can be seen, all the polarization information is contained outside the integral. Also, the intensity is expressed as a sum of sixteen terms since the electric field is composed of four elements. With the two following scalar quantities

$$\Psi_{\mu\tau\nu\kappa}^{\text{pqrs}} = X_{\mu p} X_{\tau q} X_{\nu r}^* X_{\kappa s}^* \quad (34)$$

$$\Omega_{\mu\tau\nu\kappa}^{\text{pqrs}} = [\hat{\mu}(pk_{1zi}) \cdot \hat{\tau}(qk_{1zi})] [\hat{\nu}(rk_{1zi}) \cdot \hat{\kappa}(sk_{1zi})]^* \quad (35)$$

(33) can be written as

$$\langle E_{0\mu}^{(1)}(\bar{r}) E_{0\nu}^{(1)}(\bar{r})^* \rangle = \frac{\delta\omega^4 \mu^2 |\epsilon_{1m}|^2}{16\pi^2 r^2} E_{0\tau i} E_{0\kappa i}^* \sum_{p,q,r,s=-1}^1 \Psi_{\mu\tau\nu\kappa}^{\text{pqrs}} \Omega_{\mu\tau\nu\kappa}^{\text{pqrs}} \int d^3\bar{r}_1 d^3\bar{r}_2 \int d^3\bar{\beta} \Phi(\bar{\beta}) e^{-i\bar{\beta} \cdot (\bar{r}_1 - \bar{r}_2)} [e^{i(p\bar{k}_{1zi} + q\bar{k}_{1zi})z_1} e^{2i\bar{k}_p \cdot \bar{r}_1}] [e^{i(r\bar{k}_{1zi} + s\bar{k}_{1zi})z_2} e^{2i\bar{k}_r \cdot \bar{r}_2}]^* \quad (36)$$

The integrals in (36) are solved by decomposing the variables of integration into their lateral and vertical components. By using the property of the Delta function and introducing the illuminated area  $A$ , the integration over the lateral variables  $\bar{\rho}_1$ ,  $\bar{\rho}_2$ , and  $\bar{\beta}_\rho$  yields

$$\langle E_{0\mu}^{(1)}(\bar{r}) E_{0\nu}^{(1)}(\bar{r})^* \rangle = \frac{\delta\omega^4 \mu^2 |\epsilon_{1m}|^2 A}{4r^2} E_{0r_1} E_{0\alpha_1} \sum_{p,q,r,s=-1}^1 \Psi_{\mu\nu\rho\alpha}^{pqrs} \Omega_{\mu\nu\rho\alpha}^{pqrs} \int d\beta_z dz_1 dz_2 \\ \Phi(\bar{\beta}_\rho = 2\bar{k}_\rho, \beta_z) e^{iz_1[pk_{1z_1} + qk_{1z_1} - \beta_z]} e^{-iz_2[(rk_{1z_1} + sk_{1z_1})^* - \beta_z]} \quad (37)$$

In order to solve the last set of equations, let us define first the two complex quantities

$$a = pk_{1z_1} + qk_{1z_1} \quad b = [rk_{1z_1} + sk_{1z_1}]^* \quad (38)$$

Hence, the integral part of (37) may be written

$$\int dz_1 dz_2 e^{iaz_1} e^{-ibz_2} \int d\beta_z \Phi(\bar{\beta}_\rho = 2\bar{k}_\rho, \beta_z) e^{-i\beta_z(z_1 - z_2)} \quad (39)$$

Due to Cauchy's theorem, the integral over  $\beta_z$  yields the following expression by distinguishing two cases depending upon the sign of  $z_1 \sim z_2$

$$\int d\beta_z \Phi(2\bar{k}_\rho, \beta_z) e^{-i\beta_z(z_1 - z_2)} = \begin{cases} 2\pi i \text{Res}\Phi(2\bar{k}_\rho, \beta_z^+) e^{-i\beta_z^+(z_1 - z_2)} & \text{if } z_1 < z_2 \\ -2\pi i \text{Res}\Phi(2\bar{k}_\rho, \beta_z^-) e^{-i\beta_z^-(z_1 - z_2)} & \text{if } z_1 > z_2 \end{cases} \quad (40)$$

where it is assumed that the spectrum density  $\Phi(\bar{\beta}_\rho, \beta_z)$  has only one pair of complex conjugate poles at  $\beta_z = \beta_z^\pm$ , and  $\Phi(\bar{\beta}_\rho, \beta_z)$  vanishes everywhere on the infinite circle. For the random medium of infinite lateral dimension and vertical extension from  $z = -d$  to  $z = 0$ , (39) becomes

$$2\pi i \text{Res}\Phi(\bar{\beta}_\rho = 2\bar{k}_\rho, \beta_z^+) \int_{-d}^0 dz_1 \int_{z_1}^0 dz_2 e^{iaz_1} e^{-ibz_2} e^{-i\beta_z^+(z_1 - z_2)} \\ - 2\pi i \text{Res}\Phi(\bar{\beta}_\rho = 2\bar{k}_\rho, \beta_z^-) \int_{-d}^0 dz_1 \int_{-d}^{z_1} dz_2 e^{iaz_1} e^{-ibz_2} e^{-i\beta_z^-(z_1 - z_2)} \quad (41)$$

For  $\text{Res}(\bar{\beta}_\rho = 2\bar{k}_\rho, \beta_z^-) = -\text{Res}(\bar{\beta}_\rho = 2\bar{k}_\rho, \beta_z^+)$ , these integrals may be easily solved to get

$$2\pi i \text{Res}\Phi(\bar{\beta}_\rho = 2\bar{k}_\rho, \beta_z^+) \left[ \frac{1 - e^{-i(a - \beta_z^+)d}}{(a - \beta_z^+)(b - \beta_z^+)} - \frac{1 - e^{-i(a - b)d}}{(a - b)(b - \beta_z^+)} \right. \\ \left. + \frac{1 - e^{-i(a - b)d}}{(a - b)(b - \beta_z^-)} - \frac{e^{i(b - \beta_z^-)d}}{(a - \beta_z^-)(b - \beta_z^-)} + \frac{e^{-i(a - b)d}}{(a - \beta_z^-)(b - \beta_z^-)} \right] \quad (42)$$



To simplify the expression, let us define the following term

$$I^{pqrs} = \left[ \frac{1 - e^{-i(a-\beta_i^+)d}}{(a - \beta_i^+)(b - \beta_i^+)} - \frac{1 - e^{-i(a-b)d}}{(a-b)(b - \beta_i^+)} + \frac{1 - e^{-i(a-b)d}}{(a-b)(b - \beta_i^-)} \right. \\ \left. - \frac{e^{i(b-\beta_i^-)d}}{(a - \beta_i^-)(b - \beta_i^-)} + \frac{e^{-i(a-b)d}}{(a - \beta_i^-)(b - \beta_i^-)} \right] \quad (43)$$

From (38),  $a$  is different from  $b$  for most cases because of the complex conjugation. However, for the special case when  $a = b = 0$ , (43) may be written as

$$I^{pqrs} = \left[ \frac{1 - e^{i\beta_i^+ d}}{\beta_i^{+2}} + \frac{id}{\beta_i^+} - \frac{id}{\beta_i^-} + \frac{1 - e^{-i\beta_i^- d}}{\beta_i^{-2}} \right] \quad (44)$$

Substituting (43) and (44) into (37) and using (9), the polarimetric backscattering coefficients are found to be

$$\sigma_{\mu\nu\rho\kappa} = 2\pi^2 \delta\omega^4 \mu^2 |\epsilon_{1m}|^2 i \text{Res} \Phi(\bar{\beta}_\rho = 2\bar{k}_\rho, \beta_i^+) \sum_{p,q,r,s=-1}^1 \Psi_{\mu\nu\rho\kappa}^{pqrs} \Omega_{\mu\nu\rho\kappa}^{pqrs} I^{pqrs} \quad (45)$$

Only three polarimetric backscattering coefficients are different from zero. This comes from the factor  $\Omega_{\mu\nu\rho\kappa}^{pqrs}$  in (35). They are zero due to the definition of the unit vectors [3]. Hence, the final results are

$$\begin{aligned} \sigma_{hh} &= 2\pi^2 \delta\omega^4 \mu^2 |\epsilon_{1m}|^2 i \text{Res} \Phi(\bar{\beta}_\rho = 2\bar{k}_\rho, \beta_i^+) \sum_{p,q,r,s=-1}^1 \Psi_{hhhh}^{pqrs} I^{pqrs} \\ \sigma_{vv} &= 2\pi^2 \delta\omega^4 \mu^2 |\epsilon_{1m}|^2 i \text{Res} \Phi(\bar{\beta}_\rho = 2\bar{k}_\rho, \beta_i^+) \sum_{p,q,r,s=-1}^1 \Psi_{vvvv}^{pqrs} \Omega_{vvvv}^{pqrs} I^{pqrs} \\ \sigma_{hhvv} &= 2\pi^2 \delta\omega^4 \mu^2 |\epsilon_{1m}|^2 i \text{Res} \Phi(\bar{\beta}_\rho = 2\bar{k}_\rho, \beta_i^+) \sum_{p,q,r,s=-1}^1 \Psi_{hhvv}^{pqrs} \Omega_{hhvv}^{pqrs} I^{pqrs} \quad (46) \end{aligned}$$

$$\sigma_{hv} = \sigma_{vh} = \sigma_{hhvv} = \sigma_{vvvv} = 0 \quad (47)$$

For an autocorrelation function for the random permittivity (12) of the form

$$\langle \epsilon_{1f}(\bar{r}_1) \epsilon_{1f}(\bar{r}_2)^* \rangle = \ell |\epsilon_{1m}|^2 e^{-\frac{|\bar{r}_1 - \bar{r}_2|^2}{l_p^2}} e^{-\frac{|\bar{r}_1 - \bar{r}_2|^2}{l_v^2}} \quad (48)$$

where  $\ell$  is the variance,  $l_p$  and  $l_v$  are the lateral and vertical correlation lengths, respectively, the spectrum density (28) is given by

$$\Phi(\beta_x, \beta_y, \beta_z) = \frac{l_p^2 l_v}{\pi^3 (1 + \beta_x^2 l_p^2) (1 + \beta_y^2 l_p^2) (1 + \beta_z^2 l_v^2)} \quad (49)$$

The spectral density goes to zero as  $\bar{\beta}$  tends to infinity satisfying the requirement for the complex integration (40). The poles  $\beta_z$  of the spectrum density are obtained

$$\beta_z^\pm = \pm \frac{i}{l_z} \quad (50)$$

Furthermore, the associated residues are found to be

$$\text{Res}\Phi(\beta_z, \beta_y, \beta_z^\pm) = \pm \frac{l_\rho^2}{2\pi^3 i (1 + \beta_z^2 l_\rho^2) (1 + \beta_y^2 l_\rho^2)} \quad (51)$$

## b) Anisotropic random medium model

In order to describe earth terrains exhibiting an anisotropic behavior, the random permittivity is chosen to be uniaxial in a tilted coordinate system [6]. Earth terrains such as sea ice and corn fields display such a property. From (12), the random permittivity is written in a tensor form

$$\bar{\epsilon}_1(\bar{r}) = \bar{\epsilon}_{1m} + \bar{\epsilon}_{1f}(\bar{r}) \quad (52)$$

where  $\bar{\epsilon}_{1f}(\bar{r})$  is a function of position characterizing the randomly fluctuating component of the permittivity. For the random medium, it is assumed that both  $\bar{\epsilon}_{1m}$  and  $\bar{\epsilon}_{1f}(\bar{r})$  are uniaxial in a coordinate system  $xy'z'$  tilted respectively at an angle  $\psi$ ,  $\psi_f$  around the  $\bar{r}$  axis as represented in Fig. 3. In this tilted coordinate system, the permittivity tensor  $\bar{\epsilon}_{1m}$  takes the following form

$$\bar{\epsilon}_{1m} = \begin{pmatrix} \epsilon_1 & 0 & 0 \\ 0 & \epsilon_1 & 0 \\ 0 & 0 & \epsilon_{1z} \end{pmatrix} \quad (53)$$

In the coordinate system  $xyz$ , the permittivity tensor can be expressed as

$$\bar{\epsilon}_{1m} = \begin{pmatrix} \epsilon_{11} & 0 & 0 \\ 0 & \epsilon_{22} & \epsilon_{23} \\ 0 & \epsilon_{32} & \epsilon_{33} \end{pmatrix} \quad (54)$$

where

$$\begin{aligned} \epsilon_{11} &= \epsilon_1 \\ \epsilon_{22} &= \epsilon_1 \cos^2 \psi + \epsilon_{1z} \sin^2 \psi \\ \epsilon_{23} &= \epsilon_{32} = (\epsilon_{1z} - \epsilon_1) \sin \psi \cos \psi \\ \epsilon_{33} &= \epsilon_1 \sin^2 \psi + \epsilon_{1z} \cos^2 \psi \end{aligned} \quad (55)$$

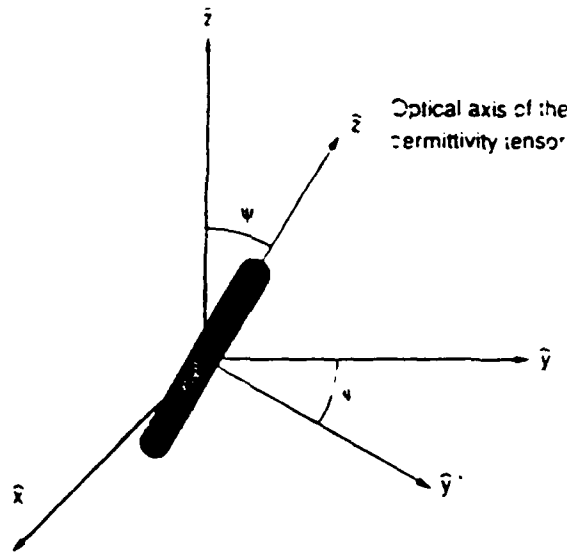


Figure 3: Geometrical configuration of the permittivity tensor in an anisotropic random medium.

Similar equations may be written for  $\bar{\epsilon}_{1j}(\bar{r})$  with the tilt angle  $\psi_j$ . From (20), the "Born first-order approximation" yields for the anisotropic case

$$\bar{E}_0^{(1)}(\bar{r}) = \int d^3\bar{r}_1 \bar{G}_{01}(\bar{r}, \bar{r}_1) \cdot \bar{Q}(\bar{r}_1) \cdot \bar{E}_1^{(0)}(\bar{r}_1) \quad (56)$$

where  $\bar{Q}(\bar{r}) = \omega^2 \mu \bar{\epsilon}_{1j}(\bar{r})$ . Using Euler notation and decomposing the electric field in horizontal and vertical components, the ensemble average for the first-order backscattered intensity may be written as

$$\begin{aligned} \langle E_{0\mu}^{(1)}(\bar{r}) E_{0\nu}^{(1)}(\bar{r})^* \rangle &= \sum_{j,k,l,m=1}^3 \int d^3\bar{r}_1 d^3\bar{r}_2 [G_{01\mu j}(\bar{r}, \bar{r}_1) E_{1\tau k}^{(0)}(\bar{r}_1)] \\ &\quad [G_{01\nu l}(\bar{r}, \bar{r}_2) E_{1\kappa m}^{(0)}(\bar{r}_2)]^* \langle Q_{jk}(\bar{r}_1) Q_{lm}^*(\bar{r}_2) \rangle \end{aligned} \quad (57)$$

where the average of the components of the electric field has been computed by defining  $\mu$  and  $\nu$  as the received polarizations and  $\tau$  and  $\kappa$  as the transmitted polarizations.

As shown in Fig. 4, a horizontally or a vertically polarized incident electric field will generate both an ordinary and an extraordinary waves, due to the anisotropic permittivity in region 1, defined by their respective wave numbers [6]

$$k_{1z1}^o = \sqrt{\omega^2 \mu \epsilon_1 - k_\rho^2}$$

$$\begin{aligned}
 k_{1zi}^{eo} &= -\frac{\epsilon_{23}}{\epsilon_{33}}k_{yi} + \frac{1}{\epsilon_{33}}\sqrt{\omega^2\mu\epsilon_1\epsilon_{1z}\epsilon_{33} - \epsilon_1\epsilon_{33}k_{xi}^2 - \epsilon_1\epsilon_{1z}k_{yi}^2} \\
 k_{1zi}^{ed} &= -\frac{\epsilon_{23}}{\epsilon_{33}}k_{yi} - \frac{1}{\epsilon_{33}}\sqrt{\omega^2\mu\epsilon_1\epsilon_{1z}\epsilon_{33} - \epsilon_1\epsilon_{33}k_{xi}^2 - \epsilon_1\epsilon_{1z}k_{yi}^2}
 \end{aligned}
 \quad (58)$$

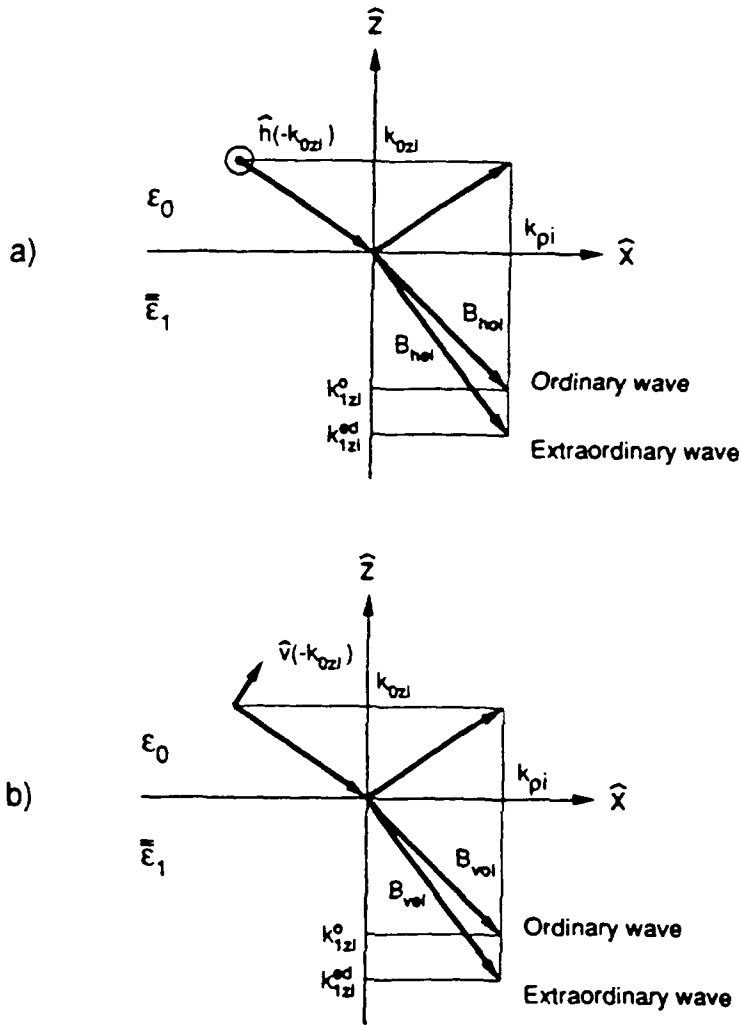


**Figure 4:** Ordinary and extraordinary electromagnetic waves excited by the anisotropic random medium. (a) Horizontally polarized incident electric field. (b) Vertically polarized electric field.

The components of the unperturbed electric field  $\bar{E}_1^{(0)}(\bar{r})$  and the Green's function  $\bar{G}_{01}(\bar{r}, \bar{r}_1)$  may be written as [7]

$$\bar{E}_{1\alpha}^{(0)}(\bar{r}) = \sum_{p=o, -o, eu, ed} E_{0\alpha i} X_{\alpha p} \hat{p}(k_{1zi}^p) e^{ik_{1zi}^p z} e^{i\bar{k}_{\alpha} \cdot \bar{r}} \quad (59)$$

$$\bar{G}_{01\alpha}(\bar{r}, \bar{r}_1) = \frac{e^{ik_0 r}}{4\pi r} \sum_{p=o, -o, eu, ed} X_{\alpha p} \hat{p}(k_{1zi}^p) e^{ik_{1zi}^p z_1} e^{i\bar{k}_{\alpha} \cdot \bar{r}_1} \quad (60)$$

where  $\alpha$  stands for either  $h$  or  $v$ , and  $p$  describes either an ordinary up-going wave ( $o$ ), an ordinary down-going wave ( $-o$ ), an extraordinary up-going ( $eu$ ), or an extraordinary down-going wave ( $ed$ ). Both the incident electric field and the Green's function are formed each by four terms meaning that backscattered electric field computed with Born first-order approximation will be constituted by sixteen terms. Furthermore, the coefficients  $X_{\alpha p}$ , the unit vectors  $\hat{p}(k_{1zi}^p)$ , and the wave numbers  $k_{1zi}^p$  take on the following expressions depending on the value of  $p$

$$\begin{array}{lll} p = o \Rightarrow k_{1zi}^p = k_{1zi}^o & \hat{p}(k_{1zi}^p) = \hat{o}(k_{1zi}^o) & X_{\alpha p} = A_{\alpha oi} \\ p = -o \Rightarrow k_{1zi}^p = -k_{1zi}^o & \hat{p}(k_{1zi}^p) = \hat{o}(-k_{1zi}^o) & X_{\alpha p} = B_{\alpha oi} \\ p = eu \Rightarrow k_{1zi}^p = k_{1zi}^{eu} & \hat{p}(k_{1zi}^p) = \hat{e}(k_{1zi}^{eu}) & X_{\alpha p} = A_{\alpha ei} \\ p = ed \Rightarrow k_{1zi}^p = k_{1zi}^{ed} & \hat{p}(k_{1zi}^p) = \hat{e}(k_{1zi}^{ed}) & X_{\alpha p} = B_{\alpha ei} \end{array} \quad (61)$$

Hence, substituting (59) and (60) into (57) yields

$$\begin{aligned} \langle E_{0\mu}^{(1)}(\bar{r}) E_{0\nu}^{(1)}(\bar{r})^* \rangle &= \frac{\omega^4 \mu^2 |\epsilon_1|^2}{16\pi^2 r^2} E_{0\tau i} E_{0\alpha i}^* \sum_{j,k,l,m=1}^3 \sum_{p,q,r,s=o}^{ed} \\ & [X_{\mu p} X_{\tau q} \hat{p}(k_{1zi}^p)_j \cdot \hat{q}(k_{1zi}^q)_k] [X_{\nu r} X_{\alpha s} \hat{r}(k_{1zi}^r)_l \cdot \hat{s}(k_{1zi}^s)_m]^* \int d^3 \bar{r}_1 d^3 \bar{r}_2 \\ & \int d^3 \bar{r} \Phi_{jklm}(\bar{r}) e^{-i\bar{s} \cdot (\bar{r}_1 - \bar{r}_2)} \left[ e^{i(k_{1zi}^p + k_{1zi}^q)z_1} e^{2i\bar{k}_{\mu} \cdot \bar{r}_1} \right] \left[ e^{i(k_{1zi}^r + k_{1zi}^s)z_2} e^{2i\bar{k}_{\nu} \cdot \bar{r}_2} \right]^* \end{aligned} \quad (62)$$

As can be seen, all the polarization information is contained outside the integral. The parameters  $p, q, r$ , and  $s$  can take the values  $o, -o, eu$ , or  $ed$  as described in (61). The intensity is hence given by a sum of 256 terms. For each of these terms, 81 products (sum over  $jklm$ ) have to be computed due to the anisotropic behavior of the random medium. In order to simplify this result, let us define the two following scalar quantities

$$\Psi_{\mu\tau\nu\alpha}^{pqrs} = X_{\mu p} X_{\tau q} X_{\nu r}^* X_{\alpha s}^* \quad (63)$$

$$\Omega_{jklm}^{pqrs} = [\hat{p}(k_{1zi}^p)_j \cdot \hat{q}(k_{1zi}^q)_k] [\hat{r}(k_{1zi}^r)_l \cdot \hat{s}(k_{1zi}^s)_m]^* \quad (64)$$

Hence, (62) may be written

$$\begin{aligned} \langle E_{0\mu}^{(1)}(\bar{r}) E_{0\nu}^{(1)}(\bar{r})^* \rangle &= \frac{\omega^4 \mu^2 |\epsilon_1|^2}{16\pi^2 r^2} E_{0r_1} E_{0r_2}^* \sum_{j,k,l,m=1}^3 \sum_{p,q,r,s=0}^{cd} \Psi_{\mu\tau\nu\kappa}^{pqrs} \Omega_{jklm}^{pqrs} \\ &\int d^3\bar{r}_1 d^3\bar{r}_2 \int d^3\bar{\beta} \Phi_{jklm}(\bar{\beta}) e^{-i\bar{\beta} \cdot (\bar{r}_1 - \bar{r}_2)} \left[ e^{i(k_{1z}^p + k_{1z}^q)z_1} e^{2i\bar{k}_\rho \cdot \bar{\rho}_1} \right] \left[ e^{i(k_{1z}^r + k_{1z}^s)z_2} e^{2i\bar{k}_\rho \cdot \bar{\rho}_2} \right]^* \end{aligned} \quad (65)$$

By following a similar procedure as in the isotropic case described in (37) through (45), the parameters  $a$  and  $b$  are first defined as

$$a = k_{1z,1}^p + k_{1z,1}^q \quad b = [k_{1z,1}^r + k_{1z,1}^s]^* \quad (66)$$

By assuming a spectrum density  $\Phi(\bar{\beta}_\rho, \beta_z)$  with  $n$  pairs of complex conjugate poles at  $\beta_z = \beta_{zn}^\pm$  and defining the following factors

$$I_{n+}^{pqrs} = \frac{1 - e^{-i(a - \beta_{zn}^+)d}}{(a - \beta_{zn}^+)(b - \beta_{zn}^+)} - \frac{1 - e^{-i(a-b)d}}{(a-b)(b - \beta_{zn}^+)} \quad (67)$$

$$I_{n-}^{pqrs} = \frac{1 - e^{-i(a-b)d}}{(a-b)(b - \beta_{zn}^-)} - \frac{e^{i(b - \beta_{zn}^-)d}}{(a - \beta_{zn}^-)(b - \beta_{zn}^-)} + \frac{e^{-i(a-b)d}}{(a - \beta_{zn}^-)(b - \beta_{zn}^-)} \quad (68)$$

the six polarimetric backscattering coefficients (11) are finally found to be [8]

$$\begin{aligned} \sigma_{\mu\tau\nu\kappa} &= 2\pi^2 \omega^4 \mu^2 |\epsilon_1|^2 \sum_{p,q,r,s=0}^{cd} \Psi_{\mu\tau\nu\kappa}^{pqrs} \sum_{j,k,l,m=1}^3 \Omega_{jklm}^{pqrs} \\ &i \sum_n \left\{ \text{Res} \Phi_{jklm}(\bar{\beta}_\rho = 2\bar{k}_\rho, \beta_{zn}^+) I_{n+}^{pqrs} - \text{Res} \Phi_{jklm}(\bar{\beta}_\rho = 2\bar{k}_\rho, \beta_{zn}^-) I_{n-}^{pqrs} \right\} \end{aligned} \quad (69)$$

Compared to the results of the isotropic case shown in (46) and (47), there is no zero elements. This is due to the anisotropic behavior and the excitation of both ordinary and extraordinary waves.

## Born Second-Order Approximation

For this case, only the isotropic random permittivity will be considered. From (21), the second-order scattered electric field is given by

$$\bar{E}_0^{(2)}(\bar{r}) = \int d^3\bar{r}_1 d^3\bar{r}_2 \bar{G}_{01}(\bar{r}, \bar{r}_1) Q(\bar{r}_1) \cdot \bar{G}_{11}(\bar{r}_1, \bar{r}_2) Q(\bar{r}_2) \cdot \bar{E}_1^{(0)}(\bar{r}_2) \quad (70)$$

where  $\bar{E}_1^{(0)}(\bar{r})$  and  $\bar{G}_{01}(\bar{r}, \bar{r}_1)$  are given by (30) and (31), respectively. The Green's function  $\bar{G}_{11}(\bar{r}_1, \bar{r}_2)$  relates the field observed in region 1 at a position  $\bar{r}_1$  due to a source in region 1 located at  $\bar{r}_2$ . It takes the following form from [9]

$$\bar{G}_{11}(\bar{r}_1, \bar{r}_2) = \frac{i}{8\pi^2} \int d^2\bar{k}_\rho \left\{ \begin{array}{l} \bar{g}_{11}^>(\bar{k}_\rho, z_1, z_2) \\ \bar{g}_{11}^<(\bar{k}_\rho, z_1, z_2) \end{array} \right\} e^{i\bar{k}_\rho \cdot (\bar{r}_1 - \bar{r}_2)} \quad \left\{ \begin{array}{l} z_1 > z_2 \\ z_1 < z_2 \end{array} \right. \quad (71)$$

where

$$\bar{g}_{11}^>(\bar{k}_\rho, z_1, z_2) = \frac{1}{k_{1z}} \sum_{q,r=-1}^1 e^{iqk_{1z}z_1} e^{ir k_{1z}z_2} \sum_{\alpha=h,v} C_{\alpha q r}^>(\bar{k}_\rho) \hat{\alpha}(qk_{1z}) \hat{\alpha}(-rk_{1z}) \quad (72)$$

$$\bar{g}_{11}^<(\bar{k}_\rho, z_1, z_2) = \frac{1}{k_{1z}} \sum_{q,r=-1}^1 e^{iqk_{1z}z_1} e^{ir k_{1z}z_2} \sum_{\alpha=h,v} C_{\alpha q r}^<(\bar{k}_\rho) \hat{\alpha}(qk_{1z}) \hat{\alpha}(-rk_{1z}) \quad (73)$$

Here  $\alpha$  denotes the polarization direction along  $h$  or  $v$ , and the coefficients  $C$  take the following values [3]

$$\begin{aligned} C_{h11}^>(\bar{k}_\rho) &= C_{h11}^<(\bar{k}_\rho) = R_{12}e^{i2k_{1z}d}/D_2 & C_{h1-1}^>(\bar{k}_\rho) &= C_{h-11}^<(\bar{k}_\rho) = 1/D_2 \\ C_{h-11}^>(\bar{k}_\rho) &= C_{h1-1}^<(\bar{k}_\rho) = R_{10}R_{12}e^{i2k_{1z}d}/D_2 & C_{h-1-1}^>(\bar{k}_\rho) &= C_{h-1-1}^<(\bar{k}_\rho) = R_{10}/D_2 \\ C_{v11}^>(\bar{k}_\rho) &= C_{v11}^<(\bar{k}_\rho) = S_{12}e^{i2k_{1z}d}/F_2 & C_{v1-1}^>(\bar{k}_\rho) &= C_{v-11}^<(\bar{k}_\rho) = 1/F_2 \\ C_{v-11}^>(\bar{k}_\rho) &= C_{v1-1}^<(\bar{k}_\rho) = S_{10}S_{12}e^{i2k_{1z}d}/F_2 & C_{v-1-1}^>(\bar{k}_\rho) &= C_{v-1-1}^<(\bar{k}_\rho) = S_{10}/F_2 \end{aligned} \quad (74)$$

The physical meaning of the Born second-order approximation (70) are interpreted based on the fact that  $\bar{G}_{01}(\bar{r}, \bar{r}_1)$ ,  $\bar{G}_{11}(\bar{r}_1, \bar{r}_2)$ , and  $\bar{E}_1^{(0)}(\bar{r})$  are composed of a down- and an up-going wave for each polarization. Therefore,  $\bar{E}_0^{(1)}(\bar{r})$  is formed by the sum of sixteen different terms as shown in Fig. 5. All the multiple reflections occurring at the boundaries are accounted for and the backscattered wave is due to the double scattering process under the Born second-order approximation.

With (30), (31), and (70), the ensemble average for the second-order intensity is given by

$$\begin{aligned} \langle E_{0\mu}^{(2)}(\bar{r}) E_{0\nu}^{(2)*}(\bar{r}) \rangle &= \int d^3\bar{r}_1 d^3\bar{r}_2 d^3\bar{r}_3 d^3\bar{r}_4 \langle Q(\bar{r}_1) Q(\bar{r}_2) Q(\bar{r}_3)^* Q(\bar{r}_4)^* \rangle \\ &\quad \left[ \bar{G}_{01\mu}(\bar{r}, \bar{r}_1) \cdot \bar{G}_{11}(\bar{r}_1, \bar{r}_2) \cdot \bar{E}_{1\tau}^{(0)}(\bar{r}_2) \right] \left[ \bar{G}_{01\nu}(\bar{r}, \bar{r}_3) \cdot \bar{G}_{11}(\bar{r}_3, \bar{r}_4) \cdot \bar{E}_{1\alpha}^{(0)}(\bar{r}_4) \right]^* \quad (75) \end{aligned}$$





Similarly to (28), by using the spectrum density of the autocorrelation function and integrating over the lateral variables, the ensemble average takes the following form

$$\begin{aligned}
 \langle E_{0\mu}^{(2)}(\bar{r}) E_{0\nu}^{(2)}(\bar{r})^* \rangle &= \frac{\delta^2 \omega^8 \mu^4 |\epsilon_{1m}|^4 A}{16\tau^2} E_{0\tau i} E_{0\kappa i}^* \int d^2 \bar{k}_\rho \int dz_1 dz_2 dz_3 dz_4 \\
 &\int d\beta_{z1} d\beta_{z2} \Phi(\bar{k}_\rho + \bar{k}_\rho, \beta_{z1}) \Phi(\bar{k}_\rho - \bar{k}_\rho, \beta_{z2}) \frac{1}{|k_{1z}|^2} \sum_{\substack{p, q, r, s \\ p', q', r', s' = -1}}^1 \Psi_{\mu\nu\kappa}^{p, p', s'} \\
 &e^{i(p k_{1z1} + q k_{1z2})z_1} e^{i(s k_{1z1} + r k_{1z2})z_2} e^{-i(p' k_{1z1}^* + q' k_{1z2}^*)z_3} e^{-i(s' k_{1z1}^* + r' k_{1z2}^*)z_4} \sum_{\alpha, \gamma = h, v} \Upsilon_{\alpha\gamma \ell_1 \ell_2}^{q', q', r', r'}(\bar{k}_\rho) \\
 &\left\{ \Omega_{\mu\nu\kappa, \alpha\gamma}^{p, p', q', q', s', s'}(\bar{k}_\rho) e^{-i\beta_{z1}(z_1 - z_3)} e^{-i\beta_{z2}(z_2 - z_4)} \right. \\
 &\left. + \Omega_{\mu\nu\kappa, \alpha\gamma}^{p, p', q', q', s', s'}(-\bar{k}_\rho) e^{-i\beta_{z1}(z_1 - z_4)} e^{-i\beta_{z2}(z_2 - z_3)} \right\} \quad (77)
 \end{aligned}$$

where the following terms have been defined

$$\Psi_{\mu\nu\kappa}^{p, p', s'} = X_{\mu p i} X_{\tau s i} X_{\nu p' i}^* X_{\kappa s' i}^* \quad (78)$$

$$\Upsilon_{\alpha\gamma \ell_1 \ell_2}^{q', q', r', r'}(\bar{k}_\rho) = C_{\alpha\gamma\tau}^{\ell_1}(\bar{k}_\rho) C_{\gamma q' r'}^{\ell_2^*}(\bar{k}_\rho) \quad (79)$$

$$\begin{aligned}
 \Omega_{\mu\nu\kappa, \alpha\gamma}^{p, p', q', q', s', s'}(\bar{k}_\rho) &= [\hat{\mu}(p k_{1z1}) \cdot \hat{\alpha}(q k_{1z2}) \hat{\alpha}(-r k_{1z2}) \cdot \hat{\tau}(s k_{1z1})] \\
 &[\hat{\nu}(p' k_{1z1}) \cdot \hat{\gamma}(q' k_{1z2}) \hat{\gamma}(-r' k_{1z2}) \cdot \hat{\kappa}(s' k_{1z1})]^* \quad (80)
 \end{aligned}$$

$$\begin{aligned}
 \Omega_{\mu\nu\kappa, \alpha\gamma}^{p, p', q', q', s', s'}(-\bar{k}_\rho) &= [\hat{\mu}(p k_{1z1}) \cdot \hat{\alpha}(q k_{1z2}) \hat{\alpha}(-r k_{1z2}) \cdot \hat{\tau}(s k_{1z1})] \\
 &[\hat{\nu}(p' k_{1z1}) \cdot \hat{\gamma}(-q' k_{1z2}) \hat{\gamma}(r' k_{1z2}) \cdot \hat{\kappa}(s' k_{1z1})]^* \quad (81)
 \end{aligned}$$

In the polar coordinate system, (77) becomes

$$\begin{aligned}
 \langle E_{0\mu}^{(2)}(\bar{r}) E_{0\nu}^{(2)}(\bar{r})^* \rangle &= \frac{\delta^2 \omega^8 \mu^4 |\epsilon_{1m}|^4 \pi A}{64\tau^2} E_{0\tau i} E_{0\kappa i}^* \int d\bar{k}_\rho \int dz_1 dz_2 dz_3 dz_4 \\
 &\frac{k_\rho}{|k_{1z}|^2} \sum_{\substack{p, q, r, s \\ p', q', r', s' = -1}}^1 \Psi_{\mu\nu\kappa}^{p, p', s'} e^{i(p k_{1z1} + q k_{1z2})z_1} e^{i(s k_{1z1} + r k_{1z2})z_2} e^{-i(p' k_{1z1}^* + q' k_{1z2}^*)z_3} e^{-i(s' k_{1z1}^* + r' k_{1z2}^*)z_4} \\
 &\sum_{\alpha, \gamma = h, v} \Upsilon_{\alpha\gamma \ell_1 \ell_2}^{q', q', r', r'}(k_\rho) \left\{ I_{\mu\nu\kappa, \alpha\gamma}^{p, p', q', q', s', s'}(k_\rho) \int d\beta_{z1} d\beta_{z2} \Phi(k_\rho + k_\rho, \beta_{z1}) \Phi(k_\rho - k_\rho, \beta_{z2}) \right. \\
 &e^{-i\beta_{z1}(z_1 - z_3)} e^{-i\beta_{z2}(z_2 - z_4)} + I_{\mu\nu\kappa, \alpha\gamma}^{p, p', q', q', s', s'}(-k_\rho) \int d\beta_{z1} d\beta_{z2} \Phi(k_\rho + k_\rho, \beta_{z1}) \\
 &\left. \Phi(k_\rho - k_\rho, \beta_{z2}) e^{-i\beta_{z1}(z_1 - z_4)} e^{-i\beta_{z2}(z_2 - z_3)} \right\} \quad (82)
 \end{aligned}$$

where the integration over  $\phi$  has yielded [3]

$$\frac{4}{\pi} \int_0^{2\pi} d\phi \Omega_{\mu\nu\kappa, \alpha\gamma}^{p, p', q', q', s', s'}(\bar{k}_\rho) = I_{\mu\nu\kappa, \alpha\gamma}^{p, p', q', q', s', s'}(k_\rho) \quad (83)$$

$$\frac{1}{\pi} \int_0^{2\pi} d\phi \Omega_{\mu\nu\kappa, \sigma\gamma}^{pqrs, p'q'r's'}(-\vec{k}_\rho) = \int_{\mu\nu\kappa, \sigma\gamma}^{pqrs, p'-q-r's'}(k_\rho) \quad (84)$$

Using the Cauchy's theorem, the integration over  $\beta_{z1}$  and  $\beta_{z2}$  may be carried out. The final result for the polarimetric backscattering coefficients are obtained [3]

$$\begin{aligned} \sigma_{\mu\nu\kappa} &= \frac{\pi^4 \delta^2 \omega^8 \mu^4 |\epsilon_{1m}|^4}{4} \int dk_\rho \frac{k_\rho}{|k_{1z}|^2} i \text{Res} \Phi(k_\rho + k_\rho, \beta_z^-) \\ &\quad i \text{Res} \Phi(k_\rho - k_\rho, \beta_z^+) \sum_{\substack{p', q', r', s' = -1 \\ p, q, r, s = -1}}^1 \Psi_{\mu\nu\kappa}^{pqrs, p'q'r's'} \sum_{\sigma, \gamma = h, v} \sum_{\xi_1, \xi_2 = -1}^1 \Upsilon_{\sigma\gamma, \xi_1 \xi_2}^{q'r', q's'}(k_\rho) \\ &\quad \left\{ \int_{\mu\nu\kappa, \sigma\gamma}^{pqrs, p'q'r's'}(k_\rho) M_{\xi_1 \xi_2}^{pqrs, p'q'r's'}(k_\rho) + \int_{\mu\nu\kappa, \sigma\gamma}^{pqrs, p'-q-r's'}(k_\rho) N_{\xi_1 \xi_2}^{pqrs, p'q'r's'}(k_\rho) \right\} \quad (85) \end{aligned}$$

The factors  $M$  and  $N$  are defined in [3]. It is noted that the integral over  $v_\rho$  cannot be solved analytically but only numerically. From the integration over the azimuthal variable  $\phi$  in (83) and (84), it is found that  $\sigma_{hh\tau\tau} = \sigma_{hh\tau\tau} = 0$ . However, the depolarization term  $\sigma_{hv}$  is different from zero, unlike the result obtained with the isotropic Born first-order approximation.

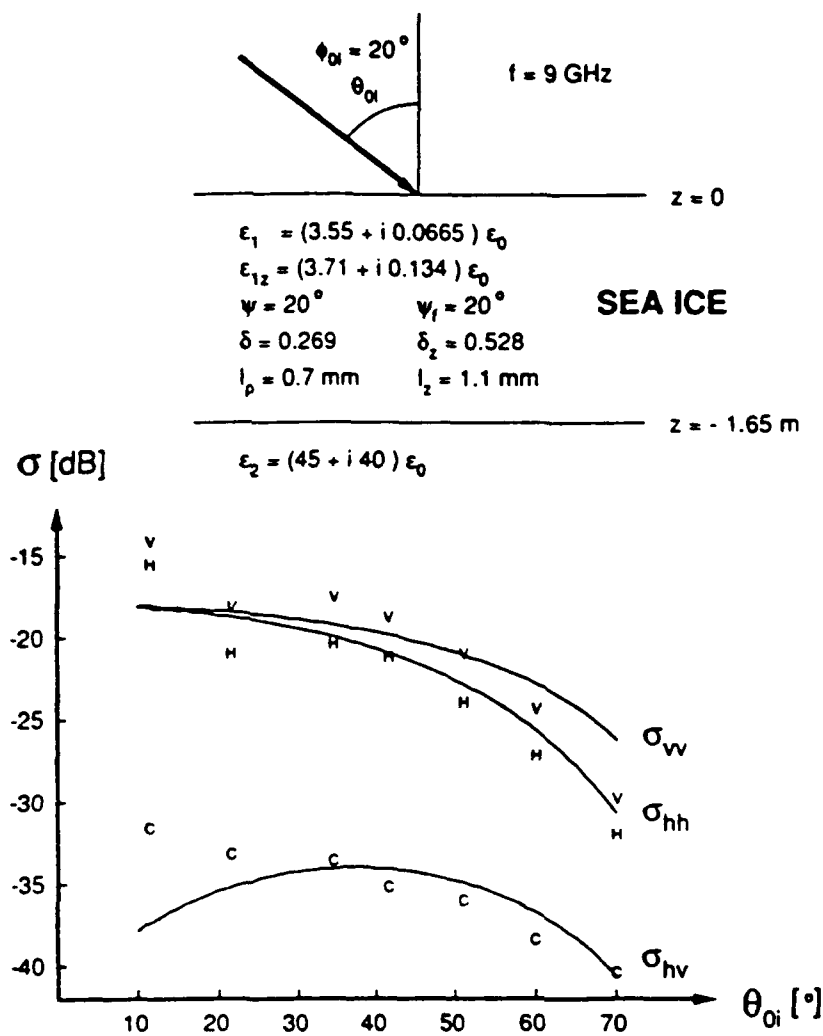
## Results

### a) Born first-order approximation

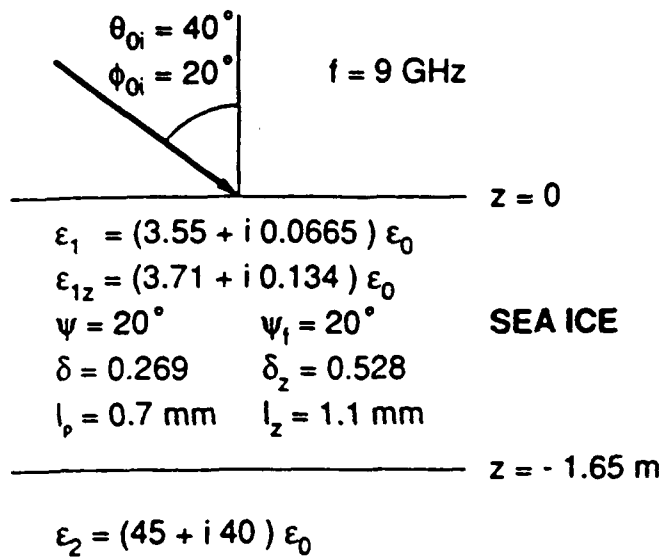
With the Born first-order approximation, the polarimetric backscattering coefficients have been obtained for the two-layer isotropic and anisotropic random medium configurations. For the anisotropic random medium, the depolarization term  $\sigma_{\Delta\Delta} \neq 0$  exists even with Born first-order approximation. In general, all the backscattering coefficients  $\sigma_{HH}$ ,  $\sigma_{HV}$ ,  $\sigma_{VH}$ ,  $\sigma_{VV}$ ,  $\sigma_{HH\Delta\Delta}$ ,  $\sigma_{HV\Delta\Delta}$ ,  $\sigma_{\Delta\Delta\Delta\Delta}$ , are different from zero for the anisotropic case. However, when  $\psi = \psi_f = 0^\circ$  but  $\epsilon_1 \neq \epsilon_{1z}$ , no depolarization term is obtained for this uniaxial untilted case and  $\sigma_{\Delta\Delta} = \sigma_{HH\Delta\Delta} = \sigma_{HV\Delta\Delta} = 0$ . Also, for  $\psi = 0$  but  $\psi_f \neq 0$ , the non-zero depolarization terms  $\sigma_{HH\Delta\Delta}$  and  $\sigma_{HV\Delta\Delta}$  are obtained. Finally, when  $\psi \neq 0$ , all the backscattering coefficients are different from zero. In a similar manner, when  $\phi = 90^\circ$ , implying that the plane of incidence contains the scatterers, there is no depolarization factor, and only three backscattering coefficients are different from zero ( $\sigma_{\Delta\Delta} = \sigma_{HH\Delta\Delta} = \sigma_{HV\Delta\Delta} = 0$ ).

Fig. 6 illustrates dependence of the backscattering coefficients on the angle of incidence for  $\sigma_{HH}$ ,  $\sigma_{VV}$  and  $\sigma_{HV}$  for a two-layer configuration, and these results are matched with experimental data for sea ice taken in 1984 in Point Barrow in Alaska by [10]. The input parameters  $\epsilon_1$ ,  $\epsilon_{1z}$ ,  $\delta$ , and  $\delta_z$  are obtained using the strong fluctuation theory developed in [11]. The tilt angle is chosen to be  $\psi = \psi_f = 20^\circ$ , and the azimuthal angle is assumed to be  $\phi = 20^\circ$ . The good correspondence is noted between the experimental results and the theoretical predictions. Fixing the incident angle at  $\theta_{0i} = 40^\circ$  in Fig. 6, the covariance matrix for the backscattering coefficient (14) is shown in Fig. 7. As can be seen, this matrix does not contain any zero elements.

For an earth terrain medium such as trees or grass, leaves grow randomly in the azimuthal direction. This can be modeled by assuming that one patch illuminated by the radar is oriented in a certain direction whereas the next patch is oriented in a different direction and so on. To obtain the backscattering coefficients, the average over many patches should be taken. This model is used in the theory by assuming a fixed direction of the scatterers but modifying the position of the radar over the azimuthal direction. This is shown in Fig. 8 for grass and in Fig. 9 for trees where both these vegetation fields are simulated by averaging the backscattering coefficients over  $\phi$ . The step of averaging is  $\Delta\phi = 1^\circ$ . Though the tilt angle  $\psi$  is different from zero, there is a depolarization factor ( $\sigma_{\Delta\Delta} \neq 0$ ), but  $\sigma_{HH\Delta\Delta} = \sigma_{HV\Delta\Delta} = 0$ . This is due to symmetrical reasons because the contribution of these two backscattering coefficients at  $\phi$  is cancelled by the one at  $180^\circ - \phi$ . Also in Fig. 8 and in Fig. 9, experimental polarimetric radar data obtained by MIT Lincoln Laboratory are displayed [14]. The frequency of operation was 35 GHz, and the angle of incidence was  $82^\circ$  (depression angle of  $8^\circ$ ). The radar illuminated on a vegetation field consisting of either grass or trees at a range of  $\sim 2$  km. A good correspondence between the theoretical predictions and the experimental results is obtained.



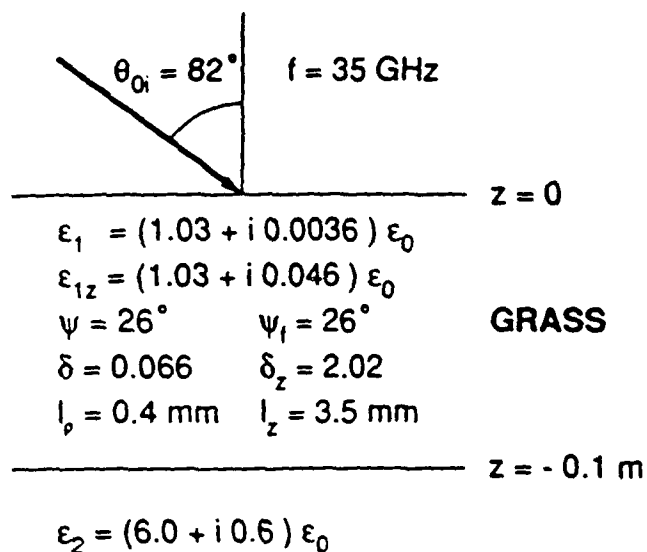
**Figure 6:** Backscattering coefficient at 9 GHz as a function of incident polar angle matched for sea ice.



Covariance matrix:

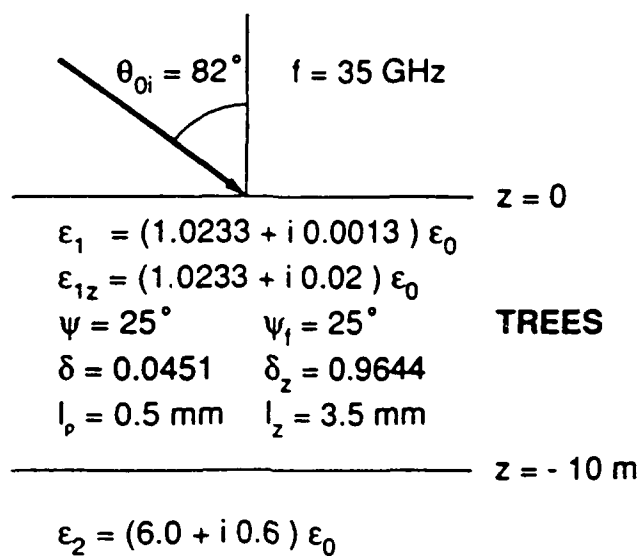
$$10^{-3} \cdot \begin{pmatrix} 8.43 & 0.23 + i 1.18 & 9.40 - i 0.76 \\ 0.23 - i 1.18 & 0.39 & 0.02 - i 1.34 \\ 9.40 + i 0.76 & 0.02 + i 0.134 & 10.6 \end{pmatrix}$$

**Figure 7:** Covariance matrix for the backscattering coefficients at  $\theta_{0i} = 40^\circ$  for sea ice.



	$\sigma_{hh} \text{ (dB)}$	$\frac{\sigma_{hv}}{\sigma_{hh}}$	$\frac{\sigma_w}{\sigma_{hh}}$	$\frac{\text{Re}(\sigma_{hhw})}{\sqrt{\sigma_{hh} \sigma_w}}$	$\frac{\text{Im}(\sigma_{hhw})}{\sqrt{\sigma_{hh} \sigma_w}}$
Experiment	-14.5	0.19	1.4	0.54	0.03
Born	-14.4	0.17	1.3	0.59	0.04

**Figure 8:** Covariance matrix elements for grass region using the average over the azimuthal angle  $\phi$  with  $\Delta\phi = 1^\circ$ . Experimental measurements and theoretical calculations are shown.



	$\sigma_{hh} \text{ (dB)}$	$\frac{\sigma_{hv}}{\sigma_{hh}}$	$\frac{\sigma_{vw}}{\sigma_{hh}}$	$\frac{\text{Re}(\sigma_{hhvw})}{\sqrt{\sigma_{hh} \sigma_{vw}}}$	$\frac{\text{Im}(\sigma_{hhvw})}{\sqrt{\sigma_{hh} \sigma_{vw}}}$
Experiment	-10.8	0.12	1.2	0.64	0.01
Born	-10.6	0.12	1.2	0.65	0.05

**Figure 9:** Covariance matrix elements for tree region using the average over the azimuthal angle  $\phi$  with  $\Delta\phi = 1^\circ$ . Experimental measurements and theoretical calculations are shown.

### b) Born second-order approximation

Unlike the isotropic Born first-order approximation, a depolarization factor  $\sigma_{hv} \neq 0$  is obtained with the isotropic Born second-order approximation [9]. Furthermore, it was shown that  $\sigma_{hhh} = \sigma_{hvv} = 0$ . Hence, the covariance matrix can be written from (11)

$$\bar{C} = \begin{pmatrix} \sigma_{hh} & 0 & \sigma_{hvv} \\ 0 & \sigma_{vv} & 0 \\ \sigma_{hvv}^* & 0 & \sigma_{vv} \end{pmatrix} \quad (86)$$

Although a mathematical proof has been used to show that five elements of the covariance matrix are zero, this fact may also be illustrated from a physical point of view. Let us concentrate on the term  $\sigma_{vvhr}$  which is proportional to  $\langle VV \cdot HV^* \rangle$  from (11). By assuming that a vertically polarized electric field is transmitted, symbolized by  $\vec{v}$  in Fig. 10, the product of the waves polarized in the horizontal and vertical directions at the receiver is taken. The wave hits a first scatterer at position  $\vec{r}_1$  and then hits a second scatterer at position  $\vec{r}_2$ . At that location, the electric field  $\vec{E}$  induces a dipole which can be decomposed into horizontal and vertical components. From that point, the wave is backscattered and the receiver collects either  $HV^*$  or  $VV$ . Due to symmetry reasons, the second scatterer may be located at position  $\vec{r}_2'$ . The corresponding electric field  $\vec{E}'$  is decomposed into a vertical component and a horizontal component which is in the opposite direction from the component created by  $\vec{r}_2$ . At the receiver, either  $HV^*$  or  $VV$  is collected. In order to obtain  $\sigma_{vvhr}$ , the product of these two quantities must be taken. However, the product created by the location at  $\vec{r}_2$  will have an opposite sign from the one created at the location  $\vec{r}_2'$ . By taking the average, these two contributions cancel and  $\sigma_{vvhr} = 0$  is obtained. Similarly for every point, there is a symmetric scatterer which will cancel its contribution.

The depolarization factor is proportional to  $\langle HV \cdot HV^* \rangle$ , i.e., a vertically polarized electric field is transmitted and the horizontal component of the scattered field is received. Unlike the term  $\langle VV \cdot HV^* \rangle$ , both quantities  $HV$  and  $HV^*$  due to the dipole at location  $\vec{r}_2$  are in the opposite direction from the ones created by the scatterer at  $\vec{r}_2'$ . This implies that the product of the two quantities, which have the same sign independent of the position of the second scatterer  $\vec{r}_2'$  or  $\vec{r}_2''$ , renders the average backscattering coefficient  $\sigma_{hv}$  different from zero as shown in Fig. 11.



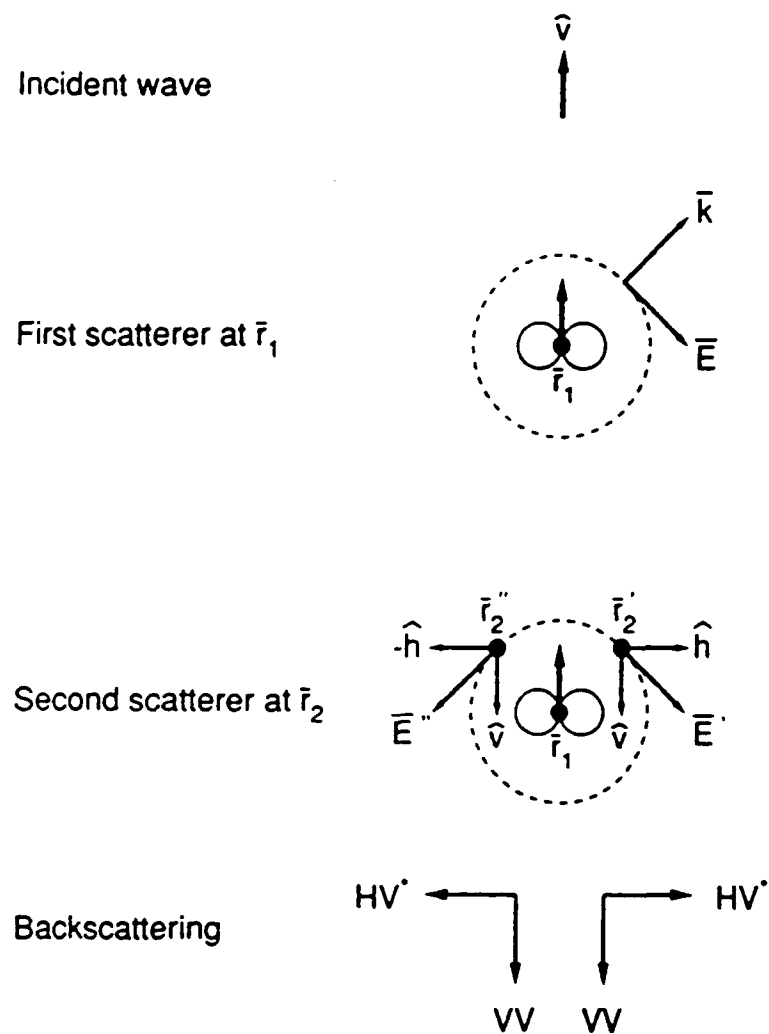
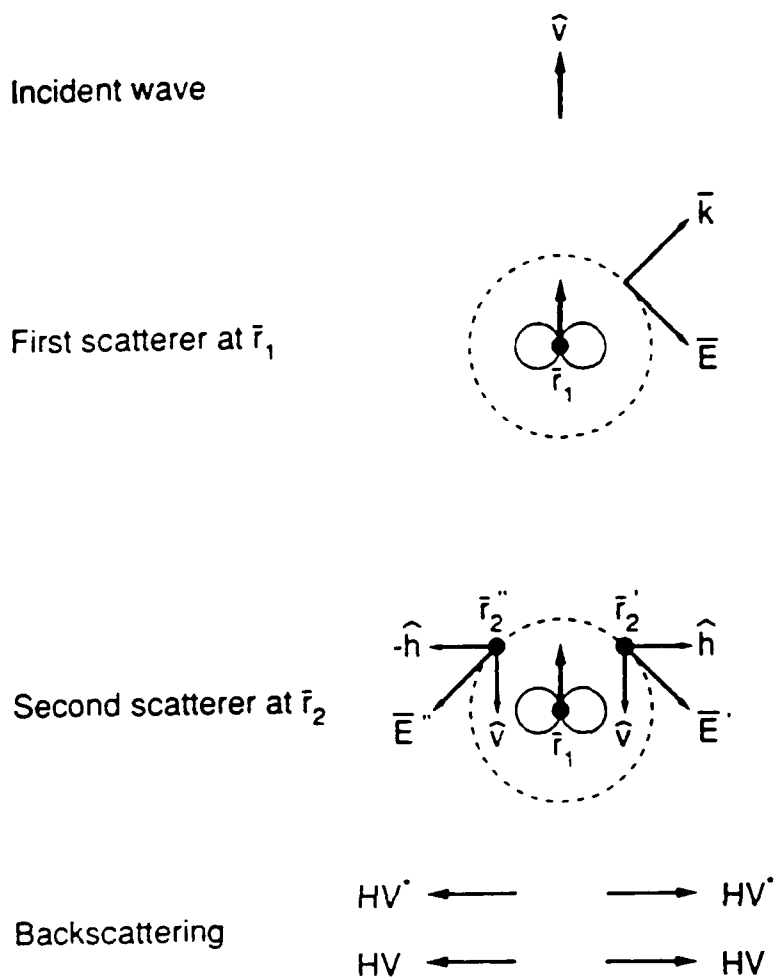


Figure 10: Interpretation of the term  $\langle VV \cdot HV^* \rangle$  with the Born second order approximation.



**Figure 11:** Interpretation of the term  $\langle HV \cdot HV^* \rangle$  with the Born second order approximation.

### c) Strong permittivity fluctuation theory

The variance of permittivity fluctuations is usually large in geophysical media consisting of mixtures of constituents with very different properties. With the diagrammatic approach [1], the propagation and scattering in random media can be studied. The diagrammatic approach leads to the Dyson's equation for the mean field. It should be noted that in solving Dyson's equation with the bilocal approximation, both the observation point and the source point within the random medium can coincide with each other in the domain of integration. To take care of the singular nature of the dyadic Green's functions, a strong permittivity fluctuation theory that applies to both small and large variances of the permittivity functions has been developed [11].

The mean field and the mean Green's function are calculated by replacing the medium with an equivalent medium having an effective permittivity which accounts for losses due to both absorption and scattering.

It should be emphasized that the effect of the random medium on electromagnetic waves is better described with the strong permittivity fluctuation theory than in the case of the traditional "weak permittivity fluctuations". For the case of a random medium described by a mixture of two components, only the fractional volume, the correlation lengths, the permittivity of the two components, and the frequency are necessary to describe the effect of the earth terrain. The other parameters, that is the variances and the mean permittivities, needed for the Born approximation are computed with the strong permittivity fluctuation theory.

In order to illustrate the results of the strong permittivity fluctuation theory, we compare  $\sigma_{AA}$  in Fig. 12 obtained with the weak permittivity fluctuation theory compared with the strong permittivity fluctuation theory. We use a correlation function exponentially decaying in all directions with  $l_p = l_s = 0.3$  mm. The physical parameters chosen in Fig. 12 characterized a layer of dry snow [13]. In Fig. 12, we plot  $\sigma_{AA}$  in the function of the frequency for  $\theta_0 = 60^\circ$ . As shown, the results obtained with the strong permittivity fluctuation theory are smaller than those obtained with the weak permittivity fluctuation theory. This difference gets larger with increasing frequencies. This is due to the fact that the losses due to scattering, which increase with increasing frequencies, are taken into account in the strong permittivity fluctuation theory.

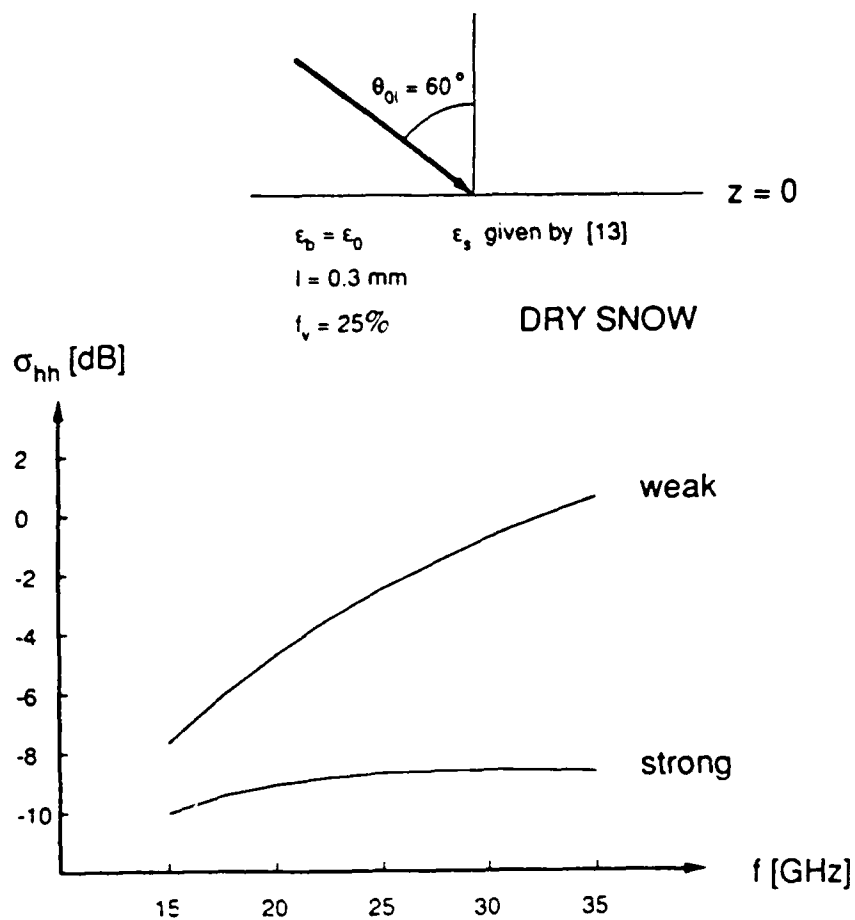


**Figure 12:** Backscattering coefficient  $\sigma_{hh}$  in function of the frequency computed with the weak and strong permittivity fluctuation theories.